



K A U N O
TECHNOLOGIJOS
UNIVERSITETAS

2007

ISSN 1822-5721

MEDICAL PHYSICS in the BALTIC STATES

PROCEEDINGS OF THE 5th INTERNATIONAL
CONFERENCE ON *MEDICAL PHYSICS*

Kaunas, Lithuania
5-6 October, 2007

ISSN 1822-5721

KAUNAS UNIVERSITY OF TECHNOLOGY

MEDICAL PHYSICS IN THE BALTIC STATES

Proceedings of the 5th International Conference on Medical Physics

**Kaunas, Lithuania
5 – 6 October, 2007**

Kaunas

Executive editor: **D.Adlienė**

CONFERENCE IS ORGANIZED BY:

Kaunas University of Technology
Malmö University Hospital, Lund University
Lithuanian Radiation Protection Centre
Kaunas Medical University Hospital

PROGRAM COMMITTEE

Diana ADLIENĖ - Kaunas University of Technology, *chairwoman*
Sören MATTSSON - Lund University, Malmö University Hospital, *chairman*
Ričardas ROTOMSKIS – Vilnius University
Albinas MASTAUSKAS – Lithuanian Radiation Protection Centre
Elona JUOZAITYTĖ – Medical University of Kaunas

ORGANIZING COMMITTEE

Lena ANCEVIČIENĖ – Kaunas University of Technology
Jurgita LAURIKAITIENĖ – Kaunas University of Technology
Gediminas ADLYS, Jr. – Kaunas University of Technology

CONFERENCE IS SUPPORTED BY:

Lithuanian State Science and Studies Foundation
Kaunas University of Technology
Malmö University Hospital
Lithuanian Radiation Protection Centre

Papers included in the Proceedings were referred by independent peer referees

CONFERENCE PROGRAM

Friday, October 5, 2007

- 10.00-11.00** Registration of participants at **Kaunas University of Technology, Studentų g.50–103a. , Kaunas**
- 11.00–11.10** Opening of the conference, *Diana Adlienė and Sören Mattsson* and Wellcome address to the participants of the conference, *Vytautas Janilionis, Dean of the Faculty of Fundamental Sciences*
- 11.10-11.40** *Kristina Stenström, Sören Mattsson*. Accelerator mass spectrometry (AMS) for pharmaceutical microdosing studies
- 11.40-12.10** *Saulius Bagdonas, Vitalijus Karabanovas, Jurga Valančiūnaitė, Ričardas Rotomskis*. Nanoparticle-sensitizer complexes: implication for photodynamic therapy
- 12.10-12.30** *Mindaugas Tamošiūnas, Martynas Plukys, Saulius Bagdonas, Gražina Gražalienė, Ričardas Rotomskis*. The application of Chlorin e₆ photobleaching in the dosimetry of PDT
- 12.30-12.45** *Jonas Venius, Ričardas Rotomskis*. Non invasive diagnostic method for the detection of non superficial lesions
- 12.45-13.00** *Vytautas Kulvietis, Eugenijus Zakarevičius, Ričardas Rotomskis, Juozas Lapienis, Gražina Gražalienė*. Comparison of PHOTOGEM[®] and AlPcS₄ accumulation in healthy rat brain

Time for the lunch 13:00 – 14:00

- 14.00-14.30** *Helen Gustavsson, Anna Karlsson, Sofie Månsson, Fredrik Nordström, Lena Wittgren and Sven ÅJ Bäck*. IMRT dose verification
- 14.30-15.00** *Sergey Popov, Sandija Plaude, Albert Miller, Yuri Dekhtyar*. New Portal Dosimetry Method for the Intensity Modulated Radiotherapy Fields
- 15.00-15.20** *Laimonas Šiupšinskas, Sigitas Tamulevičius, Rimantas Gudaitis, Alfonsas Vainoras*. Application of cold and heat contrast therapy device in the treatment of myofascial trigger points
- 15.20-15.40** *Albert Miller, Ieva Simutytė, Romualdas Griškevičius, Arvydas Burneikis*. Patient related quality controll of complex HDR brachytherapy treatments
- 15.40-16.00** *Marius Laurikaitis, Jurgita Laurikaitienė, Tatjana Zakrevskaja, Sven Bäck, Fredrik Nordström, Sören Mattsson, Gediminas A. Adlys, Saulius Raila, Diana Adlienė*. Implementation of the independent dose calculation algorithm for the checking of the Co-60 unit treatment plans

Coffee break 16.00-16.2

- 16.20-16.40** *Pontus Timberg, Mark Ruschin, Tony Svahn, Ingvar Andersson, Bengt Hemdal, Sören Mattsson, Magnus Båth, Anders Tingberg.* Breast tomosynthesis - A novel three-dimensional X-ray imaging technique
- 16.40-17.00** *Yuri Dekhtyar, Alexei Katashev, Sergey Popov, Nina Rozanova.* Thermostimulated exoelectron emission of carbon doped Al₂O₃: potential application for microdosimetry
- 17.00-17.15** *Sören Mattsson.* Optically stimulated luminescence (OSL) for medical and environmental radiation dosimetry
- 17.15-17.30** *Maksims Polakovs, Nina Mironova-Ulmane, M. Grube, E. Reinholds.* Micro-Raman and infrared spectra of blood.

19:00-22.00 Get - together party
 "Perkūnas House", Aleksoto g. 6, Kaunas

Saturday, October 6, 2007

8.30-9.30 Registration of participants at **Kaunas University of Technology, Studentų g.50-103a, Kaunas.**

- 9.30-10.00** *Nina Mironova-Ulmane, Maksims Polakovs, Andrejs Pavlenko, Daina Piekstina, Tija Zvagule, Elvira Churbakova, Natalija Kurjane, Natalija Gabrusheva, Maja Eglite, Tiit Kärner.* Estimation of internal and external exposition in retrospective dosimetry of Chernobyl clean-up workers
- 10.00-10.30** *Christian Bernhardsson, Maria Christiansson, Irina Zvonova, Tanya Jesko, Slava Golikov, Christopher Rääf, Charlotte Thornberg, Sören Mattsson.* The radiation environment in Bryansk villages: 20 years after Chernobyl.
- 10.30-10.45** *Gediminas A. Adlys, Gediminas G. Adlys.* Modelling of mass cumulation processes of Cs-137 and Sr-90 in nuclear fuel

Coffee break 10.45-11.00

- 11.00-11.30** *Julius Žiliukas.* Dozės ir ploto sandaugos matavimų rezultatai gauti rentgenoskopijos tyrimu metu
- 11.30-12.00** *Inga Cibulskaitė, Marius Laurikaitis, Jurgita Laurikaitienė, Miglė Šniurevičiūtė, Birutė Gricienė, Aušra Urbonienė, Diana Adlienė.* MAMOLIT – database for patient's dosimetry in mammography screening examinations
- 12.00-12.15** *Vanda Andrijaitienė, Lina Vespenderytė, Mindaugas Zikas, Diana Adlienė.* Practical aspects of verification in gammatherapy
- 12.15-12.30** *Eglė Skripkaitė, Jurgita Laurikaitienė.* Evaluation of the instantaneous radioactivity concentration of Technetium-99m
- 12.30-12.45** *Eglė Garnytė, Marius Laurikaitis.* Linear accelerator shielding calculations
- 12.45-13.00** **Final remarks.** Moderator *Sören Mattsson*

ACCELERATOR MASS SPECTROMETRY (AMS) FOR PHARMACEUTICAL MICRODOSING STUDIES

Kristina STENSTRÖM*, Sören MATTSSON**

*Lund University, Department of Physics, Division of Nuclear Physics, Box 118, SE-221 00 Lund, Sweden; **Lund University, Department of Clinical Sciences Malmö, Medical Radiation Physics, Malmö University Hospital, SE-205 05 Malmö, Sweden

Abstract

Microdosing is a new concept in drug development that – if implemented in the pharmaceutical industry – would mean that new drugs can be tested earlier in man than today. The human microdosing concept may offer improved candidate selection, reduced failure rates and a reduction in the use of laboratory animals in early drug development, factors which will help to speed up drug development and also reduce the costs. However, pharmaceutical companies are still not routinely using the microdosing technique due to the lack of supporting data justifying the approach. This paper describes the principles for the microdosing concept by using the modern technology of accelerator mass spectrometry (AMS).

Keywords: Microdosing, accelerator mass spectrometry, AMS, drug development, ^{14}C

1. Introduction

Developing new drugs is a complex and very expensive process. Estimates suggest that today it takes on average 10-12 years to take a molecule through from discovery to regulatory approval for human use.

The very first step in drug development is to identify biological targets in the body which are believed to be associated with a specific disease. The next step is to find substances (chemical compounds) that interact with these targets to give a desired change in the behaviour of the diseased cells, tissues and organs. Promising compounds are taken further to prioritisation tests using cell cultures in test tubes (*in vitro*) and laboratory animals (*in vivo*). In this preclinical phase the potential drug must be extensively tested on animals to minimize the risk of potential harmful effects of the drug when eventually tested on humans. Safety, toxicity, pharmacokinetics and metabolism are parameters of the drug that need to be assessed. Also the physiochemical properties of the drug, such as chemical makeup, stability and solubility, need to be established.

After the preclinical tests, three phases of clinical tests follows. In Phase 1 probable candidates are tested on a limited number of healthy volunteers to evaluate the metabolic and pharmacological action of the drug in humans. Possible side effects of increasing doses are also studied. If the Phase 1 tests are successful, the

effects of a probable candidate are tested on patients along with safety tests (Phase 2). In Phase 3, trials are performed on large population groups. Before entering the market, the drug must be approved by the authorities (Medical Products Agencies).

Making development of new drugs less expensive and less time consuming is a matter of importance not only for bringing down the costs for the pharmaceutical companies. Reducing the costs and efforts would also imply cheaper drugs for the consumer, and make new drugs reach the market sooner than today to better treat various diseases. One problem of today's selection process of new drugs is that animal models are used in the early tests. Today a significant proportion of the drug candidates fail to pass the first human studies due to an unexpected pharmacokinetic behaviour in man, not predictable from the animal tests. In fact, it has been estimated that more than 70% of drugs entering clinical tests will not reach the market [1]. Today much of the costs for drug development are associated with those drugs that do not reach the market. Furthermore, there is a risk that drug candidates are rejected in the animal models, while they might actually have worked on man. Therefore, there is a need to simplify studies in humans, enabling tests in man early in the development process.

The *microdosing* concept could pose a solution [2,3]. Microdosing utilises sub-pharmacological single doses to open opportunities for early studies in man. Two modern technologies are used for microdosing:

accelerator mass spectrometry (AMS) and positron emission tomography (PET). PET and AMS are highly sensitive and complementary analytical methods, giving information on organ and tissue distributions as well as short-term retention of the compound (PET), and the long-term pharmacokinetics, metabolism and excretion (AMS). This paper focuses on the use of the AMS technique.

2. Microdosing with ^{14}C -AMS

The microdosing approach aims to test pharmaceuticals on the ultimate target species – man – earlier than today, by shortening the preclinical phase and include a new “Phase 0”. The basic idea behind microdosing is to administer a dose of the drug that is so low, that it is unlikely to produce any pharmacological effect or any adverse reaction. Yet the dose is high enough to enable studies the cellular response by sensitive measuring techniques, such as AMS using the radionuclide ^{14}C .

The microdosing concept has been recently been supported by the European Medicines Agency (EMA) in a position paper [4]. This document defines the non-clinical assessment – significantly reduced compared to what is required in traditional drug development – that must be done prior to the new Phase 0 studies using the microdosing technique. Also the U.S. Food and Drug Administration (FDA) has recently published guidance documents for the non-clinical safety tests prior to microdosing studies [5].

After the limited non-clinical safety studies, one or several lead candidates are lightly labelled with ^{14}C (generally a few kBq per candidate, physical half-life 5730 years) and administered to human volunteers at very low chemical doses ($<1\%$ of the pharmacological dose, but also $\leq 100\ \mu\text{g}$ of drug substance). Blood, urine and faecal samples are collected over time. The resulting samples (some chemically separated with chromatographic methods) are then analysed for ^{14}C content by AMS to determine the pharmacokinetic (PK) profile as well as absorption, distribution, excretion and metabolic (ADME) characteristics. The resulting radiation absorbed dose to the volunteer from the radioactivity of ^{14}C is very low, in fact only of the same amount as a few days of natural background radiation.

The data obtained from the microdosing studies is finally used when selecting which of the drugs to take further in the development process, opening for greater prediction versus animal and/or *in vitro* models. The microdosing approach would thus help to identify the promising candidates earlier than what is possible today, i.e. an improved candidate selection. The human microdosing approach also aims to reduce the failure rate at Phase I, since it ensures that drugs do not have to

be dropped later in the drug development process due to different pharmacokinetics in man compared to animal models. As a positive side effect, the human microdosing concept may also offer a reduction in the use of laboratory animals in early drug development.

Although the use of microdosing would mean that the compound can be tested earlier in man, due to lesser regulatory requirements for supporting toxicology tests in animals (and thus save time and money), pharmaceutical companies are still not routinely using the microdosing technique due to the lack of supporting data justifying the approach. A fundamental question of microdosing is whether the pharmacokinetics seen at microdose concentrations can be extrapolated to the much higher concentrations which are reached after a relevant pharmacological dose. In a recent trial called the CREAM trial, a comparison of pharmacokinetic parameters in a group of volunteers showed good correlation between micro- and therapeutic dose pharmacokinetics for 3 out of 5 common drugs [6].

Although the results of the CREAM trial look promising, further extensive evaluation studies of the microdosing concept are required. One such research programme, The European Union Microdose AMS Partnership Programme (EUMAPP), started in 2006 (ending in 2008) and is funded by the European Commission. Seven common compounds, the majority with well-known pharmacokinetics, will be administered to volunteers in a ^{14}C -labelled microdosing test, to evaluate if the microdose can predict the pharmacokinetics of the therapeutic dose. The main goal of the programme is to certify AMS as the most accurate, reproducible and appropriate analytical tool for microdosing studies.

3. AMS

AMS is a most sensitive measuring device as it can count individual atoms of certain long-lived radioisotopes – such as ^{14}C – and it does not rely on the rare radioactive decay events. At present there are over 50 AMS centres in the world, with applications in a diversity of research disciplines [7]. The most well-known and established application is probably radiocarbon dating of archaeological and geological samples, while microdosing is one of the newest.

As the name suggests, AMS is an extension of mass spectrometry (MS), a traditional method for determining the masses of specific positive or negative ions. In MS, the sample to be analysed is introduced into an ion source, which produces a positive or negative ion beam from the sample. The ions emerging from the ion source are generally accelerated in vacuum to energies in the keV range by a strong electric field. In the most basic MS system, a magnetic field applied perpendicular to

the ion beam will bend off different ions from the initial ion trajectory according to their mass to charge ratio (m/Z). A detector is used to register just one specific m/Z ratio at a time. By varying the magnetic field, a spectrum of various m/Z ratios is obtained, yielding information e.g. about the abundance of various ions, or isotopes, in the sample.

MS can however not be used for measurements of ^{14}C , because of an insufficient detection limit, and because of interfering atomic or molecular isobars, e.g. $^{14}\text{N}^+$ if using positive ions and $^{13}\text{CH}^-$ if using negative ions. However, the atomic isobar ^{14}N does not form negative ions, and no other element comprise of naturally occurring mass 14 isotopes (all are radioactive with extremely short half-lives). Thus, if using a negative ion source, the interference will only be negatively charged molecular isobars. The technique of AMS has the ability to prevent these interfering molecular isobars from reaching the detector of the AMS system, as described below.

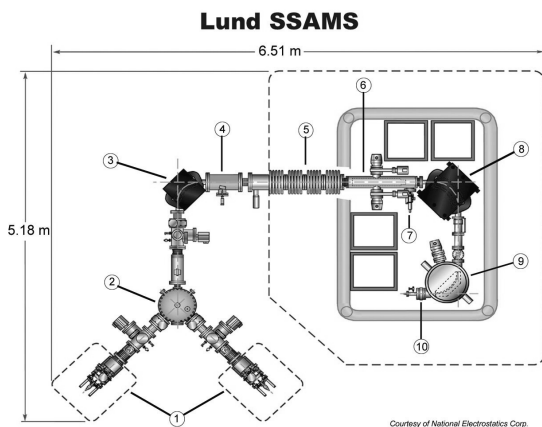


Fig. 1. The SSAMS system at Lund University.

- 1) Ion sources; 2) Rotatable spherical electrostatic analyzer (ESA); 3) Dipole magnet; 4) Einzel lens;
- 5) 250 keV accelerator; 6) Molecular dissociator;
- 7) Argon valve; 8) Dipole magnet; 9) Spherical electrostatic analyzer (ESA); 10) Sequential post-accelerator deflector (SPAD). The ^{14}C detector is placed at the end of the beam line (after the SPAD). Faraday cups for measuring $^{12}\text{C}^+$ and $^{13}\text{C}^+$ are placed in two offset positions just after the high-energy dipole magnet (8).

Fig. 1 shows an example of a modern, compact, high capacity AMS-machine of the single stage type (denoted SSAMS [8,9,10] located at Lund University. This SSAMS machine was put into operation in 2004 and is the first of its kind sold in the world. The system enables detection of ^{14}C through the following steps:

- 1) The carbon of the sample in question, e.g. blood, urine or faeces in microdosing studies, is extracted into elemental carbon. One common way of extracting the carbon from the samples is to oxidise the sample to CO_2 , which is then reduced by the

help of a heated metal catalyst and hydrogen gas to elemental carbon, see e.g. [11,12]. The required amount of carbon is generally in the range of 1 mg, but as little as a few tens of μg of carbon is even sufficient. The carbon samples are pressed into small aluminium holders and the samples are mounted into a 40-position sample wheel, along with standard samples of known ^{14}C content and blanks (the latter consisting of ^{14}C -free, fossil carbon, serving as background). Standards and blanks have also been processed through the same sample preparation system as the unknowns.

- 2) The sample wheel is introduced into the ion source of the AMS system, producing singly charged negative ions from the carbon samples (one at a time). The ion beam (about 40 keV) emerging from the sample being analysed will mainly consist of $^{12}\text{C}^-$ and $^{13}\text{C}^-$ at their natural abundances (approximately 99% and 1%, respectively), while atomic or molecular isobars to $^{12}\text{C}^-$ and $^{13}\text{C}^-$ will be negligible. Regarding ^{14}C , which AMS intends to quantify, typical orders of magnitude will be of the order of $10^{-8}\%$ to $10^{-12}\%$ in AMS analyses (the present day, natural ^{14}C abundance is about $10^{-10}\%$). Molecular isobars to $^{14}\text{C}^-$, e.g. $^{13}\text{CH}^-$ and $^{12}\text{CH}_2^-$, will be significantly more abundant than $^{14}\text{C}^-$. As seen in Fig. 1, the SSAMS system in Lund is equipped with two ion sources (only one is used at a time). The electrostatic deflector seen in the figure (no. 2) is used to select ion source and to improve the energy resolution of the injected beam.
- 3) A first mass selection is performed using a magnetic field (the dipole magnet no. 3 in Fig. 1), separating the masses 12, 13 and 14 into separate ion beams, the latter consisting mainly of $^{14}\text{C}^-$, but also of e.g. $^{13}\text{CH}^-$ and $^{12}\text{CH}_2^-$.
- 4) The separate mass-selected ion beams are sequentially accelerated to 250 keV in the SSAMS system in Fig. 1. Other types of AMS systems use tandem accelerators and energies of up to several MeV [7].
- 5) The energy of the ions, gained at the acceleration step, is now high enough to allow dissociation of the molecules into their elemental constituents by collision processes. This is done by letting the ions pass through the molecular dissociator (no. 6 in Fig. 1), which contains a very thin gas of Ar. Apart from the molecular dissociator, the whole ion path from ion source to detector is under high vacuum. After the molecular dissociator, the charge state of the ions has changed from -1 to on average +1.
- 6) The former molecular isobars, which now have been split up into positively charged elemental

fragments, are removed from the mass 14 beam by magnetic and electric fields (nos. 8 and 9 in Fig. 1).

- 7) ^{14}C is finally detected in the particle detector at the end of the beam line. Faraday cups for measuring $^{12}\text{C}^+$ and $^{13}\text{C}^+$ are placed in two offset positions just after the high-energy dipole magnet (no. 8 in Fig. 1). The ^{14}C specific activity of each sample is determined by correcting the measured $^{14}\text{C}/\text{C}$ ratios for background (using the blanks), and comparing the $^{14}\text{C}/\text{C}$ ratios to those of the standard samples of known activity (also corrected for background). For samples from microdosing studies, the obtained ^{14}C specific activity of each sample used as a basis when determining PK and ADME data.

The SSAMS system at Lund University is, apart from microdosing studies, devoted to radiocarbon dating, biomedicine and environmental samples. For mg-sized carbon samples it has a precision of 5‰ for the $^{14}\text{C}/^{12}\text{C}$ ratio, and a background of about 2‰ (corresponding to an age of 50000 ^{14}C years) relative the modern standard for an infinite-aged graphite sample (Skog 2007). For microdosing studies, each ^{14}C measurement only takes a few minutes of measuring time, once the SSAMS system has started up (which takes a few hours). Alike most modern AMS instruments, the SSAMS system is fully automatic, but requires skilfully trained personnel to tune the apparatus before measurement. The sample preparation is more time and labour consuming than the actual AMS measurement.

The main advantage of the AMS method is its extremely low detection limit: less than 1 μBq of ^{14}C can be quantified per mg-sized carbon sample. Decay counting techniques, such as liquid scintillation counting (LSC), are far from reaching these low levels. However, as the greatest advantage of the AMS technique is the low detection limit, its worst enemy becomes contamination. ^{14}C has been, and still is, frequently used as a tracer (for LSC measurements) in many biological laboratories, and in concentrations that are very high in perspective of the sensitive AMS method. Therefore extreme precaution must be taken to avoid handling AMS samples in labs with a ^{14}C history. In a microdose study, isotope ratios range over several orders of magnitude: from dosing solutions to volunteers – that contain kBq of ^{14}C – down to single biological samples that may contain mBq, or even μBq , of ^{14}C . It is thus of utmost importance to organize the work to avoid contamination (e.g. use different labs for high- and low-activity solutions and samples) in order to keep the sample integrity. A drawback of the AMS technique is that it is still a rather expensive technique.

4. Summary and conclusions

The possibility to assess drug pharmacokinetics in early trials in humans is of great importance in drug development. Human trials remain the best alternative for selection or rejection, and although molecular biology has developed fast, methods in this field can usually not predict well the drug behaviour in humans. Microdosing on humans may offer a solution, resulting in that a range of studies in animals may be avoided and that the focus can be directed on promising candidates. Eventually, this will save time as well as money for the whole society.

Microdosing relies on sensitive measurement techniques such as AMS. AMS itself is a well-established tool for determining the abundance of ^{14}C in various organic materials. The question that remains to be answered is if the microdosing concept itself is able to predict the behaviour of therapeutic doses.

5. References

1. DiMasi A. Risks in new drug development: approval, success rates for investigational drugs. *Clin. Pharm. Ther.* 69 (1996) 297-307.
2. Lappin G. and Garner, R.C. Big physics, small doses - the use of AMS and PET in human microdosing of development drugs. *Nature Reviews (Drug Discovery)* 2 (2003) 233-240.
3. Garner R.C. and Lappin G. The phase 0 microdosing concept. *B. J. Clin. Pharmacol.* 61:4 (2006) 367-370.
4. European Medicines Agency. Position paper on non-clinical safety studies to support clinical trials with a single microdose, 2004, CPMP/SWP/2599/02/Rev1.
5. Center for Drug Evaluation and Research. Guidance for industry, investigators and reviewers: exploratory IND studies. Draft guidance. US Dep. of Health and Human Services, Food and Drug Administration, Center for Drug Evaluation and Research. 2004.
6. Lappin G. et al. Use of microdosing to predict pharmacokinetics at the therapeutic drug: Experience with 5 drugs. *Clin. Pharm. Ther.* 50:3 (2006) 203-215.
7. Fifield L.K. Accelerator mass spectrometry and its applications. *Rep. Phys. Prog.* 62 (1999) 1223-1274.
8. Klody G.M., Schroeder J.B., Norton G.A., Loger R.L., Kitchen R.L. and Sundquist M.L. New results for single stage low energy carbon AMS. *Nucl. Instr. Meth. B* 240:1-2 (2005) 463-467.
9. Schroeder J.B., Hauser T.M., Klody G.M. and Norton G.A. Initial results with low energy single stage AMS. *Radiocarbon* 46:1 (2004) 1-4.

10. Skog G. The single stage AMS machine at Lund University: Status Report. Nucl. Instr. Meth. B259 (2007) 1-6.
11. Getachew G., Kim S.-H., Burry B.J., et al How to convert biological carbon into graphite for AMS. Radiocarbon 48:3 (2006) 325-336.
12. Hua Q., Jacobsen G.E., Zoppi U., Lawson E.M., Williams A.A., Smith A.M. and McGann M.J. Progress in radiocarbon target preparation at the Antares AMS Centre. Radiocarbon 43:2A (2001) 275-282.

THE APPLICATION OF CHLORIN e_6 PHOTOBLEACHING IN THE DOSIMETRY OF PDT

Mindaugas TAMOŠIŪNAS¹, Martynas PLUKYS¹, Saulius BAGDONAS¹
Gražina GRAŽELIENĖ² and Ričardas ROTOMSKIS^{1,2}

¹ Vilnius University, Faculty of Physics, Dept. of Quantum Electronics, Saulėtekio 9, c.3, LT-10222 Vilnius, Lithuania;

² Institute of Oncology, Vilnius University, Santariskiu 1, LT-08660, Vilnius, Lithuania

Abstract

In this study the possibility to relate the photobleaching of the sensitizer with the tumour response to PDT treatment was explored. The tumour-bearing mice were sensitized with chlorin e_6 and irradiated with a diode laser (654 nm), applying the different fluence rates. The fluorescence intensity decay at the surface or in the volume of tumour was used for modelling the PDT effect in different depths of tissue.

Keywords: Chlorin e_6 , dosimetry, fluorescence, photobleaching, photosensitized tumour therapy.

1. Introduction

Photosensitized tumour therapy (PDT) is a relatively new therapeutic modality, which involves the activation of the molecular oxygen under irradiation by light in the presence of certain photodrugs (photosensitizers) that have been selectively accumulated in the target tissue. The mechanism of light-induced degradation of cancerous tissue during the PDT involves the presence of reactive species, singlet oxygen, which, as a rule, are generated by the sensitizer. However, the produced singlet oxygen can damage not only cancerous cells but also destroy the sensitizer itself.

Light degrades most of the photosensitizers that have been used in the photosensitized tumour therapy. This process termed “photobleaching” can occur with dyes present in solutions, cells and in tissue and can be detected by measuring (decrease in intensity of) the sensitizers’ absorbance and fluorescence signal. The photobleaching of photosensitizer reflects the efficacy of singlet oxygen generation as well as the other dosimetry factors (which could not be measured directly) and can be used for the estimation of the optimal phototherapeutic dose [1].

During this study the photobleaching of the sensitizer measured on the surface of tumour as well as in the volume of tumour had been investigated in order to provide the relevant criterion of tissue response to PDT treatment.

2. Materials and methods

C57B1/CBA hybrid mice (8–10 weeks old, weight range 21–27 g), bearing either hepatoma A22 (MH-A22) or adenocarcinoma LLC in the right haunch were used. The experiment started 10 days after the inoculation of malignant cells (approximately 1×10^6 /mice), when the average volume of the growing

tumour reached $\sim 300 \text{ mm}^3$ ($13 \times 8 \times 6 \text{ mm}$). The mice received the food without the chlorophyll compounds during the experiment time as well as a week before. All mice were subjected to the control measurements of autofluorescence before the injection of the photosensitizer. The hair from the area of the measurement was removed 24 hr. before the experiment using depilatory cream.

The fluorescence spectra were measured using the optical fibre spectrofluorimeter *S2000-FL* (*Ocean Optics*) equipped with a 2048 element linear CCD array detector and connected to a personal computer (Fig. 1). The light for the fluorescence excitation ($\lambda_{\text{ex}} = 405 \text{ nm}$, LED) was delivered through the central fibre of the bundle (SOMTA, Riga, Latvia) and the ring of six identical fibres was used for the fluorescence collection. The 128 nm band pass filter (centred at 358 nm) was placed in front of the LED to remove the residual illumination in the longer wavelengths. A long pass filter ($T_{477 \text{ nm}} = 50\%$) was inserted into the detection light path in order to cut off the scattered excitation light while allowing the fluorescence to pass through.

Chlorin e_6 ($C e_6$) obtained from the Institute of Molecular and Atomic Physics of the Belarusian Academy of Sciences (Minsk, Belarus) was dissolved in 0.9% saline just before the injection and 0.2 ml of solvent was administrated intravenously into the tail vein of mice at a concentration of 10 mg/kg. The animals were divided in three groups: I – control group (3 mice for autofluorescence measurements *ex vivo*); II – sensitized group (9 mice, non irradiated); and III – PDT group (18 mice, sensitized and irradiated).

The distribution of $C e_6$ fluorescence in the sensitized group was examined. The mice were killed 4

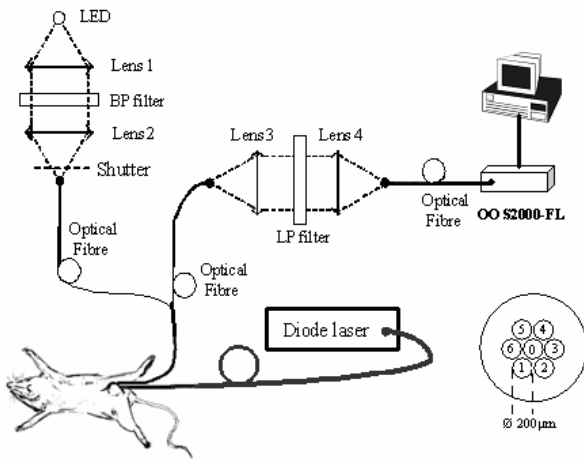


Fig. 1. Schematic diagram of the experimental setup: Excitation fibre (0); Fluorescence collection fibres (1-6); L1-L4 lenses; BP – band pass filter, LP – long pass filter; OO S2000-FL – spectrofluorimeter.

hr. following the intravenous administration of C_{e_6} (six mice bearing hepatoma A22 (MH-A22) tumour and three mice with adenocarcinoma LLC tumour). The tumours were excised from mice, cut in two equal pieces and squeezed between two glasses. The fluorescence measurements of the surface of tumour section (and outer surface as well) were performed. The dependence of the fluorescence intensity of C_{e_6} on the corresponding point of the tumour specimen evidenced the distribution of C_{e_6} in tumour tissue.

In the PDT group, the tumours *in vivo* were irradiated with laser ($\lambda = 654 \text{ nm}$) using fluence rates of 90 mW/cm^2 (light doses 2.25 J/cm^2 , 36 J/cm^2) and 612 mW/cm^2 (189 J/cm^2), 3-4 hours after the administration of chlorin e_6 . Six extra mice were used to reveal the dependence of C_{e_6} fluorescence intensity decay on irradiation time using the fluence rates of 1 mW/cm^2 , 5 mW/cm^2 and 10 mW/cm^2 . Fluorescence intensity decay measurements at the point of irradiation were performed during the treatment procedure. Due to that, the irradiation became fractionated as the dark interval of about 2-3 min. was required to measure the fluorescence. Light doses of 2.25 J/cm^2 and 189 J/cm^2 were applied for hepatoma A22 (MH-A22) tumours (six mice for each light dose) and the rest six adenocarcinoma LLC tumours were irradiated with 36 J/cm^2 . Immediately after the treatment all tumours were excised from the mice and divided in two pieces along the main plane of light penetration into tissue. Fluorescence scanning of the inner surface of the tumour cuts was performed along to the direction of incident laser beam. During the measurements *ex vivo*, all samples were mounted on a stable basement with a micrometric screw in order to keep the conditions of fluorophore excitation and emission unchanged. The step of 0.5 or 1 mm was used for scanning of the tumour

specimen in xy directions of the cut plane (see the details in Fig.4, b and c).

The fluorescence intensity of C_{e_6} was calculated after the subtraction of autofluorescence spectra (*in vivo*) or the numerical values of autofluorescence intensity at 665 nm (*ex vivo*) from the original data obtained in groups II and III.

The depth of light penetration into the tumour tissue was estimated measuring the intensity of the backscattered light in the tumour section. The optical fibre was immobilized in a close distance to the surface of tumour and the laser irradiation ($\lambda = 654 \text{ nm}$, $P=1.27 \text{ mW}$) was performed. The pictures of the tumour section were obtained using CCD camera (Telecam SL, Endovision, Karl Storz) connected to the image processor (Argus 20, Hamamatsu, Japan) and personal computer. Several accumulation times (1/2000 s, 1/1000 s, 1/500 s, 1/60 s, 1/30 s, 1/15 s, 1/8 s) were selected, so the system could detect the changes of the light intensity starting at the different distances from the irradiated surface. The images were further processed using Argus20 software and the dependence of the signal intensity on the distance from irradiated surface (defined as the tumour depth) was obtained.

3. Results and discussion

The fluorescence spectra *in vivo* were measured from the skin above the tumour tissue. Under the excitation at 405 nm, broad and non structured autofluorescence bands were detected in all fluorescence spectra at the region of 500–800 nm. A narrow emission band peaking at 665 nm was characteristic for the fluorescence of injected C_{e_6} (Fig.2).

The study of the sensitizers' accumulation at the tumour surface evidenced that the maximal fluorescence intensity of C_{e_6} was observed up to 4 hr. post injection (p.i.), and the maximal fluorescence ratio between tumour and healthy tissue was found between 3 and 8 hr. p.i. [2]. These findings based our choice to start the photodynamic treatment 3-4hr. after injection of C_{e_6} . The illumination of the sensitized tumour tissue with red light resulted in fast decay of C_{e_6} fluorescence (Fig. 2). Assuming that the mechanism of the photobleaching is coupled to the reactive oxygen, the observed decrease in C_{e_6} fluorescence indicates the destruction of C_{e_6} molecules. For the non coupled photobleaching, however, the observed spectral changes may be interpreted as the relocalization of the photo-sensitizer, e.g. it may become non fluorescent after the interaction with the changed cellular environment.

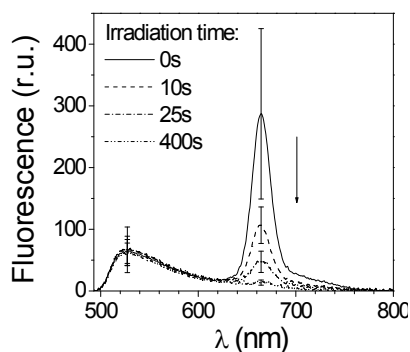


Fig. 2. Fluorescence spectra of C_{60} : before (0s) and after laser irradiation (10 s, 25 s and 400 s). Data are presented as the average \pm standard deviation.

Fig. 3 shows the fluorescence intensity of C_{60} plot as a function of the irradiation time for the different fluence rates applied (from 1 mW/cm^2 to 612 mW/cm^2). The obtained results revealed that the photobleaching of C_{60} increased with the higher fluence rates applied reaching the similar initial rates (τ_1) starting from about 90 mW/cm^2 . The dependence of the same results on the light dose is presented in Fig. 3, insert. The fluorescence intensity decay of C_{60} showed no dependence on fluence till it almost stopped responding to the fluence rate. The slope of the photobleaching curve started to increase at the fluence rate of 90 mW/cm^2 and followed the same pattern at 612 mW/cm^2 with even less photobleaching of C_{60} observed for the total light dose. It is obvious that the photobleaching of the sensitizer (e.g. coupled with the activation of the molecular oxygen) is proportional to the initial number of photons, but it is also dependent on the oxygen concentration in tissue. At the higher fluence rates, the photochemical depletion of the tissue oxygen occurs and the photobleaching becomes unresponsive to the fluence rate. But mathematically, the fluence rate is incorporated into the light dose metric, and the higher irradiance still means the higher light dose delivered. So that is the reason for the different behaviour of the bleaching kinetics at the higher fluence rates.

Light dose of 2.25 J/cm^2 reduced the initial fluorescence intensity of C_{60} at the surface of tumours *in vivo* for 85% (Fig 4, a). The fractionated mode of irradiation was further applied in order to deliver the light dose of 36 J/cm^2 thus reducing the fluorescence intensity for 97% of the initial level. The same ratio of the fluorescence intensity measured after the irradiation to the initial fluorescence intensity ($F(t)/F(0)$) was obtained for the light dose of 189 J/cm^2 using 6.8 time higher fluence rate.

The depth of C_{60} photobleaching *ex vivo* was estimated by comparing the pattern of fluorescence distribution after the irradiation of tumours with the fluorescence distribution in sensitized non irradiated tumours. The results revealed that C_{60} had been already

accumulated in the periphery and the central part of hepatoma A22 (MH-A22) and adenocarcinoma LLC

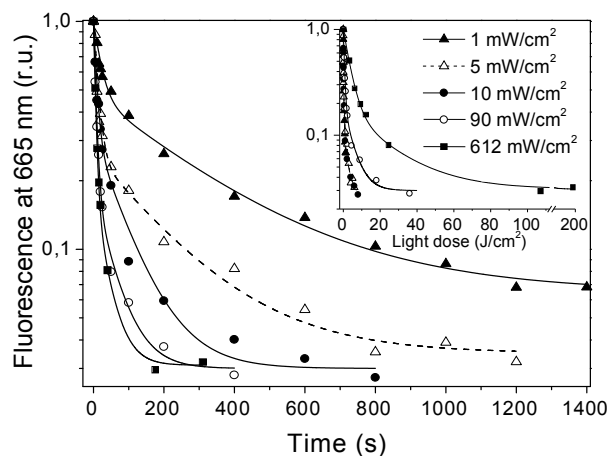


Fig. 3. The dependence of C_{60} fluorescence intensity decay on irradiation time and irradiation dose (insert) at a different fluence rates. The experimental data was approximated by two-exponential decay curves with the half lifes: $\tau_1=20\pm 1\text{s}$, $\tau_2\approx 318\text{s}$ (1mW/cm^2); $\tau_1=10.5\pm 1.1\text{s}$, $\tau_2\approx 207\text{s}$ (5mW/cm^2); $\tau_1=8.4\pm 1\text{s}$, $\tau_2\approx 89\text{s}$ (10mW/cm^2); $\tau_1=6.8\pm 0.6\text{s}$, $\tau_2\approx 56\text{s}$ (90mW/cm^2); $\tau_1=5.7\pm 0.6\text{s}$, $\tau_2\approx 37\text{s}$ (612mW/cm^2);

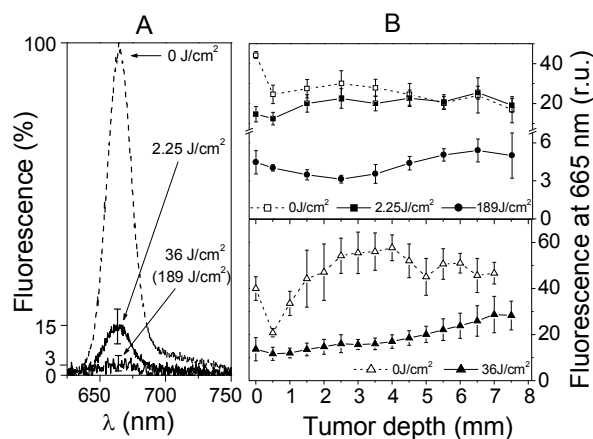


Fig. 4. Photobleaching of C_{60} on the surface of the tumour *in vivo* (A) and the variation of the sensitizer's bleaching in tumour volume, *ex vivo* (B) after the different light doses applied. Data are presented as the average \pm standard deviation (A) or standard error (B).

tumours, 4 hr. post i.v. injection. However, the pattern of the initial photosensitizer distribution was different. The highest fluorescence of C_{60} was detected at the superficial point for hepatoma A22 (MH-A22) tumour, in contrast to the lower fluorescence values detected till a depth of 1mm for adenocarcinoma LLC, see the control curves in Fig. 4, B. That can be explained by the differences in tumour morphology. The lung adenocarcinoma cells have the higher proliferation potential at the surface as compared to that in the central

part of tumour [3]. Therefore, the vascular net needs to be constantly developed at the surface, in order to maintain the cell metabolism. Assuming that the amount of accumulated sensitizer is proportional to the state of vasculature, the surface region of the decreased $C e_6$ fluorescence for adenocarcinoma LLC may represent the actively proliferating area with incomplete vascular system. The absorbance of the excitation light by the blood haemoglobin is lower at the superficial point, which is possibly the reason of the relatively increased fluorescence being detected there.

The fluorescence scanning performed along the direction of incident light beam after the resection of tumours revealed that the fluorescence intensity of the spots depended on the distance from the irradiated surface. Lower fluorescence intensity was detected at the tumour exterior (defined as the minimal tumour depth in Fig. 4, B) while the opposite part of the tumour for each fluence applied was less affected by light. After the irradiation with fluence of $2.25 J/cm^2$ the reduced fluorescence of chlorin e_6 was detected till a depth of 0.5 mm from the surface of tumour. Much more of the photosensitizer was bleached when the light doses of $36 J/cm^2$ and $189 J/cm^2$ were applied. Although there were traces of fluorescence recurrence in the depth of tumour, in the latter case the levels of the remained fluorescence intensity did not match the control ones at any point.

The ability of light to penetrate the tumour was also represented by the profile of $C e_6$ photobleaching obtained *ex vivo*. When the light beam is directed to the tissue sample, the photons may be reflected, scattered in

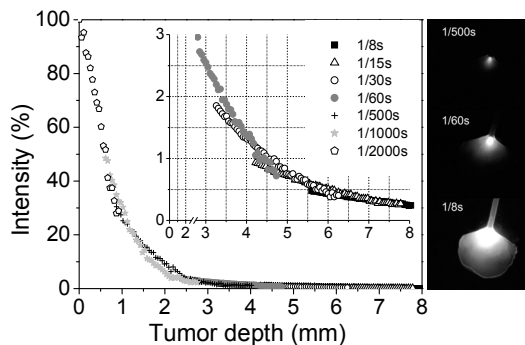


Fig. 5. The dependence of the light intensity decay on the distance from the irradiated surface of tumour.

the tissue volume or be absorbed by chromophores. Generally that results in the attenuation of light intensity inside the tissue following the direction of irradiation and the formation of the inner front surface corresponding to each discrete fluence rate. The pictures of the distribution of backscattered light from the tumour tissue obtained *ex vivo* (Fig. 5, right panel) may provide the direct information about the depth of light penetration. According to our data, the attenuation of light intensity in tumour tissue (estimated parallel to the

incident irradiation) followed the monoexponential approach with $\tau = 0.69 \pm 0.02$ mm, Fig. 5. Proportionally to the changing number of photons in the volume of tumour, the decrease of $C e_6$ fluorescence becomes non uniform: a fluorescence signal of $C e_6$ should remain more intense deeper in the tumour and more of the sensitizer should be bleached at the surface; that was actually observed *ex vivo* (for the light doses of $2.25 J/cm^2$ and $36 J/cm^2$), Fig. 4 B. The bleaching profile of $C e_6$ *ex vivo* was also affected by the dependence of the photobleaching rates (τ_1, τ_2) on the fluence rate (Fig. 3, main panel). It means that if tumour fluorescence is compared at two points that limit the depth where τ is weakly affected by the fluence rate, the decrease of the fluorescence signal of $C e_6$ would be the same there.

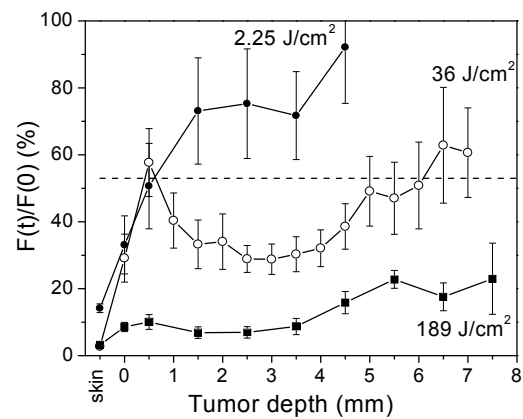


Fig. 6. The decay of $C e_6$ fluorescence obtained in various depths of the tissue. The first point (skin) was made by the non-invasive measurement and the last points were derived by dividing the fluorescence of irradiated and control tumours *ex vivo*. Data are presented as the average \pm standard error.

The PDT effect on tissue was estimated from the ratio $F(t)/F(0)$, which was obtained either at the surface of tumour or in the tumour volume (Fig. 6). The morphological study made for the reference evidenced that the tumour necrosis occurred up to 0.6 mm (on average) from the irradiated surface when the light dose of $2.25 J/cm^2$ was applied [4]. That marks the intersection point between the photobleaching curve ($2.25 J/cm^2$) and the dashed line $F(t)/F(0)=53\%$, Fig. 6. Generally it means that if we measure the fluorescence at the depth x in tumour, the irradiation with the fluence rate of $90mW/cm^2$ will result in the necrosis at this point of interest, when the intensity of $C e_6$ fluorescence decreases twice. The depth of necrosis further increases with the light dose. According to our model, the light dose of $36 J/cm^2$ ($90mW/cm^2$) should induce the necrosis till the depth of about 6 mm. But in the latter case note the point at the depth of 0.5 mm, which signals that some parts of the tumour could be intact there. As the lower amount of the photosensitizer was

accumulated at this depth (Fig. 4, B), the principle of to be sustained only by the additional irradiation to increase the light dose. Alternatively, the preliminary prognosis of tumour destruction during PDT could be obtained from non invasive measurements. After the irradiation, the 85% fluorescence decrease at the surface of tumour will indicate the tumour necrosis till a depth of 0.6 mm and that of 97% – till a depth of 6 mm from the surface. But this approach is valid only for the tumours with the homogenous distribution of the sensitizer and the fluence rates till about 90 mW/cm². As the fluence rate was increased (resulting in the increase of the total light dose) the decrease of superficial fluorescence remained the same, 97%. Moreover, in this case the bleaching data obtained *ex vivo* indicated the complete destruction of the tumour volume ($F(t)/F(0) < 53\%$), but that was not confirmed histologically [4]. In this case, the depletion of tissue oxygen might affect the obtained results. And because of the enhanced possibility for the non-coupled photobleaching (the loss of the fluorescence, which is not involved in the photodynamic effect) the different threshold values of $F(t)/F(0)$ should be selected, considering the conditions of irradiation.

the equivalentum of the total phototherapeutic dose has

4. Conclusion

Fluorescence decay of chlorin e_6 could be used as a parameter for the evaluation of tumour response to PDT treatment.

5. References

1. Wilson B.C., Patterson M.S. and Lilge L. *Lasers Med. Sci.* 1997, 12(3), p. 182-199.
2. Tamošiūnas M., Bagdonas S., Didžiapetrienė J. and Rotomskis R. *J. Photochem. Photobiol. B: Biol.* 2005, 81(2), p. 67-75.
3. Shoji M., Dobashi Y., Morinaga S., Jiang S.X. and Kameya T. *Am. J. Pathol.* 1999, 154(3), p. 909-918.
4. Strazdaitė V., Aleksandravičienė Č., Tamošiūnas M., Bagdonas S., Didžiapetrienė J. and Rotomskis R. *Acta Bio-Opt. Inform. Med.* 2004, 10, p. 41.

NON INVASIVE DIAGNOSTIC METHOD FOR THE DETECTION OF NON SUPERFICIAL LESIONS

Jonas VENIUS, Ričardas ROTOMSKIS
Vilniaus universitetas, Fizikos fakultetas, Saulėtekio al. 9, LT-10222 Vilnius

Abstract

Early diagnostics is the key to the successful treatment. One of the most suitable opportunities is optical methods. However, signal detection from deeper layers is problematic. It was shown that multifiber systems could be used for depth resolved fluorescence detection. Our results indicate that using multifiber system is possible to register fluorescence mostly from the deeper layers and to monitor the change of the layers thickness. Also it was obtained a reference curve for the approximate evaluation of the fluorescing layer's depth.

Keywords: Non invasive diagnostics, optical biopsy, depth resolved fluorescence, multidistance

1. Introduction

Successful treatment of the disease foremost depends on the curing method itself. The second equally important factor is the precise identification of the disease or the detection of the damaged areas. In some cases, especially in oncological disorders, early diagnostics is the key to the successful treatment of the disease [1]. In order to make diagnostics a simple, cheap and daily procedure informative but rather simple methods needs to be employed. Nowadays optical diagnostic techniques, also known as optical biopsy, are widely used in many areas of medicine due to non-invasive approach and instant performance [2]. Majority of these methods are based on the fluorescence measurements, which reflect molecular, biochemical and structural composition of the tissue, but are quite simple to perform. Thus non invasive but very informative optical methods are one of the most suitable opportunities for the early diagnostics.

In conventional optical biopsy the detected signal is a mixture of fluorescence signals originated in various depths, therefore no information about spatial structure and composition of the tissue is obtained. Most of the signal is composed from the upper layer's fluorescence and sometimes it drowns the useful information coming from the tissue inside. Some of the cancerous diseases originate deeper in the epithelial tissue, therefore the most valuable information is from the deeper layers [3]. Signal from the deeper layers is weak due to the light scattering, but scattering also allows photons, originated deeper in the tissue, leave the medium at higher distances from the point of light incidence into the tissue, whereas photons, originated in the superficial

layers, will escape the medium at smaller distances. Therefore, the distribution of fluorescence intensity registered on the tissue surface at different registration distances contains information about the depth dependent distribution of the fluorophores in the tissue. Such distribution could be obtained using a multifiber system (Fig.1).

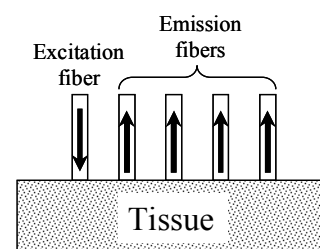


Fig.1. A multifiber system for the depth resolved fluorescence measurements.

The system consists of a single fiber and multiple registration fibers located at various distances from the illumination fiber. Zhu et al. theoretically investigated the properties of such system by Monte Carlo simulation method. The researchers concluded that such multidistance fiber system is more useful in detecting fluorescence from the deeper layers as compared to conventional single fiber systems [4]. Also it was shown experimentally, that fibers, which are close to the excitation fiber, are more sensitive to the superficial layers, while fibers, located at some distance, are more sensitive to the deeper layers [5].

The goal of this study was to characterize the spatially resolved fluorescence from the modeled turbid medium

identifying the conditions for the estimation of the fluorescing layer depth.

2. Materials and methods

A layered turbid medium was simulated for the depth resolved fluorescence measurements. It was realized by means of the special multi-compartment cuvette (Fig.2).

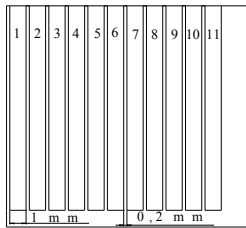


Fig. 2. A special cuvette for the simulation of multilayered structures.

The compartments were filled with milk-based scattering medium and fluorescing layers were realized by refilling the appropriate compartments by fluorescing material. In our experiments CdSe/ZnS quantum dots (QD) were used as fluorescing agents. We used two types of QD: QD₁ ($\lambda_{em} = 540$ nm) and QD₂ ($\lambda_{em} = 620$ nm). Fluorescence of QD was excited by the light emitting diode (470 ± 10 nm). A multifiber system for fluorescence registration was realized by a special fiber optic probe, which consists of 9 fibers that closes in one

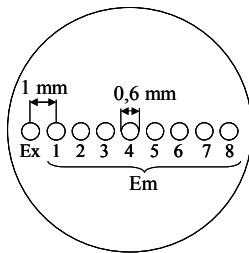


Fig. 3. A tip of the multidistance fiber.

tip (Fig.3). The diameter of each fiber is $600 \mu\text{m}$ and spacing between them is 1 mm (center to center distance). The Ex fiber is used for excitation and the Em fibers – for collecting the emission. During the experiments the tip was placed at the front wall of the cuvette that was considered to be the surface of the medium. Fluorescence spectra were recorded by fiber spectrometer S2000-FL (Ocean optics).

3. Results

The initial task was to characterize the spatially resolved fluorescence.

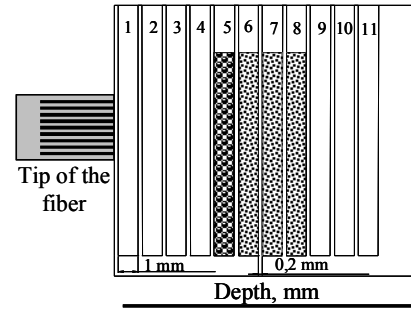


Fig. 4. A multilayered turbid medium. 0-4mm scattering medium, 4-5mm QD₁, 5-8 mm QD₂.

For this purpose a turbid medium with fluorescing layers at a certain depths was modeled (Fig.4). For the first experiments two different fluorescing layers were embedded in 4-7 mm depth. The upper layer (1 mm thick) was made from QD₁ and the second (3 mm thick) was made from QD₂. In front of the fluorescing layers was the scattering medium (1-4 mm). Fluorescence spectra registered at different distances from the excitation fiber are depicted in Fig.5.

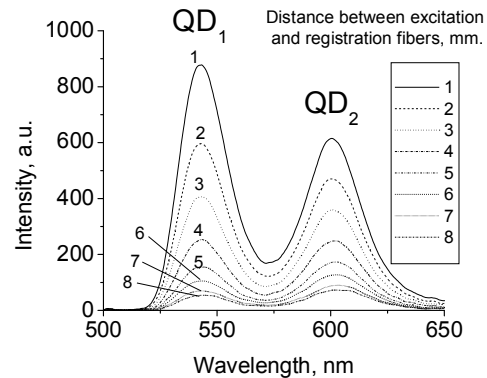


Fig. 5. Fluorescence spectra registered at different distances from the excitation fiber.

The nearest fiber (fiber No.1) detected an intense fluorescence from the first layer and less intense from the second layer. The 2nd and the 3rd fibers registered similar distributions, but fluorescence from the second layer almost reached the intensity registered from the first layer. At the registration distance of 4 mm fluorescence intensities registered from the deeper and from the upper layers became equal. According to the theory, when the fluorescence occurs deeper in the tissue the emitted photons will reach the surface more spread, while the photons emitted near the surface will be more concentrated. Therefore the fluorescence from the first layer reaches mostly the closest fibers, while fluorescence from the second layer is able to reach further fibers. Following this, fibers situated more than 4 mm away from the excitation fiber more intense

fluorescence registered from the deeper layer. To show this effect more clearly it is useful to calculate the ratio between the peak intensity values of QD₂ and QD₁ fluorescence bands. The calculated ratio $I(QD_2)/I(QD_1)$ is plotted in Fig.6.

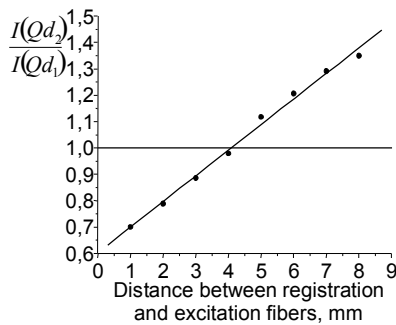


Fig. 6. The ratio between the peak intensity values of QD₂ and QD₁ fluorescence bands.

At the registration distance of 1 mm QD₁ fluorescence is ~ 1,4 times higher than QD₂ fluorescence, and at the registration distance of 8 mm the deeper layer (QD₂) has ~1,35 times higher fluorescence than the upper layer (QD₁). This phenomenon could be used for the evaluation of the localization of the fluorescing layer in regard to the other fluorescing object. Fluorescence measured at 1 and 8 mm distances from the excitation fiber should indicate which of the fluorescing objects is deeper. Also it should be possible to detect the dynamics of the thickness of the fluorescing layer, what could be useful in photodynamic tumor therapy to observe the accumulation of the sensitizer. To verify this hypothesis we simulated the change of the fluorescing layers thicknesses. The thicknesses were changed in respect to the previous experiment. QD₁ layer now was in 4 - 6 mm depth and QD₂ layer from 6 to 8 mm. In this way the upper layer (QD₁) was made thicker, while the next layer (QD₂) became thinner (Fig.7).

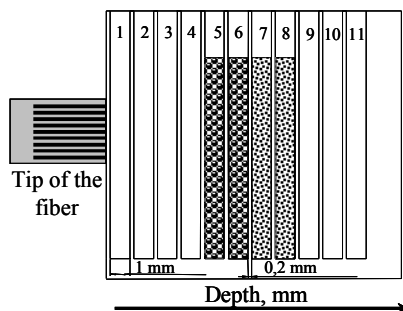


Fig. 7. A multilayered turbid medium. 0-4mm scattering medium, 4-6 mm QD₁, 6-8 mm QD₂.

Fluorescence spectra measured at different distances from the excitation fiber are represented in Fig.8.

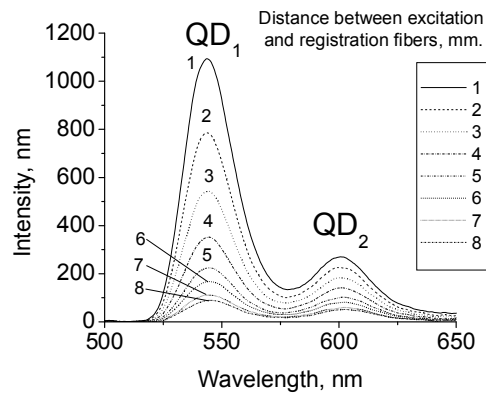


Fig. 8. Fluorescence spectra registered at different distances from the excitation fiber.

In all spectra the fluorescence from the first layer is more intense than fluorescence from the deeper layer. This could be explained by the fact, that additional QD₁ layer was added underneath, what resulted in increased fluorescence intensity, especially in the further fibers. On the other hand QD₂ layer was made thinner from above, what resulted in decreased fluorescence, especially in the nearest fibers. To show this more clearly the ratios of fluorescence intensities were calculated. The ratios represent how much the intensities of QD₁ or QD₂ layer fluorescence have changed after the thickness change. R₁ represents the change of fluorescence intensity of QD₁ layer measured at the 1st fiber and R₂ represents the change of fluorescence of QD₁ layer measured at the 8th fiber. After the thickness change the fluorescence of QD₁ layer became more intense. In the 1st fiber intensity raised 1,24 times (R₁ = 1,24) and in the 8th fiber 1,65 times (R₂ = 1,65). This is logical since the nearest fibers are more sensitive to the upper layers and furthest fibers – to the deeper layers. The QD₁ layer was added underneath what resulted in higher fluorescence increase in further fibers. The same findings could be observed for the deeper QD₂ layer. After the change fluorescence of this layer became less intense. In the 1st fiber intensity decreased 2,3 times (R₃ = 2,3) and in the 8th fiber 1,4 times (R₄ = 1,4). This is also logical since the nearest fibers are more sensitive to the upper layers and the QD₂ layer was removed from above what resulted in higher fluorescence decrease in nearest fibers. These results enhance the potential of multifiber systems to be used for depth resolved diagnostics and for the evaluation of the fluorescing layers thickness.

More significant task than monitoring the dynamics of fluorescing layers is to determine the depth in which the fluorescing object is located. For this task the depth

resolved fluorescence of one layer (QD₂) was measured for six different depths. Fluorescing layer QD₂ in the cuvette was moved down from 1 to 6 mm and fluorescence was measured for each depth. In this case the most significant information in the fluorescence spectra is the peak intensity of the fluorescence band (intensity at the fluorescence maximum of quantum dots – at 620 nm). It is more valuable to present the peak intensity registered at eight different distances instead of representing the entire fluorescence spectra (Fig.9).

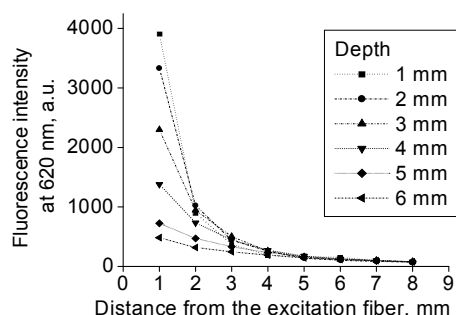


Fig. 9. Peak intensity registered at eight different distances. Depth was changed from 1 to 6 mm.

Each depth now can be characterized by a set of numbers that represents the peak intensities registered at eight different distances from the excitation fiber. The distribution of fluorescence intensities registered on the surface of the medium has the shape of the first order exponential decay $y = y_0 + A_1 e^{-x/t}$. The decay coefficient t was calculated for all depths.

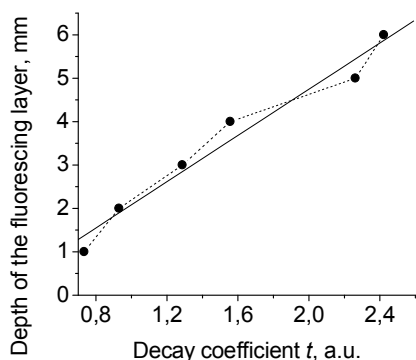


Fig. 10. Reference curve. The decay coefficient t calculated for all depths of the fluorescing layer. The line corresponds to the linear fit.

Decay coefficient t plotted over depth of the fluorescing layer gives the reference curve (Fig.10). The coefficient t is specific for each depth therefore t is the parameter of the depth of the fluorophore. Having the measured intensity distributions of the fluorescing

layer, which is in the unknown depth, it is possible to calculate the decay coefficient and from the reference curve evaluate the approximate depth of the fluorescing layer. Although the measurements were performed in the modeled medium but they are very promising for the evaluation of the fluorophore depth in the weakly scattering tissues.

4. Conclusions

The experimental investigation of the spatially resolved fluorescence from the modeled turbid medium showed, that it is possible to register fluorescence spectra, where the most part of it would be from the deeper layers. This could be achieved when the registration fiber is placed more than 4 mm away from the excitation fiber.

In addition, the change of the thickness of the fluorescing layers significantly changed the fluorescence intensities registered with the 1st and 8th fibers. These findings allow to monitor the change of the fluorescing layers thickness.

Investigations of the fluorescence distributions of the fluorescing layer embedded in various depths of turbid medium showed that it is possible to obtain a reference curve from which the approximate depth of the fluorescing layer, which is in the unknown depth, could be estimated.

5. References

1. G.A. Wagnieres, W.M. Star, B.C. Wilson. *In vivo* fluorescence spectroscopy and imaging for oncological applications. *J. Photochem. Photobiol.* 1998, 68, p. 630-632.
2. Lakowicz J.R. Principles of fluorescence spectroscopy. New York, 1998
3. R. Drezek, C. Brookner, I. Pavlova, I. Boiko, A. Malpica, R. Lotan, M. Follen, and R. Richards-Kortum, "Autofluorescence microscopy of fresh cervical-tissue sections reveals alterations in tissue biochemistry with dysplasia," *Photochem. Photobiol.* **73**, 636–641 ~2001!
4. Zhu Ch., Liu Q., Ramanujam N. Effect of fiber optic probe geometry on depth-resolved fluorescence measurements from epithelial tissues: a Monte Carlo simulation. *J. of Biomed. Opt.* 2003, 8(2), p. 237-247.
5. J. Venius, R. Rotomskis. Analysis of different fluorescence excitation-emission systems for optical biopsy. Proceedings of the 4th international conference on medical physics. Kaunas, 2006. p.5-7.

COMPARISON OF PHOTOGEM[®] AND ALPcS₄ ACCUMULATION IN HEALTHY RAT BRAIN

Vytautas KULVIETIS*, Eugenijus ZAKAREVIČIUS*, Ričardas ROTOMSKIS***, Juozas LAPIENIS*, Gražina GRAŽELIENĖ*

*Laboratory of Biomedical Physics, Institute of Oncology, Vilnius University, LT-01204 Vilnius, Lithuania;

**Laser Research Center, Vilnius University, Saulėtekio 9, LT-10222 Vilnius, Lithuania

Abstract

The efficiency of brain tumour boundary delineation using fluorescence diagnostics is primarily determined by the sufficient accumulation of the sensitizer in the brain tissue. Therefore, we investigated the accumulation of two sensitizers in healthy rat brain using fluorescence spectroscopy. Our results show that Photogem[®] poorly accumulates in rat brain, and its fluorescence overlaps with the endogenous porphyrins. ALPcS₄ definitely occur in brain structures and it would be more suitable sensitizer for brain tumour diagnostics.

Key words: brain tumour diagnostics, sensitizer, Photogem, ALPcS₄, fluorescence spectroscopy.

1. Introduction

The most cases of brain tumours are treated surgically. Unfortunately, the neoplastic tissue is infiltrated into surrounding healthy tissue and it has no distinct boundary. Therefore, it is difficult or even impossible to resect the tumour completely. Unresected neoplastic cells can regenerate and form a new tumour. On the other hand, it is important to minimize the injuries on healthy tissue and the harmful affect to the central nervous system. All in all, accurate tumour boundary delineation determines the success of the surgery. The conventional tumour imaging techniques – computer tomography, magnetic resonance imaging, ultrasonography and visual inspection by neurosurgeon – are not enough effective [1].

One of the new promising harmless methods in brain tumour margins detection is fluorescence diagnostics. During its procedure, a fluorescent marker – sensitizer – is administered to the organism. The sensitizer has an ability to accumulate selectively in neoplastic tissue and it can be detected using fluorescence microscopy or spectroscopy. In this way, target tissue can be distinguished from the healthy surrounding tissue.

Usually two main problems occur when fluorescence diagnostics is applied for brain tumours: low selectivity of the sensitizers for the neoplastic tissue and delivery impediment related to the blood-brain barrier. More to add, there is a wide variety of potential sensitizers, but there are not enough pre-clinical studies indicating which contrasting agent is the most suitable for brain tumour delineation.

Sensitizers used in our study – Photogem[®] and ALPcS₄ – localize primarily where the collagenous proteins are normally found, i.e. basal lamina, connective tissue, keratinized epithelium, mononuclear phagocyte system and cell membranes [2]. Photogem[®] is not a pure compound but a mixture of a purified fraction of hematoporphyrin derivate, oligomeric and monomeric porphyrins. These molecules are more hydrophobic than ALPcS₄ and therefore, Photogem[®] penetrates through cell membrane better and accumulates in intracellular structures at higher concentration. Meanwhile ALPcS₄ is linked to localize in blood vessels and extra cellular matrix [3]. These sensitizers have different pharmacokinetical properties: ALPcS₄ reaches its maximum concentration in the tissues 4 h after intravenous administration and Photogem[®] – 24 h [2,3]. ALPcS₄ has shorter clearance from the organism period than Photogem[®]. Therefore, the organism remains photosensitive for a shorter time after the ALPcS₄ sensitized diagnostic procedure [3].

In order to investigate the accumulation of sensitizers in brain tissue, experiments are usually done on animals with inoculated brain tumours. It is shown that tumour blood vessels have intact blood-brain barrier and increased permeability compared with healthy tissue. Therefore, hematoporphyrin type sensitizers as well as ALPcS₄ can pass from the tumour into the surrounding healthy tissue. This leakage depends on physiological state of the organism and on the histological structure of the tumour [1,2,4]. In this way, experiments with the brain tumour bearing animals do not reflect the accumulation of sensitizers in healthy brain tissue impartially. More to add, experiments are done with a wide diversity of tumours. Therefore, it is

difficult to summarize the forthcoming results of different laboratories. There is a need for more objective studies, which would describe and compare the accumulation of different sensitizers and evaluate their potential effectiveness in brain tumour fluorescence diagnostics.

The aim of our study was to investigate the accumulation of AlPcS₄ and Photogem[®] in healthy brain tissue. To realize this, few tasks were set: to evaluate fluorescence intensity of each sensitizer, to evaluate the autofluorescence of healthy brain structures and to compare potential effectiveness of Photogem[®] and AlPcS₄ in the brain tumour fluorescence diagnostics.

2. Materials and methods

For the experiments two sensitizers were used: Photogem[®] (from “Биолек”, Russia) and aluminum phthalocyanine tetrasulfonate - AlPcS₄ (from “Frontier Scientific”, USA). In order to get the most intense fluorescence signal we irradiated the samples with the light, which is best absorbed by each sensitizer. Photogem[®] has an absorption maximum at 405 nm and AlPcS₄ – at 351 nm [3]. The sensitizers were identified in the specimens according to the shape of their fluorescence spectra (Fig 1.). Fluorescence intensity was evaluated at the main fluorescence peak: Photogem[®] – 628 nm and AlPcS₄ – 684 nm.

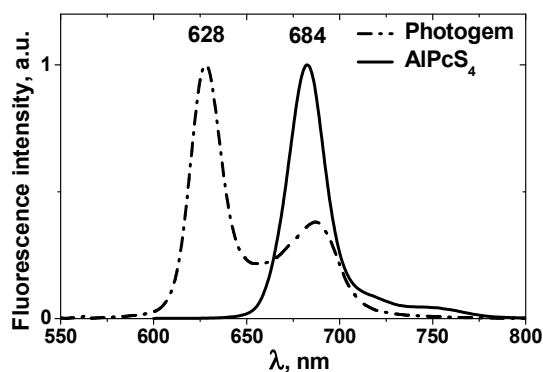


Fig. 1. The fluorescence spectra of Photogem[®] ($\lambda_{ex}=405\text{nm}$) and AlPcS₄ ($\lambda_{ex}=405\text{nm}$) at 10^{-5} M concentration in aqueous solution

During the experiments 14 Wistar albino rats were used (weight 200-350g). 8 animals received slow intravenous injection of the sensitizer at 5 mg/kg or 10 mg/kg dose in 0,5 ml saline and 6 animals were used for control groups. The details of the experimental design are represented in Table 1.

Table 1. Overview of the experimental design

Group	Number of animals	Excitation wavelength, nm
5 mg/kg AlPcS ₄	3	351
Control	3	351
5 mg/kg Photogem [®]	3	405
10 mg/kg Photogem [®]	2	405
Control	3	405

The incubation period was chosen according to the pharmacokinetics of the sensitizer: 4 hours for AlPcS₄ and 24 hours for Photogem[®] [2,3]. Rats were kept in the dark until they were sacrificed by lethal ketamine dose (0,5 ml). The organs were removed and prepared for spectroscopic investigation.

Parenchymous organs (liver, spleen, lungs, muscle, kidneys, Harderian gland) were prepared for fluorescence spectroscopy by making their cross-sections (thickness ~1mm). Tubular organs (oesophagus, stomach, duodenum, small intestine, bladder, uterus) were prepared by cutting their walls. The brain grey matter was separated from the surface of the brain. The white matter was collected from deeper layers of the brain. Cerebellum specimen represented the whole brain tissue and it was prepared by making cross-section. In total, 16 samples from each animal were prepared for spectroscopic analysis.

The animal husbandary and experiments on animals were carried out according to the national and European regulations and were approved by Lithuanian Animal Care and Use Committee.

Fluorescence spectra were registered using luminescence spectrophotometer Perkin Elmer LS50B. Excitation wavelength for specimens sensitized with Photogem[®] was 405 nm and for AlPcS₄ - 351 nm. Fluorescence emission spectra were measured in the range of 550-800 nm. Fluorescence spectra were measured for each sample at three different positions and they were averaged. On purpose to eliminate the autofluorescence of the tissue and to evaluate the fluorescence of the sensitizer, all spectra were normalized at 600 nm. This wavelength was chosen according to two factors. Firstly, tissue fluorescence of shorter wavelength is reabsorbed by blood (main absorption peak of oxyhemoglobin is at 580 nm). Secondly, fluorescence of sensitizers was observed at longer wavelengths (Fig. 1).

On purpose to evaluate the accumulation of the sensitizers in each tissue, the normalized autofluorescence spectra of the control samples were subtracted from the normalized fluorescence spectra of the samples incubated with the sensitizer. The fluorescence intensity differences for each sample were averaged and the standard error was evaluated. The accumulation of sensitizers was evaluated by the difference at the main sensitizer’s peak: for Photogem[®] at 628 nm and for AlPcS₄ at 684 nm.

For the additional comparison of the fluorescence intensities of control and sensitized samples Mann-Whitney test was used. P values smaller than 0,05 were considered statistically significant.

The distribution of endogenous porphyrins in rat organism was evaluated considering to the autofluorescence spectra of the control group with 405 nm excitation wavelength. Porphyrins were identified according to the shape of the fluorescence spectra and the position of the main peak

3. Results

In the samples sensitized with AlPcS₄ the fluorescence peak was observed at 684 nm and in the most cases of Photogem[®] sensitized samples - at 628 nm (Fig. 2).

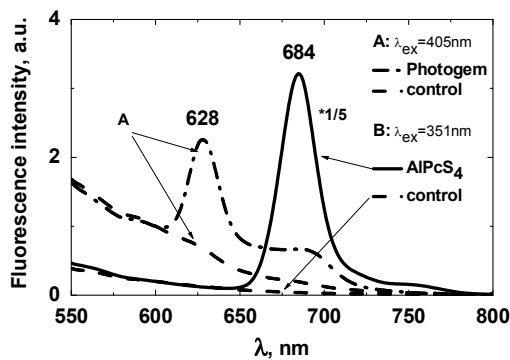


Fig. 2. Fluorescence spectra of rat uterus after i.v. administration of sensitizers at 5 mg/kg. AlPcS₄ and its control fluorescence spectra intensities are reduced in 5 times

The fluorescence of AlPcS₄ was easily detected in all specimens of sensitized tissues. The highest concentrations were observed in bladder and uterus. The least concentrations were registered in the brain structures: cerebellum, white matter and grey matter (Fig. 3).

The average AlPcS₄ concentration ratio in the brain to other tissue varied from 1:2,5 for the spleen to 1:13,7 for the bladder. Moderately, AlPcS₄ accumulates in the brain structures at 7 times lower concentration than in other organs. The low level of the sensitizer in the brain could be determined by limited sensitizer's permeability through the blood-brain barrier.

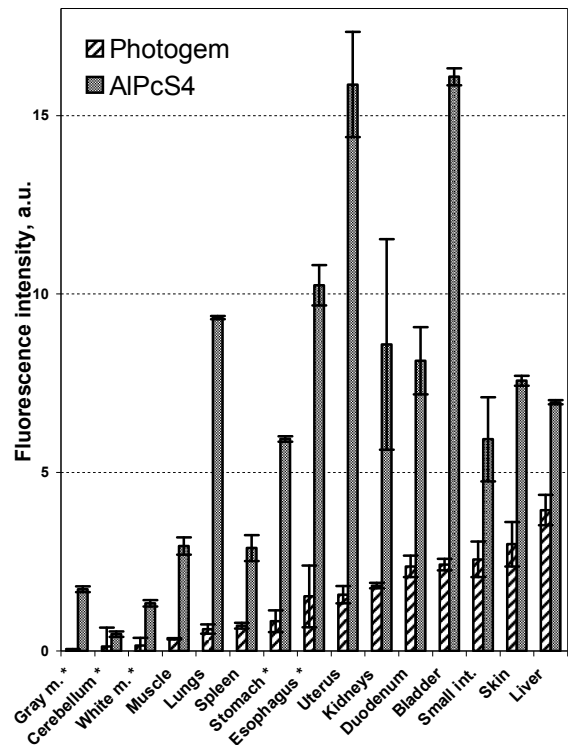


Fig. 3. Distribution of Photogem[®] ($\lambda_{ex}=405\text{nm}$, $\lambda_{fl}=628\text{nm}$) and AlPcS₄ ($\lambda_{ex}=351\text{nm}$, $\lambda_{fl}=684\text{nm}$) in rat brain structures and other organs. Sensitizers' dose 5 mg/kg, incubation time: 24h for Photogem[®] and 4h for AlPcS₄. Intervals indicate standard errors. * $p>0,05$ for Photogem[®]

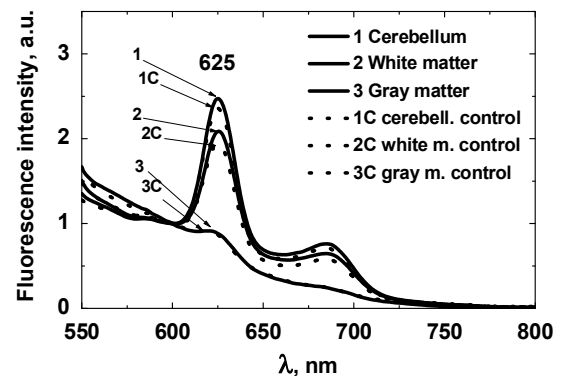


Fig. 4. The fluorescence spectra of the brain structures after Photogem[®] administration (solid lines) and control samples (dotted lines), ($\lambda_{ex}=405\text{nm}$)

When Photogem[®] was administered to the experimental animals, the characteristic fluorescence peak for this photodrug (at 628 nm) was not detected in the brain samples. The fluorescence spectra of brain structures after sensitizer injection did not differ from the control group (Fig. 4). Mann – Whitney test showed that p values for the brain structures were greater than

0,05 (grey matter - 0,83, white matter - 0,51 and cerebellum - 0,57).

The fluorescence peak in control group as well as in Photogem[®] group was observed at 625 nm ($\lambda_{ex}=405$ nm). There was seen another smaller peak at 685 nm. These fluorescence peaks were assigned to endogenous coproporphyrin [4]. They were not expressed in the brain grey matter or any other sample.

There were seen no changes in brain fluorescence spectra when the Photogem[®] even when the sensitizer's dose was increased by 2 times (10 mg/kg). Meanwhile the fluorescence intensity at the main peak in other organs slightly increased.

These results indicate that Photogem[®] passage through the blood-brain barrier is limited.

When 405 nm excitation light was applied, in some control samples fluorescence peaks at 620 nm (kidneys) and 635 nm (Harderian gland, skin, liver, oesophagus, stomach, duodenum) were observed. These peaks were assigned to uroporphyrin and protoporphyrin IX, respectively [4,5].

In some of these samples the main fluorescence peak after Photogem[®] administration was red shifted: from 628 nm to 630-633 nm, because of the overlapping fluorescence of Photogem[®] and endogenous porphyrins. After subtracting from these spectra the appropriate control autofluorescence spectra, the fluorescence peak of Photogem[®] at 628 could be identified and the accumulation of the sensitizer could be evaluated. The highest concentrations of accumulated Photogem[®] were observed in liver and skin (Fig. 3).

The fluorescence of endogenous porphyrins wasn't expressed analyzing the accumulation of AlPcS₄. Since absorption maximum of the endogenous porphyrins is in the region of 390-410 nm, only the fluorescence peak of AlPcS₄ was identified, when 351 nm excitation light was applied. Therefore, it was easier to analyze the fluorescence spectra of the tissues sensitized with AlPcS₄ and to evaluate the accumulation of this sensitizer more precisely. More to add, AlPcS₄ fluorescence was approximately 5 times more intense than that one of Photogem[®].

4. Discussion

Our results indicate that Photogem[®] was not detected in the healthy rat brain structures by means of fluorescence spectroscopy, while it was identified in all other specimens. There are some studies showing that hematoporphyrin type sensitizers occur in healthy brain tissue when administered intravenously into brain tumour bearing animals [2]. It is also proved that sensitizers can pass through the intact blood-brain barrier of the tumour and accumulate in the surrounding healthy tissue [1,4]. The bulk of this flow depends on the histological structure of the tumour and on the physiological state of the organism. In this way experiments performed on animals with inoculated brain

tumours do not reflect the accumulation of exogenous sensitizers in healthy brain objectively. However, our results and those found in the literature show that blood-brain barrier has low permeability for hematoporphyrin type sensitizers, including Photogem[®].

The AlPcS₄ occurred in all the investigated organs. The least concentrations were registered in the brain structures: it was moderately 7 times lower than in other organs. This result is in agreement with the other authors, who detected AlPcS₄ in the brain at 8-50 times lower concentration than in other tissues [2].

During our study it was found out that endogenous porphyrins accumulate in some rat tissues. They were identified considering to the main autofluorescence peak position ($\lambda_{ex}=405$ nm): protoporphyrin IX (fluorescence peak at 635 nm), uroporphyrin (620 nm) and coproporphyrin (625 nm) [4,5]. The highest concentration of protoporphyrin IX was observed in Harderian gland. It also appeared in digestive tract, skin and liver. Protoporphyrin IX is thought to pass from the Harderian gland with tears through nasal duct into nasal cavity, pharynx and further on to the digestive tract. The level of endogenous porphyrins may increase because of various disturbances of heme biosynthesis. The activity of heme biosynthesis enzymes change in the case of inherited diseases (called porphyrias), inflammatory processes, pathological conditions or other physiological stresses [5].

The accumulation of endogenous porphyrins in the brain white matter was also observed by other authors. It was reported that porphyrins in the grey matter occur at lower quantities than in myelinated tissue structures. It is explained that heme biosynthesis in oligodendrocytes and Schwann cells, which form the white myelin sheaths, is more intense than in the neurons [1].

Whereas the fluorescence spectra of endogenous porphyrins and Photogem[®] overlap, the application of this sensitizer in brain tumour fluorescence diagnostics would be complicated: it would be difficult to distinguish fluorescence of accumulated Photogem[®] in neoplastic tissue from the surrounding healthy areas with very similar optical properties. On the other hand, a part of excitation light for Photogem[®] (405 nm) would be absorbed by endogenous porphyrins. Therefore, less sensitizer's molecules would be excited and lower fluorescence could be detected. These disadvantages are not characteristic for AlPcS₄. The excitation light, which would be used in AlPcS₄ sustained diagnostics, wouldn't be absorbed by endogenous porphyrins and more intense fluorescence signal could be detected. More to add, AlPcS₄ fluorescence spectrum doesn't overlap with spectra of endogenous porphyrins. This sensitizer fluoresce in the far red region (684 nm) and therefore this light is less reabsorbed by the tissue than that one of Photogem[®]. These facts indicate that using AlPcS₄ in fluorescence diagnostics more intense fluorescence signal and higher accuracy could be

achieved compared to Photogem[®]. Consequently, ALPcS₄ would be more effective marker in brain tumours fluorescence diagnostics.

5. Conclusions

Photogem[®] does not accumulate in the healthy rat brain at the concentration which could be detected using fluorescence spectroscopy. Meanwhile fluorescence of ALPcS₄ is observed in all brain structures. The fluorescence of Photogem[®] during intra-operative tumour delineation could be misled with fluorescence of endogenous porphyrins which occur naturally in the healthy brain tissue. The fluorescence of ALPcS₄ is more intense and it doesn't overlap with fluorescence of endogenous porphyrins. Therefore, ALPcS₄ would be more suitable sensitizer for brain tumours fluorescence diagnostics.

6. References

1. Chung YG, Schwartz JA, Gardner CM, Sawaya RE, Jacques SL. Diagnostic Potential of Laser-Induced Autofluorescence emission in Brain Tissue. *J Korean Med Sci*, 1996. 12(2): 135-42.
2. Dereski MO, Madigan L, Chopp M. Brain response to photodynamic therapy and Photofrin, nonsulfonated aluminum phthalocyanine and tin purpurin. *Proc. SPIE*, 1995. 2371: 579-81.
3. Chan WS, Marshall JF, Svensen R, Bedwell J, Hart IR. Effect of Sulfonation on the Cell and Tissue Distribution of the Photosensitizer Aluminum Phthalocyanine. *Cancer Research*, 1990. 50:4533-8.
4. Hebeda KM, Saarnak AE, Olivo M, Sterenborg HJCM, Wolbers JG. 5-Aminolevulinic Acid Induced Endogenous Porphyrin Fluorescence in 9L and C6 Brain Tumours and in the Normal Rat Brain. *Acta Neurochirurgica*, 1998. 140:503-13.
5. Lin DL, He LF, Li YQ. Rapid and Simultaneous Determination of Coproporphyrin and Protoporphyrin in Feces by Derivative Matrix Isopotential Synchronous Fluorescence Spectrometry. *Clinical Chemistry*, 2004. 50(10): 1797-803.

IMRT DOSE VERIFICATION

Helen Gustavsson, Anna Karlsson, Sofie Månsson, Fredrik Nordström, Lena Wittgren and Sven ÅJ Bäck
Department of Medical Radiation Physics, Malmö University Hospital, Sweden

Abstract

In order to verify an individual intensity-modulated radiation therapy (IMRT) plan, one- and two-dimensional measurements are normally performed. The aim of this study was to investigate different types of detectors (1-, 2- and 3D), as well as an independent dose calculation, for verification. The used detector systems were an ion chamber (1D), a diode array (2D) and a polymer gel (3D). An in-house developed dose calculation algorithm was used for the independent dose check. A treatment plan for a head&neck case was transferred to the different phantoms and the dose was calculated using the Oncentra Optimiser in MasterPlan 1.5 (Nucletron, The Netherlands). The measurements were compared with calculated values of point dose (1D), isodoses and gamma (2D) and dose volume histograms (DVH) (3D), respectively. Good agreement between calculated and measured data was obtained for all three systems. The point dose measurement, using the ion chamber, was 1.8% lower than the calculated value, with maximum and minimum deviations of 9 and -14% for individual beams, respectively. Comparing the diode array measurement and calculations, a minimum of 88.2% of the points passed the 3mm/3% gamma criteria. The corresponding number for the independent dose calculation was 82%. Deviations were observed in the penumbra as well as in low dose regions, where the TPS calculations are known to be erroneous. The same deviations were observed in the gamma maps and DVHs obtained from the gel measurement.

Keywords: IMRT, verification, gel dosimetry, ion chamber, diode array, independent dose calculation.

1. Introduction

Intensity-modulated radiation therapy (IMRT) was introduced in the mid-nineties, and has now been widely implemented. In order to verify an individual intensity-modulated radiation therapy (IMRT) plan, one- and two-dimensional measurements are normally performed. For the one-dimensional measurement, ion chambers are commonly used (1), while film, EPID (Electronic portal imaging device) diode or ion chamber arrays are used for the 2D measurement (e.g. 2, 3). However, it is still debated whether these types of verification measurements are enough to guarantee a correct delivery. The verification of IMRT is complicated by the fact that the radiation field is continuously changing size and shape (sliding window) or made up by multiple small beam segments (step and shoot). The ion chamber measurement is performed in a single point, and many of the segments will not be directly incident on the chamber. As a consequence a large contribution to the measured dose will come from scattered radiation, which is a source of error (4). For the 2D measurement, all beams are usually delivered orthogonal to the detector, i.e. the gantry angle is 0° for all beams. Consequently, the MLC movement will not be verified with the gantry in the correct position. Furthermore, the diode and ion chamber arrays have a limited resolution, between 0.5 and 1 cm for the commercially available systems. Since an IMRT dose distribution often contains sharp dose gradients, good spatial resolution is desirable. Ideally, a detector with the possibility for integrating volumetric measurements with high resolution should be used. Another crucial feature is

that the detector response should be independent of incident radiation direction. This would enable a complete treatment to be evaluated in a single measurement, as opposed to measuring each beam separately. Gel dosimetry have been used in several studies for verification of IMRT (e.g. 5, 6). In most studies the gel measurement was only compared to TPS calculations. The aim of this study was to investigate different types of detectors (1, 2 and 3D) for IMRT verification. In addition to the 1- (ion chamber) and 2D (diode array) verification that are routinely used in our clinic a 3D (gel dosimetry) measurement was performed. Furthermore, an independent dose calculation was performed, using a method for monitor unit verification that is used routinely in our clinic (7). The observed deviations between the measurements and the TPS calculations were analyzed and compared for the different systems.

2. Materials and methods*2.1. Treatment planning*

Inverse treatment planning was performed using the Oncentra Optimiser in the MasterPlan 1.5 treatment planning system (TPS, Nucletron, The Netherlands). The selected plan was a treatment for a larynx cancer, which consisted of seven coplanar beams. Two PTVs were defined and planned to receive 67.2 Gy and 54.4 Gy at the normalization point, respectively. The plan data was transferred to

CT scans of the different phantoms used for the 1D, 2D and 3D measurements, respectively, and the absorbed dose was calculated for all cases. Irradiation was performed using an Electa linear accelerator (Electa, Sweden) and 6 MV photons. The accelerator is equipped with an 80 leaf dynamic MLC, and intensity modulation is achieved using step and shoot.

2.2. Ion chamber measurement

For the ion chamber measurement an elliptical CT phantom with drilled cavities for the ion chamber was used. The ion chamber was a Farmer NE 2571 0.6 cc (Nuclear Enterprises, U.K.). A reference measurement was performed using a 10x10 cm² beam, with the ion chamber positioned at the isocenter. The phantom was then moved so that the ion chamber was positioned in a region with homogenous dose according to the TPS calculations. The treatment delivery was performed in the same way as for the patient, i.e. using the correct gantry and collimator settings.

2.3. Diode array measurement

A Mapcheck diode array (Sun Nuclear Corporation, Melbourne, FL) was used for 2D measurements of the absorbed dose distribution. The array contains 445 diodes, with a detector spacing of 0.7 cm in the inner 10x10 cm² detector array, and a spacing of 1.4 cm in the outer array. The total measurement area is 22x22 cm². The measurement was performed at source-to-detector distance of 100 cm, with 5 cm buildup. Each beam was delivered separately, all using a gantry angle of 0 degrees. The measured data was compared with the TPS calculations using gamma evaluation with the criteria 3mm/3% and a minimum relative dose cut-off threshold of 10% (figure 1).

2.4. Gel dosimetry measurement

The gel was prepared according to the procedure described in previous publications (8, table 1), and following the good practice recommendations suggested by Karlsson (9). A 2 liter cylindrical glass phantom was used for the verification of the treatment plan, while eight 15 ml glass vials were used for investigation of the absorbed dose response of the gel. The gels were irradiated the day after preparation. Irradiation of the IMRT phantom was performed according to the treatment plan. The vials used for dose response evaluation were placed at maximum dose depth in a water bath, and irradiated to absorbed doses between 0.5 and 8 Gy. After irradiation the gels were placed in the MRI room in order to establish thermal equilibrium before scanning.

Table 1. Gel composition, concentrations are in percentage weight by weight (% w/w).

Chemical	Concentration
Purified water	90%
Gelatin	8%
MAA	2%
THP	2 mM

MR imaging was performed approximately 24 h after irradiation using a 3 T Siemens Trio scanner (Siemens, Erlangen, Germany), and a 32-echo multiple spin echo pulse sequence (Table 2). The IMRT phantom was placed in the center of a receiver head coil. The body coil was used for transmission of the RF pulse. The dose response vials and depth dose tubes were imaged together, also positioned in the center of the coil. In order for direct comparison between gel measured and TPS calculated data to be feasible, 3 mm thick slices were acquired at the same positions as the CT-slices. Forty-eight slices were needed to cover the PTV. To avoid cross-talk the slices were separated by a 18 mm distance, i.e. adjacent slices were not scanned at the same run of the sequence. Therefore, the sequence was repeated six times, with eight slices acquired from each measurement. The total acquisition time was approximately 3 hours.

The T2 value of each pixel was derived by fitting a monoexponential decay to the MR signal values using the Levenberg-Marquardt optimisation algorithm. The calculations were performed using an in-house developed software routine written in IDL (Interactive Data Language, Research Systems Inc., Boulder, CO, USA) (9). Background subtraction of the R2 images as well as matching and normalization of calculated and gel measured images were performed using the same software. The TPS and MR images were matched using fiducial markers (lead spheres for the CT images and vitamin E capsules for the MR images) as reference. Normalization of the measured and calculated dose distributions was performed in the isocenter point.

Table 2. MR scanning parameters.

MR parameter	Value
TR (ms)	4700
TE (ms)	10.6
No of echoes	32
FoV (mm ²)	256x224
Matrix size	256x224
Slice thickness (mm)	3
No of acquisitions	2
Scanning time (min)	30

2.5. Independent dose calculation

Independent dose calculations were performed for each beam separately. The dose was calculated in the

same geometry as for the diode array, at 5 cm depth and a source-to-detector distance of 95 cm. A gamma comparison was performed with the same criterion as for the diode array measurement.

3. Results and discussion

3.1. Ion chamber measurement

The deviation between the summed beam ion chamber reading and the TPS calculation was -1.8%. However, the variation in the corresponding figure for the individual beams was considerably larger, between -14 and +9% (table 3). This is supposedly due to the varying angles and beam segment sizes, which leads to over- and underestimation of the dose under measurement conditions far from radiation equilibrium (4).

Table 3. Results from the in chamber measurement.

Beam no	Ion chamber (Gy)	TPS (Gy)	Deviation (IC/TPS) (%)
1	0.102	0.095	7.89
2	0.291	0.287	1.27
3	0.402	0.424	-5.19
4	0.385	0.399	-3.56
5	0.240	0.28	-14.25
6	0.316	0.31	2.08
7	0.266	0.245	8.67
Summary	2.003	2.040	-1.83

3.2. Diode array measurement

For the beam with the largest number of failed points, 88.2% of the points passed the gamma criterion (table 4). Relative deviations of up to almost 20% were found, primarily in the penumbra or low dose regions. The points around the penumbra that failed the test were always located in the proximity of sharp gradients. It is well known that the TPS overestimates the absorbed dose in the penumbra region (e.g.10).

Table 4. Pass ratios (PR, Number of points that pass the criteria divided by the total number of points) for the gamma evaluation for the diode array and independent dose calculation.

Beam no	Diode array Passratio (%)	Independent dose calculation PR (%)
1	89.0	82
2	91.2	85
3	95.1	84
4	92.0	85
5	88.2	87
6	91.5	86
7	94.8	86

In the low dose region, corresponding to the medulla in the investigated treatment plan, the absorbed dose is underestimated by the treatment planning system. This is

also a well know phenomena, caused by insufficient modeling of the inter-leaf transmission (e.g. 11).

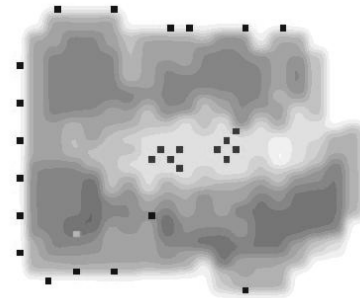


Figure 1. Gamma calculation comparing the diode array measurement with the TPS calculations for one of the seven beams. Red dots are deviations where the measured dose was larger than the calculated, while blue indicates a lower measured value. The green dot indicates the maximum dose value.

3.3. Gel dosimetry measurement

An approximately linear dose response evaluated by means of transversal relaxation rate (R2) was found for the absorbed doses in the investigated interval (figure 2). The slope and intercept for the R2 versus dose curve were $0.58 \text{ s}^{-1}\text{Gy}^{-1}$ and 2.42 s^{-1} ($r^2=0.999$). The assumption of a linear dose response was thus justified and a relative dose evaluation was undertaken. The relative dose was compared to the dose calculations from the treatment planning system (figure 3) using gamma evaluation, isodose comparison and DVHs.

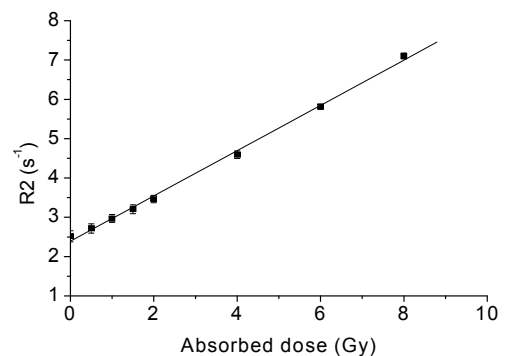


Figure 2. Dose response evaluated by means of relaxation rate (R2) as a function of absorbed dose. The uncertainty bars correspond to one standard deviation in the R2 map.

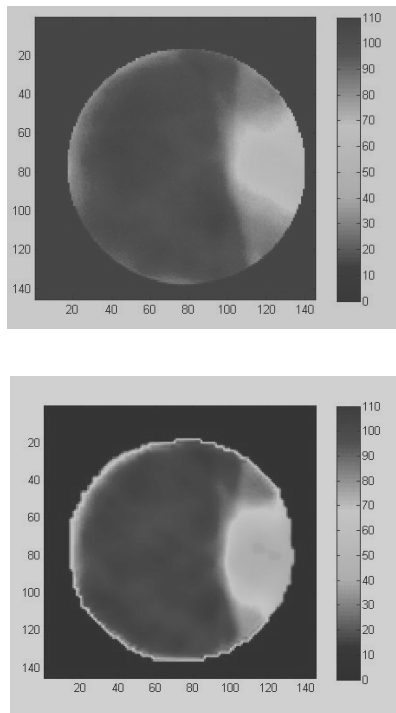


Figure 3. Relative dose maps in the isocenter slice. Polymer gel measurement (top) and dose calculation (bottom).

3.3. Independent dose calculation

The pass ratios for the gamma evaluation of the independent dose calculation varied between 82 and 87% (table 4). That is, fewer point passed the evaluation than corresponding data from the diode array measurement. Except for the regions that showed large disagreements in the diode array measurement, the majority of the deviations were scattered throughout the beams (figure 3).

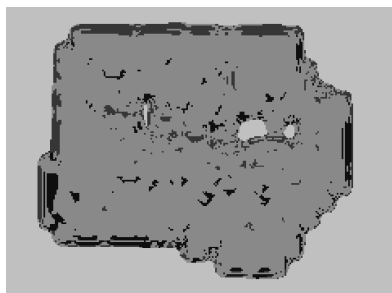


Figure 3. Gamma calculation comparing the independent dose calculation with the TPS calculations for one of the seven beams. Red dots are deviations where the dose from the independent calculation was larger than the TPS calculated, while blue indicates a lower value.

4. Conclusions

The 1D measurement using the ion chamber agreed well with the TPS calculated data when the beams were summed. However, large differences were observed for the individual beams. This indicates that this method

might not be suitable for measurements of absolute dose for IMRT plans.

For the 2D comparisons using the gamma method, the independent dose calculation, diode array- and gel dosimetry measurements all showed deviations in the penumbra and low dose region. The discrepancies can to a large extent be attributed to errors in the TPS calculations. In our clinic, the accepted maximum dose to the medulla is therefore approximately 20% lower than for a conventional plan.

5. References

1. Bouchard, H. & Seuntjens, J. Ionization chamber-based reference dosimetry of intensity modulated radiation beams. *Med Phys* **31**, 2454-2465 (2004).
2. Sankar, A. et al. Comparison of Kodak EDR2 and Gafchromic EBT film for intensity-modulated radiation therapy dose distribution verification. *Med Dosim* **31**, 273-282 (2006).
3. Cilla, S. et al. Comparison of measured and computed portal dose for IMRT treatment. *J Appl Clin Med Phys* **7**, 65-79 (2006).
4. González-Castaño, D. et al. The change of response of ionization chambers in the penumbra and transmission regions: impact for IMRT verification. *Med Biol Eng Comput* (2007).
5. Gustavsson, H. et al. MAGIC-type polymer gel for three-dimensional dosimetry: intensity-modulated radiation therapy verification. *Med Phys* **30**, 1264-1271 (2003).
6. Wu, C.S. & Xu, Y. Three-dimensional dose verification for intensity modulated radiation therapy using optical CT based polymer gel dosimetry. *Med Phys* **33**, 1412-1419 (2006).
7. Knöös, T., Johnsson, S.A., Ceberg, C.P., Tomaszewicz, A. & Nilsson, P. Independent checking of the delivered dose for high-energy X-rays using a hand-held PC. *Radiother Oncol* **58**, 201-208 (2001).
8. Karlsson, A., Gustavsson, H., Månsson, S., McAuley, K.B. & Bäck, S.A. Dose integration characteristics in normoxic polymer gel dosimetry investigated using sequential beam irradiation. *Phys Med Biol* **52**, 4697-4706 (2007).
9. Karlsson, A., PhD Thesis, (Lund University, Malmö, 2007).
10. Ahnesjö, A. & Aspradakis, M.M. Dose calculations for external photon beams in radiotherapy. *Phys Med Biol* **44**, R99-155 (1999).
11. Azcona, J.D., Siochi, R.A. & Azinovic, I. Quality assurance in IMRT: importance of the transmission through the jaws for an accurate calculation of absolute doses and relative distributions. *Med Phys* **29**, 269-274 (2002).

NEW PORTAL DOSIMETRY METHOD FOR THE INTENSITY MODULATED RADIOTHERAPY FIELDS

Sergey Popov¹, Sandija Plaude¹, Albert Miller², Yuri Dekhtyar³

1 – Latvian Oncology Center of Riga Eastern University Hospital, 4, Hipokrata St., Riga, LV-1079, Latvia

2 – Vilnius University Oncology Institute

3 – Riga Technical University

Abstract

Intensity Modulated Radiotherapy (IMRT) was introduced in clinical practice during the last decade. IMRT has potential to improve conformity of dose distributions virtually for all tumor localizations. Improvement of dose distributions conformity in IMRT, which is accompanied by high technical complicity of this method, raises new questions in field of verification of treatment planning and dose delivery. New dosimetry method for Intensity Modulated Radiotherapy fields was developed, allowing to estimate from two-dimensional dose distribution, acquired using Electronic Portal Imaging Device, two-dimensional dose distribution in water equivalent phantom. New method can be used for patient related clinical dosimetry in all hospitals, using dynamic Intensity Modulated Radiotherapy.

Keywords: Intensity Modulated Radiotherapy, Dosimetry, Electronic Portal Imaging device

1. Introduction

Intensity Modulated Radiotherapy (IMRT) was introduced in clinical practice during the last decade. IMRT has potential to improve conformity of dose distributions. IMRT uses all Three-Dimensional Conformal Radiation Therapy (3D-CRT) tumor visualization and dose calculation methods, with addition of inverse treatment planning and delivery of radiation beams with intensity modulated fluence. Using radiation beams with fluence intensity modulation, high dose regions can be shaped to conform target volume, so lowering the dose to surrounding normal tissues. With IMRT is possible to deliver higher doses to tumor, which for these localizations is improving survival and cure rates. Furthermore, using IMRT it is possible to reduce complications for many tumor sites.

One of the most commonly used methods for delivery of IM fields in radiotherapy is delivery using clinical linear accelerator equipped with dynamic Multileaf Collimator (dMLC). In this method, movement of individual MLC leaves while radiation beam is on achieves fluence modulation.

Improvement of dose distributions conformity in IMRT, which is accompanied by high technical complicity of this method, raises new questions in field of verification of treatment planning and dose delivery.

For IMRT procedures precision of dose delivery is recommended to be $\pm 3\%$ for dose error and ± 3 mm for spatial deviation (1 standard deviation, 0.68 confidence interval) [1, 2, 3].

IMRT fields are commonly verified delivering plan to the phantom, and comparing measured resulting dose distributions with ones calculated by TPS.

Most commonly used and most reliable IMRT verification measurements method is based on combination of film and ionometric dosimetry. This method has two drawbacks: film dosimetry is very time consuming and requires highly qualified and experienced personnel; effects of partial irradiation of ion chamber in the presence of high dose gradient can give rise to reading error up to 13%. It is needed to develop and introduce in the clinical practice new method of patient related dosimetry for IMRT plan verification, which results will be equal to the existing film and ionometric dosimetry method.

Virtually all linear accelerators used for IMRT treatments are equipped with Electronic Portal Imaging Devices. Signal of acquired EPID image is proportional to the dose absorbed in EPID cassette material, and it should be possible to develop method that will estimate dose absorbed in water equivalent phantom from EPID signal.

2. Materials and Methods

2.1. Selection of detectors for calibration and test measurements

Reference dose distribution in water equivalent phantom was acquired using film dosimetry. Films were irradiated in water equivalent phantom at the depth of 5 cm, at the isocenter plane. Ionization chamber was positioned in the phantom under the film. Chamber signal was used to perform verification and correction of film dosimetry results.

Films were calibrated using method proposed by Childress et al. [4]. During each measurement series,

calibration film was exposed together with test films with 9 dose levels (1.23 – 95.63 cGy). Areas with different dose levels were formed using dynamic Multileaf Collimator (dMLC) static sequence. Film scanner Vidar 16 VXR (Vidar Systems Corporation, USA) was used for film digitizing, in 12 bit mode, with resolution of 75 dpi (point size 0.339 mm). Scanned films were stored in 12-bit TIFF format, for further processing using DoseLab 4.0 software [5]. Optical density image was converted to the dose image, using calibration curve, acquired by means of calibration film. Quality of the developer, together with used film calibration method is allowing to achieve film dosimetry precision of $\pm 2\%$ [Error! Bookmark not defined.].

2.2. Calibration of Electronic Portal Imaging Device dosimetric image acquisition mode.

Amorphous silicon EPID (PV aS500, Varian Medical Systems, USA) was used in this work. EPID had following physical properties: sensitive area $40 \times 30 \text{ cm}^2$; matrix size $512 \times 384 = 196,608$ pixels; pixel size $0.784 \times 0.784 \text{ mm}^2$; time of one frame acquisition 0.111 sec. EPID image signal is proportional to the dose, absorbed at detector measurement plane. The dosimetric image was acquired in relative Calibration Units (CU). EPID calibration procedure used for imaging (dark field and flood field corrections) is supplemented by radial accelerator fluence distribution correction.

Measurements performed have shown that EPID signal dependence from the irradiated field size is not linear. Therefore dosimetric image calculation method was supplemented by new multiplicative coefficient (K), which takes into account these signal non-linearities. Proposed coefficient (K) was calculated as ratio of water and EPID total output factors:

$$K(A,B) = \frac{OF^{H_2O}(A,B)}{OF^{EPID}(A,B)}, \quad (1)$$

$$OF(A,B) = \frac{D(A,B)}{D(10,10)}, \quad (1.1)$$

where $OF^{H_2O}(A,B)$ – total output factor measured in water (AU); $OF^{EPID}(A,B)$ – total output factor measured from EPID dosimetric images (AU); A and B – size of the field defined by accelerator jaws (cm); D(A,B) – dose measured by given detector for given field size (Gy); D(10,10) – dose for field $10 \times 10 \text{ cm}^2$, reference geometry (Gy).

Maximal value of the correction factor was 1.046 for field size $3 \times 3 \text{ cm}^2$, minimal 0.950 for field size $28 \times 38 \text{ cm}^2$. Maximal absolute value of introduced correction over whole range of the field sizes was 5.2 %.

Than resulting dosimetric image correcting scheme for each pixel can be defined as following:

$$D^{EPID}(x,y) = \left(\frac{[s(x,y) - DF(x,y)] / FF(x,y) k_{FFmean} OAR(x,y)}{C} \right) K(A,B), \quad (2)$$

$$C = \frac{[s(0,0) - DF(0,0)] / FF(0,0) k_{FFmean}}{D = 1 \text{ Gy, field} = 10 \times 10 \text{ cm}^2, SDD = 100 \text{ cm}} \quad (2.1)$$

$$k_{FFmean} = \frac{\sum_{x=0}^{N-1} \sum_{y=0}^{M-1} FF(x,y)}{NM}, \quad (2.2)$$

where $D^{EPID}(x,y)$ - EPID dosimetric image value for pixel with coordinates x and y respectively; s(x,y) – uncorrected value of each pixel; DF(x,y) – dark current value for each pixel; FF(x,y) – individual pixel gain coefficient; k_{FFmean} – gain coefficient averaged over all sensitive area; OAR(x,y) – off axis ratio, normalized to beam central axis; C - acquisition matrix calibration coefficient, acquired in standard calibration conditions; SSD – Source Surface Distance (cm); N – number of elements of two-dimensional dose distribution in row; M – number of elements of two-dimensional dose distribution in column; K(A,B) – coefficient taking into account matrix response non-linearity with field size, for field size A and B (equation (1.)).

2.3. Method for calculation of two-dimensional dose distribution in water equivalent phantom from Electronic Portal Imaging Device dosimetric image.

In homogeneous media dose from photon radiation, in a point where electron equilibrium exists can be calculated as follows [6]:

$$D = \frac{\bar{\mu}_{en}}{\rho} \Psi_{prim} e^{-\bar{\mu}d} + S, \quad (3)$$

where D – absorbed dose (Gy); $\frac{\bar{\mu}_{en}}{\rho}$ - effective mass energy absorption coefficient ($\frac{m^2}{kg}$); $\bar{\mu}$ - effective linear attenuation coefficient (1/m); ρ - density of media (kg/m^3); Ψ - primary photon energy fluence ($\frac{MeV}{m^2}$); S – scatter component (Gy); d – depth of the calculation point in a media (m).

Scatter component (S) of the dose was described as [7]:

$$S(x,y,z) = \sum_{x'} \sum_{y'} \sum_{z'} \frac{\bar{\mu}}{\rho}(x',y',z') \Psi_{prim}(x',y',z') [A_{sc}(x-x',y-y',z-z') \Delta x \Delta y \Delta z] \quad (4)$$

$$\Psi_{prim}(x',y',z') = \Psi_{prim} e^{-\mu d(x',y',z')}, \quad (4.1)$$

where A_{sc} – scattered radiation energy absorption and transfer function [$1/m^3$]; $\Psi_{prim}(x',y',z')$ - primary photon energy fluence at the point of the scatter source ($\frac{MeV}{m^2}$).

For homogeneous media equations (3) and (4) were combined without loss of generality, to calculate together contribution of primary and secondary component of the dose, using single energy absorption and scattering function, A_{pri+sc} [$1/m^3$]:

$$D(x,y,z) = \iiint_{x',y',z'} \bar{\mu}(x',y',z') \Psi_{prim}(x',y',z') A_{pri+sc}(x-x',y-y',z-z') dx'dy'dz', \quad (5)$$

In the case of EPID, one need to calculate dose in single plane and therefore equation (5) can be truncated as:

$$D(x,y) = \iint_{x',y'} \bar{\mu}(x',y') \Psi_{prim}(x',y') A_{pri+sc}(x-x',y-y') dx'dy', \quad (6)$$

From signal processing theory point of view, assuming that primary photon fluence is signal function and A_{pri+sc} is system response function, equation (6) can be rewritten as signal function Ψ_{prim} convolution with response kernel A_{pri+sc} :

$$D = \Psi_{prim} \otimes A_{pri+sc}. \quad (7)$$

Any signal, which was affected by response function, can be restored in original form using deconvolution.

One-dimensional convolution for discrete function of finite duration M is linear equation system solving from unknown primary signal Ψ_{prim} [8]:

$$(\Psi_{prim} * A_{pri+sc})_j \equiv \sum_{k=-M/2+1}^{M/2} (\Psi_{prim})_{j-k} * (A_{pri+sc})_k. \quad (8)$$

Such a system solution in time domain is not realistic, especially in case of two-dimensional deconvolution.

Using Fourier transform for signal and response discrete functions one-dimensional convolution in frequency domain can be described as multiplication of two transforms:

$$D(f) = \Psi_{prim}(f) A_{pri+sc}(f), \quad (9)$$

where $D(f)$, $\Psi_{prim}(f)$ and $A_{pri+sc}(f)$ are Fourier transforms of respective functions.

Than deconvolution in frequency domain can be written as:

$$\Psi_{prim}(f) = D(f) / A_{pri+sc}(f). \quad (10)$$

With the aim to improve calculation speed of the software developed, Fast Fourier Transform method (FFT) was implemented.

To calculate the dose, absorbed in homogeneous phantom, at the plane of interest, FFT was performed for the EPID dosimetric image, and EPID specific absorption and scatter kernel. Than these two transforms were divided in frequency domain, resulting in Fourier transform of primary photon energy fluence in air. Than result was multiplied by Fourier transform of water equivalent media absorption and scatter kernel, resulting in Fourier transform of dose distribution in water at the plane of interest. Than inverse FFT was applied to the result so providing in dose distribution in time domain.

To avoid EPID dosimetric image noise amplification during deconvolution, optimal Wiener filtering was build into deconvolution equation at the stage of software implementation. Finally used deconvolution algorithm was described as following:

$$\Psi_{prim}(fx, fy) = D^{EPID}(fx, fy) A_{pri+sc}^{EPID} / \left[A_{pri+sc}^{EPID} + F \right], \quad (11)$$

where D^{EPID} – value of EPID dosimetric image; A_{pri+sc}^{EPID} – EPID primary and scattered radiation energy absorption and transfer function; fx, fy – dose distribution matrix indices in frequency domain; F – constant coefficient, equal to EPID noise to signal ratio (NRS) ($NRS^{EPID} \sim 0.02$).

When primary photon fluence in air is known, absorbed dose distribution can be calculated virtually in any media, using convolution with media specific scattering and absorption kernel. For convolution Fourier transforms of respective functions were used as well:

$$D^{H_2O}(fx, fy) = \Psi_{prim}(fx, fy) A_{pri+sc}^{H_2O}, \quad (12)$$

where $A_{pri+sc}^{H_2O}$ – energy absorption and scattering kernel for water equivalent media.

To calculate primary photon energy fluence form EPID dosimetric image corrected according to equation (1) there is need to know EPID specific scattering and absorption kernel A_{pri+sc}^{EPID} in discrete form. For current work were used A_{pri+sc}^{EPID} values, calculated using Monte Carlo simulation.

Water scatter and absorption kernel $A_{pri+sc}^{H_2O}$ values were obtained from Eclipse (Varian Medical Systems, USA) Treatment Planning System database for water equivalent depth of 5 cm. $A_{pri+sc}^{H_2O}$ in treatment planning system are sum of the monoenergetic kernels, with weights assigned according to linear accelerator photon beam energy spectrum. Monoenergetic kernels used in TPS are calculated for the manufacturer by Monte Carlo BEAM code. $A_{pri+sc}^{H_2O}$ kernels were verified during TPS commissioning for all clinically used phantom and radiation field geometrical combinations.

Dose distribution in water, calculated from a real fluence map, formed by delivery of leaf motion sequence by dMLC and linear accelerator system is obtained using proposed calculation method. Dose distribution calculation in water is done for depth of 5 cm, as this is depth clinically used for verification measurements of 6 MeV IMRT fields.

Method for calculation of dose distributions was implemented in the corresponding software, which allows clinical use of proposed method.

2.4. Experiment

Test fields with intensity modulation were developed for the verification of new dosimetry method. Test fields have different fluence modulation and therefore different gradients inside the field.

Field with low fluence intensity modulation inside the field was developed to test proposed method. This field is delivered by means of dMLC, and fluence distribution is similar to one from static field of same size (Fig. 2). Aim of this field is to verify proposed calculation method for minimally possible gradient inside the field.

Field with high fluence modulation, delivered by means of dMLC was developed to test proposed method with extreme leaf motion speeds and, respectively with maximally possible fluence gradients inside the field (Fig. 2). There was region with zero fluence inside this field.

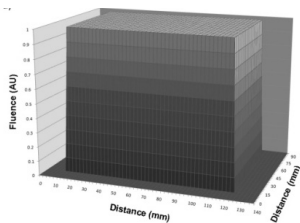


Fig. 1. Uniform fluence, developed for field with low intensity modulation

All test fields were developed using Eclipse TPS (Varian Medical Systems, ASV). TPS leaf motion calculator recalculated manually painted fluence to leaf motion sequence, for further transfer to linear accelerator and dMLC system.

Verification of developed method was performed for 2 clinical fields originally developed for Head and Neck cancer patient, receiving IMRT in Latvian Oncology Center of Riga Eastern Hospital.

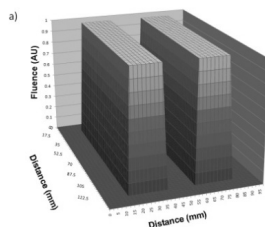


Fig. 2. Non-uniform fluence, developed for field with high intensity modulation.

Measurements were performed in Radiotherapy Department of the Latvian Oncology Center of Riga Eastern Hospital. For delivery of IMRT fields with dynamic intensity modulation was used clinical linear accelerator Clinac 2100 C/D (Varian Medical Systems, USA) equipped with dynamic MLC with 60 leaf pairs (Millennium MLC-120 Varian Medical Systems, USA).

For all verified fields was used photon beam with nominal energy 6 MeV and accelerator dose rate 300 Monitor Units (MU)/min.

To compare dose distributions obtained by means of dosimetry method developed in frames of current work with film dosimetry results was used Open Source software DoseLab version 4.0.

2.5. Evaluation of the results

For error calculation was used modification of the equation proposed by International Atomic Energy Agency (IAEA) report No. 430 for dose calculation error derivation in the point of interest [9]:

$$\delta(x, y) = 100 \times \frac{D(x, y)^{EPID} - D(x, y)^{filma}}{D^{\max, filma}}, \quad (13)$$

where $\delta(x, y)$ - dose calculation error at two-dimensional dose distribution point with coordinates x and y respectively (%); $D(x, y)^{EPID}$ - dose in a point with coordinates x, y , in homogeneous water phantom, for IMRT test phantom geometry, calculated from EPID dosimetric image by means of developed method (Gy); $D(x, y)^{filma}$ - dose in a point with coordinates x, y , measured in IMRT test phantom by means of film dosimetry (Gy); $D^{\max, filma}$ - maximum dose in two-dimensional dose distribution, measured in IMRT test phantom by means of film dosimetry (represents prescribed dose) (Gy).

For IMRT fields it is not feasible to use only dose direct dose error comparison, as are areas with high dose gradients, where very big errors can arise due to small spatial uncertainty in registration of dose distributions, for example. Therefore calculated dose distributions was tested using Gamma Evaluation method proposed by Low et al. [10]. Method compares two-dose distributions using dose deviation criteria if gradient is small and Distance to Agreement Criteria (DTA) in presence of high dose gradient. Gamma Evaluation results in gamma (γ) values distribution, with gamma value assigned to each point of tested dose distribution. To evaluate dose distributions calculated from EPID dosimetric images with film dosimetry results was used Gamma Evaluation equation modified for two-dimensional case, as implemented in DoseLab software [Error! Bookmark not defined.]. From clinical point of view, acceptable dose error is defined as $\pm 3\%$ and acceptable spatial uncertainty of ± 3 mm. Therefore for gamma evaluation were used agreement criteria's as $\Delta D_M = \pm 3\%$ and $\Delta d_M = \pm 3$ mm, respectively.

To evaluate uncertainty of developed dosimetric method, all calculated dose distributions were assessed after dose measured by film using: dose error for each point of dose matrix (%); mean dose error for whole two-dimensional dose distribution (%); error standard deviation for whole two-dimensional dose distribution (%); gamma index for each point of dose matrix; mean

gamma index for whole two-dimensional dose distribution.

Results and Discussion Table 1 shows results. From table data one can see that maximal standard deviation of error is 2.88%, for test field with high intensity modulation. Mean errors are very close to zero, which is showing very small probability of systematic error. On average clinical fields are showing better statistic as compared to test fields. Gamma evaluation results for test fields show that dose distributions calculated using dosimetry method developed in this work are in good agreement with film measurements – for field with low intensity modulation only 3.1% of the field points are exceeding gamma index 1. For field with high intensity modulation 5.9% of field points are exceeding gamma index 1. In clinical fields, only 0.2% and 0.8% from dose distributions are exceeding gamma index 1, for clinical field with relatively high and relatively low intensity modulation respectively. Method error according to test data is 2.88% for 0.68 confidence interval and 5.76% for 0.96% confidence interval respectively. This is in good agreement with precision requirements in radiotherapy of 3% for confidence interval 0.68.

Table 1. Uncertainty estimation results for proposed dosimetry method for test and clinical intensity modulated fields

Field	Mean error $\bar{\delta}$ (%)	Error standard deviation σ (%)	% from field where error $\leq \pm 3\%$	Mean gamma index	% of field where $\gamma < 1$
Test field with low intensity modulation	0.196	2.22	88.6	0.34	96.9
Test field with high intensity modulation	0.278	2.88	82.0	0.42	94.1
Clinical field with high intensity modulation	0.272	2.56	86.1	0.33	99.8
Clinical field with low intensity modulation	0.1	1.64	93.7	0.29	99.2

For each tested dose distribution, error and gamma index frequency distributions were presented in graphical form.

Figure 3 shows calculated from EPID dosimetric image and measured by means of film dosimetry profiles for test field with low intensity modulation, with deviation calculated using equation (16). It can be seen from the image that all deviations bigger than 2% are concentrated in region of high dose gradient in field penumbra. Bigger deviations in high dose gradient area can be attributed to dose matrixes registration uncertainties, and to different resolution of dose distributions. From EPID dosimetric image calculated dose distribution has pixel size of 0.747 mm (as projected

to 100 cm) but film dosimetry dose distribution has pixel size of 0.339 mm.

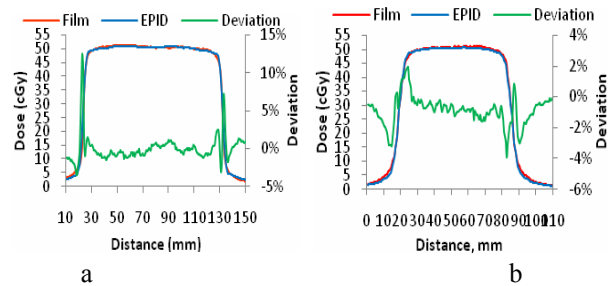


Fig. 3. Dose profiles and deviation for test field with low intensity modulation. a) profiles in direction perpendicular to the dMLC leaf motion; b) in direction parallel to the leaf motion

Figure 4 shows calculated from EPID dosimetric image and measured by means of film dosimetry profiles for test field with high intensity modulation with calculated deviation. Values of deviation are higher not only in field penumbra region as in the previous case, but also in high gradient region inside the field. These higher deviation values can be attributed to the same reasons like in previous case.

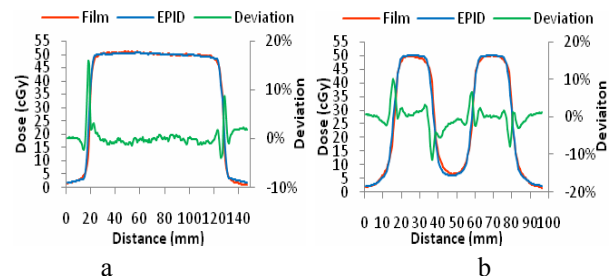


Fig. 4. Dose profiles and deviation for test field with high intensity modulation. a) profiles in direction perpendicular to the dMLC leaf motion; b) in direction parallel to the leaf motion

Figure 5.a. shows two-dimensional distribution of gamma index for test field with low intensity modulation. Each pixel on the image is in accordance to pixel in dose distribution calculated from EPID dosimetric image. Figure 5.b. shows gamma index histogram for corresponding field.

One can see good gamma evaluation results for the test field with low intensity modulation. Small area in the middle of the field where gamma indexes are bigger than 1 is attributable to backscatter from the stem of ionization chamber to the film (chamber body was positioned 1.5 mm below the film). All the rest of the areas with gamma index exceeding 1 are inside penumbra region.

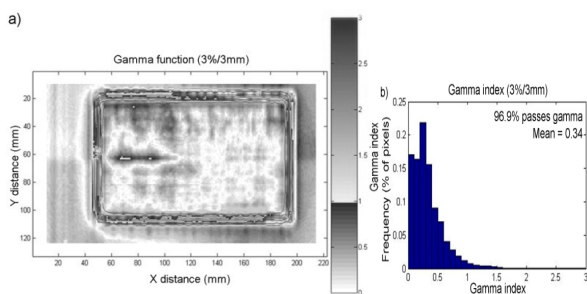


Fig. 5. Gamma distribution for test field with low intensity modulation. a) two-dimensional gamma distribution image; b) gamma indexes histogram

Figure 6 shows gamma evaluation results for test field with high intensity modulation. Area of higher gamma values in the low dose part of the field is attributable like in previous case to the backscatter from the stem of the chamber. All the rest of areas exceeding gamma evaluation criteria are located in the high dose gradient areas of the dose distribution.

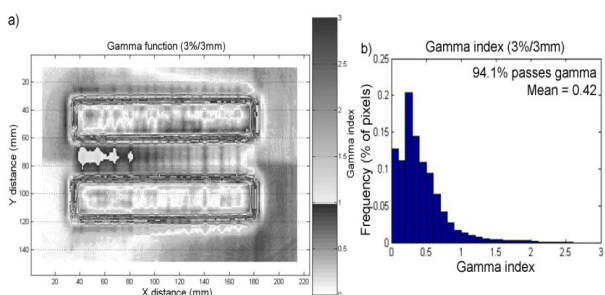


Fig. 6. Gamma distribution for test field with high intensity modulation. a) two-dimensional gamma distribution image; b) gamma indexes histogram

Figure 7.a shows error histogram for clinical field with high intensity modulation. Figure 7.b shows error histogram for clinical field with low fluence modulation.

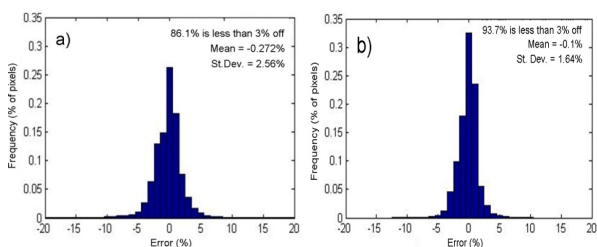


Fig. 7. Error histograms for the clinical fields with a) high intensity modulation and b) low intensity modulation

Figure 8 shows gamma evaluation results for clinical field with high fluence modulation. Practically all field shows agreement with acceptance criteria 3%/3mm. One can see small areas in the lower part of the field, where gamma index is exceeding 1. This is explainable with very high dose gradient is this part of the field.

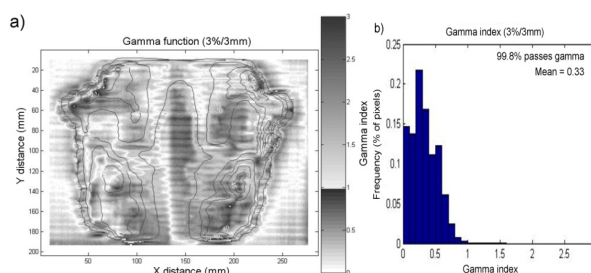


Fig. 8. Gamma distribution for clinical field with high intensity modulation. a) two-dimensional gamma distribution image; b) gamma indexes histogram.

3. Conclusions

New dosimetry method for Intensity Modulated Radiotherapy fields was developed, allowing to estimate from two-dimensional dose distribution, acquired using Electronic Portal Imaging Device, two-dimensional dose distribution in water equivalent phantom. New method can be used for patient related clinical dosimetry in all hospitals, using dynamic Intensity Modulated Radiotherapy. Method is using portal

4. References

1. The modern technology of radiation oncology. Ed. JV Dyk. – USA: Medical Physics Publishing, 1999. – 1072. pp.
2. Khan F. M. The Physics of Radiation Therapy. – USA: Lippincott Williams & Wilkins, 2003. – 560. pp.
3. Ezzell G. A., Galvin J. M., Low D. et al. Guidance document on delivery, treatment planning, and clinical implementation of IMRT: Report of the IMRT subcommittee of the AAPM radiation therapy committee// Med. Phys. – 2003. – 30. – 2089.- 2115. pp.
4. Childress N.L., Dong L., Rosen I.I. Rapid radiographic film calibration for IMRT verification using automated MLC fields// Med Phys. – 2002. – 29. – 2384.-2390. pp.
5. DoseLab software homepage / Internet. – <http://www.doselab.com>
6. Attix F.H. Introduction to Radiological Physics and Radiation Dosimetry. - USA: John Wiley and Sons, 1986. – 607. pp.

7. Johns H.E., Cunningham J.R.. The Physics of Radiology. 4th edition, USA: Charles C Thomas Publisher, 1983. - 796. pp.
8. Numerical Recipes in C. The Art of Scientific Computing. Second Edition. Press W.H., Teukolsky S.A., Vetterling W.T. et al./ New York: Cambridge University Press, 1999. – 994. lpp.
9. International Atomic Energy Agency: Technical Report Series No. 430./ Comissioning and Quality Assurance of Computerezed Planning Systems for Radiation Treatment of Cancer, - Austria: IAEA, 2004. – 281. pp.
10. Low D.A., Harms W.B., S.M. and Purdy J.A.. A technique for the quantitative evaluation of dose distributions// Med. Phys. – 1998. – 25. – 656.-661. pp.

APPLICATION OF COLD AND HEAT CONTRAST THERAPY DEVICE IN THE TREATMENT OF MYOFASCIAL TRIGGER POINTS

Laimonas ŠIUPŠINSKAS* **, Sigitas TAMULEVIČIUS*, Rimantas GUDAITIS*, Alfonsas VAINORAS**

*Kaunas University of Technology, Institute of Physical Electronics;

**Kaunas University of Medicine, Department of Kinesiology and Sports Medicine

Abstract

Aim of the study was to assess effects of cold and heat contrast therapy device in the treatment of myofascial trigger points. Device (patent number A61F 7/00), originally constructed in Kaunas University of Technology, Institute of Physical Electronics was used in this research. 37 computer users with pain and discomfort symptoms in the neck and shoulder area were recruited for this research. Used stretching exercises and cold-heat contrast therapy reduced pain in the neck and shoulder area ($p < 0,05$). The best effect in the treatment of myofascial trigger points had cold – heat contrast therapy.

Keywords: heat and cold device, contrast, myofascial trigger points, treatment

1. Introduction

Nowadays, when computers are the main working tool for lot of us, many people are suffering from musculoskeletal pain. According data from Occupational Safety and Health Administration (OSHA) about 90 % of computer users are suffering (or will suffer) from work-related musculoskeletal injuries [1]. The first sign of such a lesion is discomfort leading to pain. It's an unpleasant sensory and emotional experience associated with actual or potential tissue damage, or described in terms of such damage [2]. The most often cause of work-related pain is long lasting static contraction of posture muscles. As a result, myofascial trigger points are forming in the tired muscles triggering discomfort and pain [3]. Myofascial trigger points represent a major cause of sustained pain, as well as muscular, nervous system, and soft tissue dysfunction. Extensive research and experiential results show that all chronic pain conditions produce trigger points. Myofascial trigger points represent small areas of tightness within muscles, creating tight bands and "knots" or tiny bumps from the contracted muscle fibers. It's a sensitive spot in a taut band of a skeletal muscle that is painful on compression and/or stretch and that can give rise to a typical referred pain pattern. The most effective methods of treatment of trigger points involve local ischemic compression and cold or heat applications [4]. Application of separate heat and cold agents are widely discussed in scientific literature. The decrease of tissue temperature produced by cold agent may directly reduce the sensation of pain. Applying cold for 10 – 15 minutes can control pain for 1 or more hours. Effects of cold involve initial decrease and later

increase in blood flow, decrease nerve conductivity, increase pain threshold, alter muscle strength, decrease spasticity, facilitation of muscle contraction. Cold has been demonstrated to be effective in the treatment of myofascial pain [7]. Its analgesic effect is probably one of its greatest benefits with ability to reduce muscle spasm [8]. Within rehabilitation, heat is used primarily to control pain, increase soft tissue extensibility, increase circulation and accelerate healing. Heat has these therapeutic effects due to its influence on hemodynamic, neuromuscular, and metabolic processes [5]. Local superficial heating is recommended in subacute conditions for reducing pain and inflammation through analgesic effects. Superficial heating produces lower tissue temperatures in the site of the pathology relative to the higher temperatures in the superficial tissues, resulting analgesia. Heat dilates blood vessels, causing the patient capillaries to open up and increase circulation [8]. The rate of metabolism of tissues depends partly on temperatures. The metabolic rate has increased approximately 13% for each 1°C increase in temperature [9]. A lot of devices are used in physiotherapy in order to treat tender points in the muscles and to reestablish normal muscle function. Acupuncture, dry needling and injection into trigger points, laser and magnetic treatment, microcurrent, ultrasound and hydrotherapy devices are available on the market. Unique device (patent number A61F 7/00) [10], originally constructed in Kaunas University of Technology, Institute of Physical Electronics includes the main physical agents (compression and cold and heat) needed for the treatment of trigger points. The main task of the research is to assess effectiveness of

cold-heat contrast therapy device in the treatment of myofascial trigger points.

2. Experimental

2.1. Cold-heat contrast therapy device

The device used in this research consists of a controller and thermoelectric module (TEM) (Fig. 1).



Fig. 1. View of the cold – heat contrast therapy device

The basis of controller is a microprocessor pic 16f628 with a program. According to written control protocols and in association with the data input device („rotary encoder”), LCD indicator and analogue – code converter controls the thermoelectric module (TEM) (Fig. 2). Depending on the direction of the current flow, the thermoelectric module (TEM) will either absorb or release the heat. Depending on the difference of the real and necessary temperatures of the thermoelectric module (TEM), voltage of the necessary direction and value for the thermoelectric module (TEM) are outgoing.

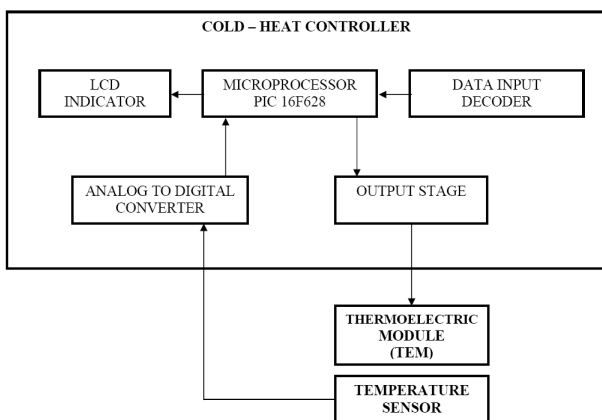


Fig. 2. The principle scheme of the cold – heat contrast therapy device [6]

The contact surface of the thermoelectric module (TEM) is a 10 mm diameter rounded edged copper „finger” which can be cooled up to -20 °C and can be

heated up to +50°C. Resolution of temperature is 0.5 °C, maximal temperature ramp rate - 40 °C/min. It has a contact with a Peltier element and transmits heat directly to the skin. Compression with a copper “finger” and cold-heat contrast can be used simultaneous for the maximal effectiveness of treatment.

2.2. Patients and methods

In order to assess the effectiveness of the cold-heat contrast therapy device we have recruited 37 computer users (33.4 ± 4 years old) with discomfort and pain in the upper part of the body (neck and shoulders). The average hours per day spent on the computer was 6.5 ± 09 . The painful points (myofascial trigger points) were assessed by algometer - the diagnostic device for measuring pain caused by pressure. Each point was pressed with the 5 kg/cm² pressure and patient was asked to evaluate felt pain in 10 score system (0 – no pain, 10 – severe pain) (VAS – visual analogue scale). The most common, standard locations of trigger points in the upper part of the body were tested according Travell and Simons’ topographical charts [3]. After the initial investigation, patients were divided into 3 groups: 15 patients were asked to do stretching exercises 3 times per day for 6 weeks according the given program; 10 patients had 10 procedures of cold-heat contrast therapy and 12 patients were in control group (recommendations were given after the experiment). The procedures of cold-heat contrast therapy were given with intermittent compression together with 70 s of -10 °C of cooling and 90 s of +45.2°C of heating of each trigger point. After 6 weeks of the application of stretching exercises and cold-heat contrast therapy we have reevaluated patients. Control group was reevaluated after 6 weeks too.

3. Results

3.1. Measurement of pain

The average initial pain in myofascial trigger points in all 3 groups was similar (no significant difference) and varied from 1.8 to 8.4 score. So we can state that groups were homogeneous. Changes of myofascial trigger point’s pain before and after the application of stretching exercises, cold-heat contrast therapy and in the control group are presented in Fig. 3.

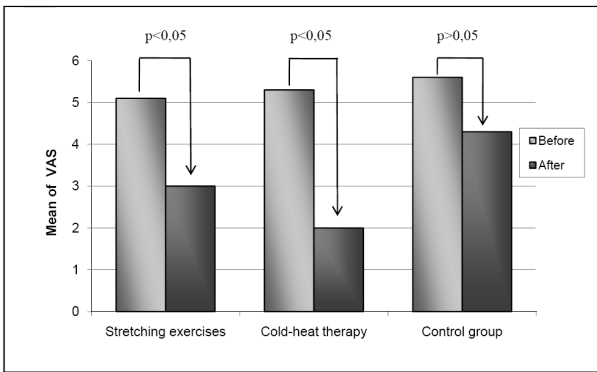


Fig. 3. Total changes of myofascial trigger point's pain before and after the application of stretching exercises, cold-heat contrast therapy and in the control group.

3.2. Effects of stretching exercises

After 6 weeks of individually done stretching exercises for head and shoulder muscles 28.6% of patients reported absence of pain, 50% had less pain, in 14.3% pain stayed at the same level and 7.1% reported increased pain. The main reason of increased pain was sustained work on the computer and not enough frequent done stretching exercises. In 31.3% of found myofascial trigger points pain was statistically significant decreased ($p < 0.05$) (Fig. 4)

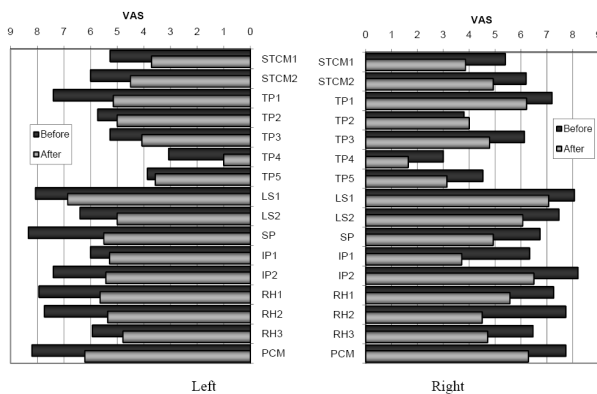


Fig. 4. Level of myofascial trigger points pain before and after the application of stretching exercises

3.3. Effects of cold-heat contrast therapy

After the session of 10 procedures during the 6 weeks 25% of patients reported absence of pain and 75% claimed that pain was significantly reduced by the cold-heat contrast therapy. Pain, measured in VAS (visual analogue scale) in the initial testing varied from 4 to 8 score, while after cold-heat therapy score was from 0 to 4. The most noticeable effect of therapy was observed in reducing pain of myofascial trigger points. Reduced pain was observed in 81.3% of trigger points ($p < 0.05$) (Fig. 5).

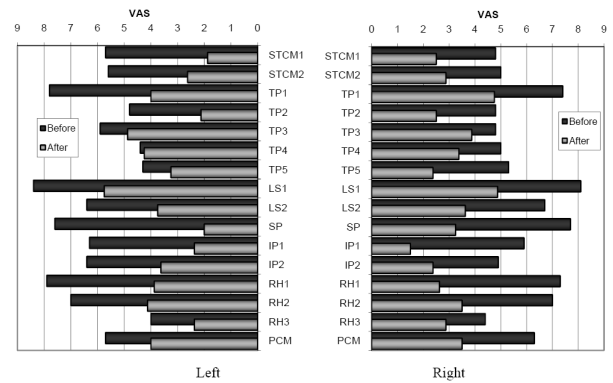


Fig. 5. Level of myofascial trigger points pain before and after the application of cold-heat contrast therapy

3.3. Control group

70% of patients in the control group reported the same level of pain in trigger points after 6 weeks. In 20% - the pain increased and in 10% - decreased. The main reason of decreased pain was start of doing physical exercises individually. The pain of myofascial trigger points increased after 6 weeks period (21.9% statistically significant, ($p < 0.05$)) (Fig. 6).

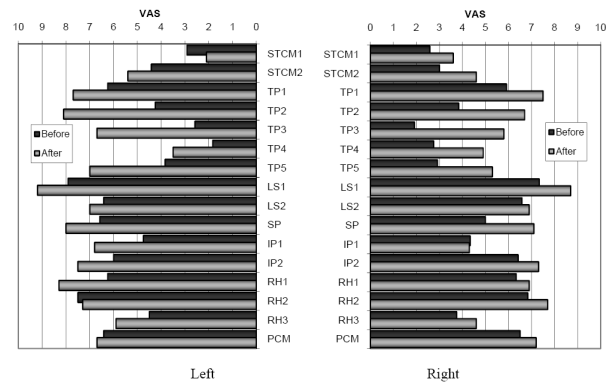


Fig. 6. Level of myofascial trigger points pain before and after 6 weeks in the control group

4. Conclusions

The stretching exercises and cold – heat contrast therapy statistically significant ($p < 0.05$) reduced pain in the neck and shoulders. Stretching exercises reduced pain duration and frequency and had effect on daily life activities, meanwhile cold-heat contrast therapy statistically significant ($p < 0.05$) reduced most (83%) of found myofascial trigger points. In the control group was no change of 70% of patients and 20% of them had intensified pain in the neck and shoulder area. Control group also had pain intensify of myofascial trigger points, 22% of them – statistically significant ($p < 0.05$). In conclusion, the best effect on neck and shoulder muscles and discomfort/pain in this area had the cold-heat contrast therapy. Many scientific papers proof effectiveness of complex use of intermittent ischemic compression, stretching, heat, cold in the treatment of

myofascial trigger points. This research showed clear indications for trigger points treatment: acute pain – cold-heat contrast therapy, chronic pain – stretching exercises for treatment and prevention of muscle pain.

5. References

1. European Agency for Safety and Health at Work. Every year millions of European workers are affected by work related musculoskeletal disorders (MSDs). <http://osha.europa.eu/topics/msds>
2. Classification of Chronic Pain, Second Edition, IASP Task Force on Taxonomy, edited by H. Merskey and N. Bogduk, IASP Press, Seattle, 1994, pp 209-214.
3. Travell J.G., Simons D.G. Myofascial pain and dysfunction: the trigger point manual. Baltimore: Williams & Wilkins, 1983.
4. Chaitow L., Fritz S. A massage therapist's guide to understanding, locating and treating myofascial trigger points. Churchill Livingstone Elsevier, 2006
5. Cameron M.H. Physical agents in rehabilitation. From research to practise. St. Louis: Saunders, 2003.
6. Gudaitis R., Tamulevičius S. Žmogaus raumens šaldymo ir šildymo įrenginys // Elektronika ir elektrotechnika. – Kaunas: Technologija, 2005.- N 5(61).- P.44-47.
7. Travell, J. Rapid relief of akute „stif neck“ by ethyl chloride spary, Am. Med. Wom. Assoc. 4(3):89-95, 1949.
8. Prentice W.E. Therapeutic modalities in rehabilitation. New York: McGraw-Hill, 2005.
9. Hocutt, J., Jaffe, R., and Rylander, C.: Cryotherapy in ankle sprains, Am. J. Sports Med. 10(3):316-319, 1992.
10. Žmogaus raumens šildymo ir šaldymo įrenginys (angl. Heating and Cooling Device of Human Muscles). Tarptautinės patentų klasifikacijos indeksas - A61F 7/00. Išradėjai: Vytautas Ostaševičius, LT; Sigitas Tamulevičius, LT; Rimantas Gudaitis, LT.

PATIENT RELATED QC OF COMPLEX HDR BRACHYTHERAPY TREATMENTS

Albert Miller*, Ieva Simutyte*, Romualdas Griskevicius*, Sergey Popov**

*Institute of Oncology, Vilnius University, Vilnius, Lithuania, **Latvian Oncology Center, Riga, Latvia

Abstract

The patient related QC of very complex HDR brachytherapy plan was performed with anthropo-morphic CIRS phantom. Point doses were measured with small volume ionization chambers. Good agreement of measured doses and volume optimized plan doses was achieved. The time needed for verification procedure is in order of 40 min, which is feasible and is comparable with time of IMRT plan verification.

Keywords: brachytherapy, dose, verification

1. Introduction

The most of brachytherapy applications nowadays uses from one to three catheters for treatment of esophageal, bronchial, rectum and gynecological tumors. The treatment planning for these cases is rather standard and do not requires neither volume optimization, nor unusual dwell times distribution. The final treatment time verification of these plans is performed by means of independent quite simple and most of the times in house developed computer programs. Even more, the dose and dwell times distribution for these treatments are very well known. Therefore, experienced physicist most likely will recognize the possible error in the treatment plan intuitively. However, the verification of more complex plans where up to 20 catheters are irradiating large and highly irregular treatment volume may become difficult. The scope of this investigation was to demonstrate feasibility of HDR brachytherapy plans verification with anthropomorphic IMRT phantom.

2. Material and methods

The HDR brachytherapy treatment plan produced within commercial software Brachyvision was used for verification. As representative example, the authors have chosen the treatment of chest wall with standard tissue equivalent surface applicator 30x30 sq.cm and 16 catheters of 100 cm each placed into it. The plan was volume optimized to deliver prescribed dose to PTV (Fig.1)

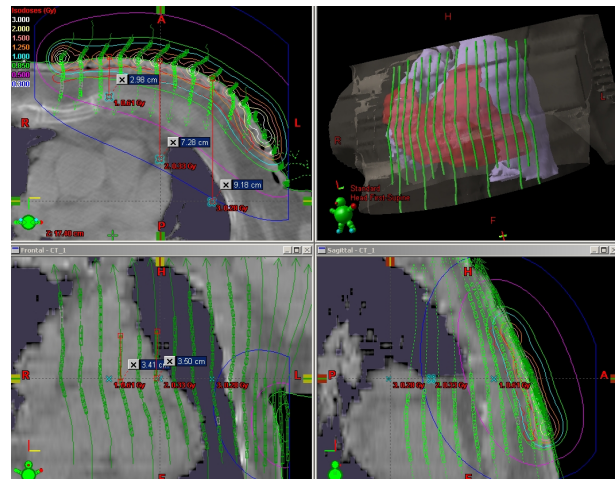


Fig. 1. Dose distribution and catheters arrangement of volume optimized patient treatment plan.

The same surface applicator was positioned at the anthropomorphic CIRS thorax phantom. Three small volume ionization chambers (0.125 cc) were inserted into specially designated holes, representing mediastinum point, soft tissue point and lung point. The distance from the sources paths to the probe centers was at least 3 cm to minimize the effect of large dose heterogeneity through chamber sensitive volume. The phantom with probes and surface applicator in place was CT scanned and treatment plan with real patient plan dwell times was overlaid on 3D image of the phantom. The phantom with ionization chambers was than treated to the normalized dose of 1 Gy to prescribed isosurface (Fig.2). Measured doses were compared to the planned phantom doses at the same points. In addition, the measuring phantom points were identified on the actual patient treatment plan in relation to the applicator position (see points 1, 2 and 3 on the Fig.1). Three sets of measured and calculated point doses are collected and presented in the Table 1.



Fig. 2. The patient related QC set up with CIRS thorax phantom and inserted three small volume ionization chambers. Sixteen catheters are connected to HDR treatment unit.

3. Results and discussion

The results of point dose measurement with ionization chambers in the thorax phantom and dose at the correspondent points calculated by the treatment planning system in patient and in the phantom are presented in the Table 1.

Table 1. The result of patient related QC procedure.

	Mediastinum point No.1	Soft tissue point No.2	Lung point No.3
Ionization chamber measurement	0.59 Gy	0.3 Gy	0.265 Gy
Patient plan point dose	0.61 Gy	0.33 Gy	0.28 Gy
Phantom plan point dose	0.58 Gy	0.29 Gy	0.22 Gy

The obtained calculated and measured dose values for point No. 1 are in very good agreement (within 3 %). For the soft tissue point No. 2 the agreement between measured and calculated dose in the phantom is still good – within 3 %. However, measured in the phantom and calculated in the patient doses agreement is only in order of 10 %. The reason for this large discrepancy is most probably the noticeable difference in patient and phantom chest wall curvature.

The discrepancy between measured and calculated dose in the thorax phantom for the lung point No. 3 is very large – 17 %. However, this discrepancy one would expect considering the fact that brachytherapy treatment planning algorithm does not take into account heterogeneity for the calculation.

4. Conclusions

The patient related QC using anthropomorphic phantom and point dose measurements with small ionization chamber is feasible and reliable procedure for complex HDR treatments. For the points in the homogeneous media and at the distance about 3 - 4 cm from the source path, agreement within 5 % between measured and calculated in the phantom doses would indicate acceptance of the plan for the further treatment.

5. References

1. Bakai A, Alber M, Nüsslin F (2003) A revision of the evaluation concept for the comparison of dose distributions. *Phys Med Biol* 48:3543–3553
2. Bucciolini M, Buonamici FB, Casati M (2004) Verification of IMRT fields by film dosimetry. *Med Phys* 31:161–168
3. Depuydt T, Van Esch A, Huyskens DP (2002) A quantitative evaluation of IMRT dose distributions: refinement and clinical assessment of the gamma evaluation. *Radiother Oncol* 62:309–319
4. Dogan N, Leybovich LB, Sehti A (2002) Comparative evaluation of Kodak EDR2 and XV2 films for verification of intensity modulated radiation therapy. *Phys Med Biol* 47:4121–4130
5. Esthappan J, Mustic S, Harms WB, Dempsey JF, Low DA (2002) Dosimetry of therapeutic photon beams using an extended dose range film. *Med Phys* 29:2438–2445
6. Ezzel GA, Galvin JM, Low DA, Palta JR, Rosen I, Sharpe MB, Xia P, Xiao Y, Xing L, Yu C (2003) Guidance document on delivery, treatment planning, and clinical implementation of IMRT: report of the IMRT subcommittee of the AAPM radiation therapy committee. *Med Phys* 30:2089–2115

IMPLEMENTATION OF THE INDEPENDENT DOSE CALCULATION ALGORITHM FOR THE CHECKING OF THE Co-60 UNIT TREATMENT PLANS

Marius LAURIKAITIS*, Jurgita LAURIKAITIENĖ***, Diana ADLIENĖ**, Tatjana ZAKREVSKAJA*, Gediminas A. ADLYS**, Saulius RAILA**, Fredrik NORDSTRÖM***, Sven BÄCK***, Sören MATTSSON***
 * Oncological Hospital of Kaunas Medical University Hospital, Volungių g. 16, LT-45434 Kaunas, Lithuania;
 ** Kaunas University of Technology, Physics Department, Studentų g. 50, LT-51368 Kaunas, Lithuania;
 *** Lund University, Malmö University Hospital, Department of Radiation Physics, SE-205 02 Malmö, Sweden

Abstract

The independent dose calculation algorithm was adopted for the Co-60 unit treatment plan checking. Application of the proposed algorithm have shown that 12 % of TPS plans exceeded the 5 % tolerance limit. Estimated deviation between SPR and manual PDD method was within 2 % range for isocentric treatment technique. For the most treatment cases except lung treatment the deviation between SPR method and TPS was within 5 % range.

Keywords: Radiotherapy, Co-60 unit, Dose calculation, Dose plan.

1. Introduction

The requirements for the exact delivering of the prescribed dose in modern radiotherapy are growing fast. All radiotherapy process is computerized – starting from the patient data mapping to the treatment delivery. In one or other part of all these process the errors may occur. It was reported, that in 15 % of plans the errors are presented [1]. The differences in the prescribed dose larger than 5%, may influence the clinical outcome of the treatment [2]. This might be prevented if the treatment plans are checked before the first treatment. Almost all radiotherapy clinics are checking the plans using the different calculation algorithms but with the same input data that is used in the treatment planning system (TPS). However it is much better to use independent calculation algorithms that use different input data than TPS algorithms, for reducing errors in the plans.

The gammatherapy treatment (Co-60 source) is quite popular in Lithuania, however not only these therapy units are old but the planning systems that are used for this treatment planning are also very old. Due to these reasons a lot of mistakes are possible. To reduce the probability of errors, the treatment plans should be checked before treatment using different from the TPS checking algorithm.

In this work an independent calculation algorithm for checking of radioactive source (Co-60) plans is presented. This algorithm is slightly changed version of the algorithm that is used for the checking of the dose plans at linear accelerator[3].

2. Material and methods

2.1. The calculation method

The absorbed dose D at the point of calculation can be divided into its primary (subscript p) and scatter (subscript s) components. Primary dose is a dose delivered to the target by the photons that have not interacted previously in the irradiated volume. Scattering dose is a dose delivered to the target by the photons that have at least once interacted before. The total absorbed dose D can be written as:

$$D = D_p + D_s = \beta_p K_p + \beta_s K_s, \quad (1)$$

where K – kerma, and β – dose-to-kerma ratio. The scattering dose is nearly equal to scatter kerma [4], so we can consider that $\beta_s = 1$. By defining the scatter-to-primary kerma ratio $\sigma = K_s / K_p$, the total dose can be written as $D = K_p (1 + \sigma)$. It is possible to write primary kerma as $K_p = K_{p,0} T$, where $K_{p,0}$ – “free in-air” primary kerma (primary kerma at the calculation point without surrounding medium), T – transmission factor, which accounts for the attenuation of the primary kerma in the medium. The “free in-air” primary kerma relative to a reference field $K_p^{rel} = K_{p,0} / K_{p,0,ref}$ is measurable quantity [5], which depends on the collimator setting c , defined at isocenter (the head-scatter factor $H(c)$), the distance f from the X-ray source (the inverse-square law $I(f)$), and the presence of a tray factor for block support (transmission factor of the shadow tray $k_{0,t}(c)$):

$$K_{p,0}^{rel}(c, f) = H(c) \cdot I(f) \cdot k_{0,t}(c). \quad (2)$$

The head-scatter factor H is given by:

$$H(c) = \frac{a_1 + a_2 c}{1 + a_3 c + a_4 c^2}, \quad (3)$$

where a_n – the coefficients, c – the square field size.

The inverse-square law I :

$$I(f) = \left(\frac{f_{ref}}{f} \right)^2, \quad (4)$$

where f – the distance between the source and the calculation point, f_{ref} – the reference distance.

By relating the dose-per-time D/t to the reference situation, the final expression for the absorbed dose D in the medium can be written as:

$$D = t \left(\frac{D}{t} \right)_{ref} K_{p,0}^{rel} \frac{T(1+\sigma)}{T_{ref}(1+\sigma_{ref})}. \quad (5)$$

The transmission factor T for the radioactive source (Co-60) is defined by an exponentially based linear attenuation coefficient μ in water for the primary photons:

$$T(z) = e^{-\mu z}, \quad (6)$$

where z – the depth at the calculation point.

For the determination of the scatter and the primary kerma ratio, the semi-empirical formalism [6] has been used:

$$\sigma(s, z) = \frac{a \cdot s \cdot z}{w \cdot s + z}. \quad (7)$$

The field size s corresponds to equivalent square field size at the depth z in the medium. The parameters a and w are linear functions of the linear attenuation coefficient μ [7].

Heterogeneities in the patient are handled by replacing the physical depth with the radiological depth for transmission of the primary kerma. Only bulk densities are used for lung (0,3 g/cm³) and bone (1,2 and 1,5 g/cm³).

The algorithm that is described above was computerized and the “Radiotherapy Verification Program” (RVP) was created. The interface of RVP is represented in Fig. 1. The program was created in Malmö University Hospital (Malmö, Sweden) for the checking of the MU calculations for linear accelerators. Some changes were made to the program in Oncological Hospital of Kaunas Medical University (Kaunas, Lithuania) due to the necessity to use it for the checking of the time calculations for Co-60 unit.

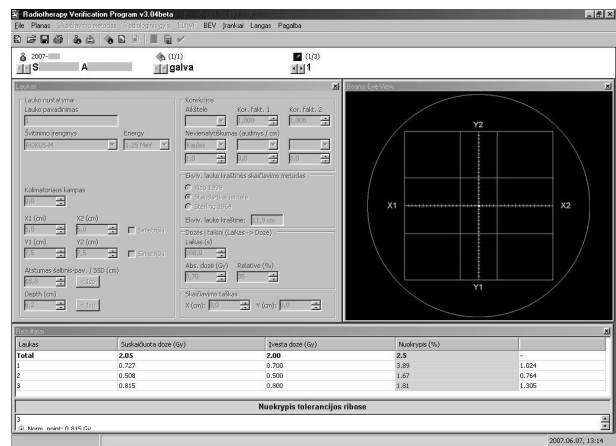


Fig. 1. The “Radiotherapy Verification Program” interface.

2.2. Measurements

The Co-60 linear attenuation coefficient μ was determined from narrow-beam measurements of the clinically used Co-60 unit with NE 2570 1B electrometer and RK 8307 ionizing chamber. The different thickness of cylinder form solid water phantoms were added in front of the chamber. The results were normalized to the depth $z = 0$.

The head-scatter data was collected in air at clinical isocenter ($SAD = 75$ cm) of Co-60 unit with an PTW-UNIDOS electrometer and PTW M31003 ionization chamber. The build-up cap was used also. The results were normalized for field size $c = (10 \times 10)$ cm².

3. Results and discussion

The fitting of the linear attenuation coefficient for the clinically used Co-60 source are shown in the Fig. 2. The value of the determined coefficient is $\mu = 0,0624$ cm⁻¹. In the BJR Supplement 25 the value of Co-60 linear attenuation coefficient in water is $\mu = 0,0657$ cm⁻¹ [8], therefore value of μ for 1,25 MeV photons in water posted by National Institute of standards and Technology is 0,0632 cm⁻¹ [9]. Differences can be explained by the difference between a 1,25 MeV monoenergetic photon beam and a Co-60 clinical radiotherapy beam, which has a photon spectrum differing from the spectrum of photons emitted by Co-60 nuclide.

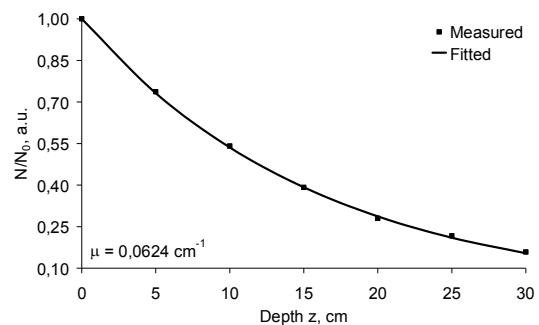


Fig. 2. The determination of the linear attenuation coefficient for the clinically used Co-60 source.

The fitting of the practically measured head-scatter factor is shown in Fig. 3. It was used for the estimation of the coefficients a_n , which are used in the (3). After deriving the linear attenuation coefficient and head scatter factor coefficients, the “Radiotherapy Verification Program” was arranged for the verification of the Co-60 unit dose plans.

The fast checking of the independent algorithm calculations were made, firstly. The time, which was needed to deliver the constant dose to the different sized field was calculated using the independent calculation method (SPR) at isocentric conditions. Calculated time was compared with a time estimated from a simple formalism using manual calculation, based on the percentage dose depth (PDD) evaluation for delivery upon the same treatment conditions. The differences in the times were recalculated to the deviation. The deviation as a function of the field size and the depth is shown in Fig. 4. The deviation is within 2 % range for the different field sizes c ($5 \times 5 - 20 \times 20 \text{ cm}^2$) and depth z (5 – 20 cm). It is good agreement of these two calculation methods. The biggest deviation was observed for the largest fields (more than $17 \times 17 \text{ cm}^2$) and for the biggest depth ($z = 20 \text{ cm}$).

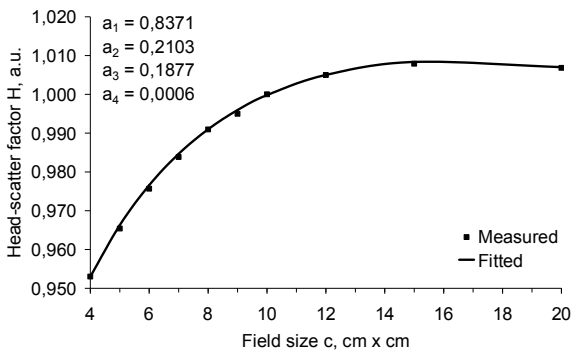


Fig. 3. The determination of the head-scatter factor fitting coefficients for the Co-60 unit.

Due to rather small deviation ($\pm 2 \%$) of these two calculation methods, the decision was made to implement the program in the routine work of the treatment plan checking. The deviation tolerances were increased to $\pm 5 \%$, to cover the deviation ($\pm 3 \%$) of treatment planning system calculations and PDD manual calculations plus the deviation ($\pm 2 \%$) of SPR and PDD method comparison. The decision was made to check manually dose plans using PDD calculation method and to ensure that the calculations made using SPR method do not exceed 5 % tolerance. For manual calculation the tolerance was reduced to $\pm 3 \%$. It was assumed, that in the case when the plan exceeds manual calculation tolerance, it has to be recalculated.

Dose plans at isocentral conditions were prepared for 87 patients and checked by RVP, using SPR method. 208 fields were checked in total. The distribution of the dose deviation after the performed comparison between RVP and TPS is shown in Fig. 4. It could be seen, that

the deviation is concentrated around + 3 %. This shift in deviation curve might be caused by the old 2D planning system calculations. It is not possible to change the beam data in this system. The input data for the calculation program is taken from the dose atlases for Co-60, and have been derived many years ago. After the systematic error was recovered, the decision was made do not use this planning system for isocentric planing.

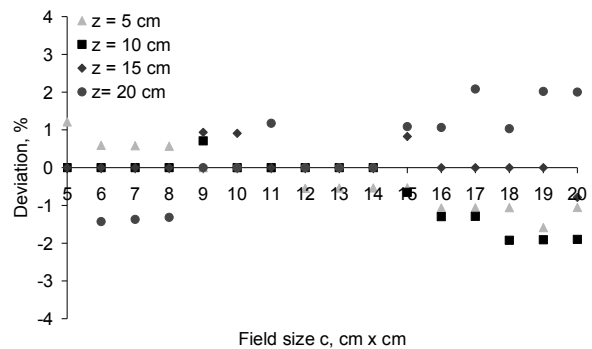


Fig. 4. The deviation from comparison between PDD and SPR as a function of the field size and the depth for Co-60 ($SAD = 75 \text{ cm}$).

The data in Fig. 5 show that 12 % of the planned fields were outside of the tolerance limits. In most cases the results outside tolerance were attributed to heterogeneity effect in the lung. Changes of the physical depth into the radiological depth for SPR method have not shown better results for Co-60 unit calculations.

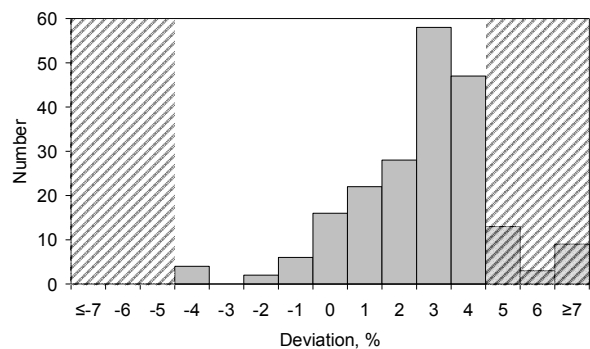


Fig. 5. The distribution of the deviation from comparison between RVP and TPS. The lined area show values, that are outside of determined tolerance ($\pm 5 \%$).

Radiotherapy Verification Program with independent calculation algorithm from the practical point of view is a simple tool for the routine plan checking. It is necessary to mention two cases, when RVP helped to prevent the radiation accident. First mistake was made by personnel. The dose plan has had to be calculated using source skin distance (SSD) method, but due to the mistake of medical physicist it was calculated for source axis distance (SAD) method. Other physicist entered the plan into the RVP as SSD

method. He found that the dose plans prepared using SPR method and PDD method exceed the tolerance limits. After the checking of paper plan it was found that the methods were mixed. This mistake could result in 27 % lower absorbed dose to the patient.

Another mistake was made by treatment planning system. The medical physicist, who was checking plan with the RVP has found, that the treatment field differ by 20,8 % when calculations are performed using SPR method and by 16,5 % calculating by PDD method. This difference resulted in the increased total dose of 9,9 % for SPR and of 6,1 % for PDD. No explanation was found why the TPS made this mistake. Possible explanation could be, that an illegal operation was performed at the moment of calculation, and the system made a big mistake. It is interesting to mention, that the change of the gantry angle of 1 degree into one or other side, the TPS starts to calculate the plan perfect. The TPS error was +13 %, the deviation between SPR and TPS has been changed to 4,6 %, and deviation between PDD ant TPS has been changed to 0,5 %.

4. Conclusions

The Radiotherapy Verification Program with the independent calculation algorithm (SPR) is good and fast tool for routine Co-60 plan checking. It made possible to estimate that 12 % of the dose plans exceeded the tolerance limits for independent checking, and needed manual recalculation of the plans using PDD method. This number will be reduced in the future, due to the closing of the not optimal 2D planning system. The deviation between SPR and manual PDD method is within 2 % range for isocentric treatment technique. For the most treatment cases except lung treatment the deviation between SPR method and TPS is within 5 % range.

Acknowledgements

The authors would like to express their gratitude to International Atomic Energy Agency for founding the fellowship at Malmö University Hospital.

This work was supported by Lithuanian State Science and Studies Foundation.

5. References

1. Valli M.C., Prina M., Bossi A, et al. Evaluation of most frequent errors in daily compilation and use of a radiation treatment chart. *Radiotherapy and Oncology* 32, 1994. p. 87-89.
2. ICRU Report No. 62. Prescribing, recording and reporting photon beam therapy. Bethesda, MD: ICRU, 1999.
3. Johnsson S.A., Ceberg C.P., Nilsson P. A simplistic formalism for calculating entrance dose in high-energy x-ray beams. *Physics in Medicine and Biology*, 47, 2002. p. 3985-3995.
4. Hannallah D, Zhu T.C., Bjärngard B.E. Electron disequilibrium in high-energy x-ray beams. *Medical Physics* 23, 1996. p. 1867-1871.
5. Johnsson S.A., Ceberg C.P., Knööös T., Nilsson P. Transmission measurements in air using the ESTRO mini-phantom. *Physics in Medicine and Biology* 44, 1999. p. 2445-2450.
6. Bjärngard B.E., Vadash P. Analysis of central-axis doses for high energy X rays. *Medical Physics* 22, 1995. p. 1191-1195.
7. Bjärngard B.E., Vadash P., Ceberg C.P. Quality control of measured Xray beam data. *Medical Physics* 24, 1997. p. 1441-1444.
8. BJR Suppl. 25. Central axis depth dose data for use in radiotherapy, *British Journal of Radiology*. London: British Institute of Radiology, 1996.
9. Hubbell J.H., Seltzer S.M. Tables of X-Ray Mass Attenuation Coefficients and Mass Energy-Absorption Coefficients from 1 keV to 20 MeV for Elements Z = 1 to 92 and 48 Additional Substances of Dosimetric Interest

BREAST TOMOSYNTHESIS – A NOVEL THREE-DIMENSIONAL X-RAY IMAGING TECHNIQUE

Pontus Timberg^a, Mark Ruschin^a, Tony Svahn^a, Ingvar Andersson^b, Bengt Hemdal^a, Sören Mattsson^a, Magnus Båth^c, and Anders Tingberg^a

^aDepartment of Medical Radiation Physics, Lund University, Malmö University Hospital, SE-205 02, Malmö, Sweden;

^bDepartment of Radiology, Lund University, Malmö University Hospital, SE-205 02, Malmö, Sweden; ^cDepartment of Medical Physics and Biomedical Engineering, Sahlgrenska University Hospital, SE-413 45, Göteborg, Sweden

Abstract

The sensitivity and specificity in 2D mammography is not perfect and could possibly be improved by a 3D technique that will overcome some of the limitations. These include overlapping anatomic structures that may mask a tumor or produce false densities, simulating tumors. The proposed technique is breast tomosynthesis (BT) in which low-dose images are acquired under rotation of the x-ray tube through a limited angle (50 degrees). These low-dose images are used to mathematically reconstruct a 3D volume image of the breast. The aim of this manuscript is to summarize three of our research projects and also to give an overview of our clinical findings of BT. Preliminary results have indicated a potential for an increase in cancer detection sensitivity by using BT compared to 2D mammography.

Keywords: Breast Tomosynthesis, Mammography

1. Introduction

Breast tomosynthesis (BT) is a three-dimensional (3D) x-ray imaging technique in which low-dose images are acquired under rotation of the x-ray tube through a limited angle. These low-dose images are used to mathematically reconstruct a 3D volume image of the breast, thus potentially increasing the visibility of lesions compared to the visibility in standard, two-dimensional mammography images. Our research projects consist of optimization of the BT system and to study the clinical benefits of this modality as to be implemented in screening programs.

A prototype, research BT system based on a Mammomat Novation (Siemens) full-field digital mammography system is installed at Malmö University Hospital. Ethical approval has been obtained to acquire images of selected patients undergoing mammography. There is also access to breast specimens and phantom materials for testing different image acquisition parameters, including number of low-dose image acquisitions, x-ray beam quality, detector-operating mode, and absorbed dose.

2. Aims and Methods

The aims of our projects include: developing phantoms and methods for evaluation of image quality; determination of the optimal combination of image acquisition and reconstruction parameters; determining the fundamental lesion detection limits for BT; and

clinical evaluation of BT with a limited number of cancer patients.

In the first study[1], a contrast-detail phantom was developed that contains spheres of different attenuation properties and sizes embedded in Polylyte[®], Fig. 1. Projection images were collected and an enhanced filtered back projection (FBP)[2] was applied to reconstruct the image volume of the phantom. The purpose of this phantom was to measure artifacts (in-plane artifacts [1]) introduced by the undersampled geometry and to quantify these effects on the images of the different spheres.

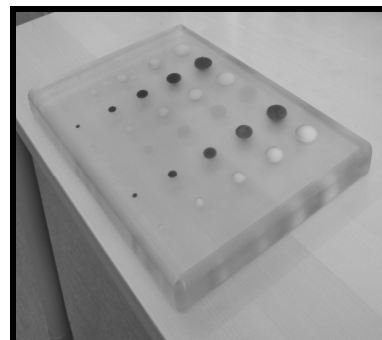


Fig. 1a. The contrast-detail phantom (210 mm × 300 mm × 26 mm) containing spheres of 6 different materials (diameters 4, 8, 12, 16, and 20 mm).

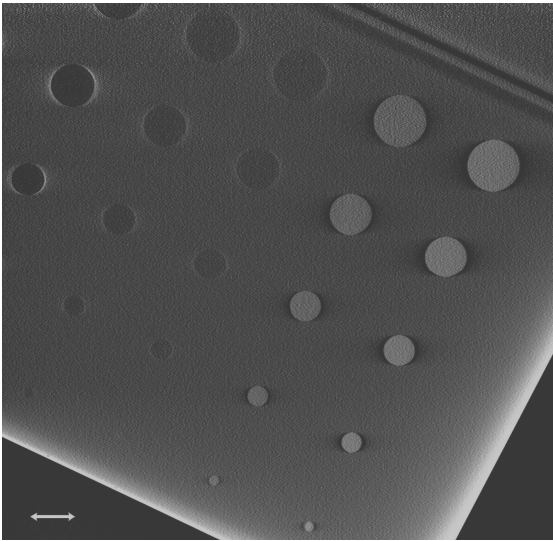


Fig. 1b. A reconstructed BT slice of the middle plane of the contrast-detail phantom. Notice the horizontal artifacts adjacent to the spheres.

In the second study [3], BT images of breast specimens containing malignant findings were collected at different acquisition modes and were visually graded by human observers in terms of artifacts, lesion visibility, sharpness of structures, noise and overall image quality, Fig. 2. The BT image acquisitions of the same specimens were performed varying the number of projections, angular range, and detector signal collection mode (binned and non-binned in the scan direction). The purpose was to determine image quality relative to optimal acquisition techniques of the unit. Reconstruction parameters were kept constant for this study.

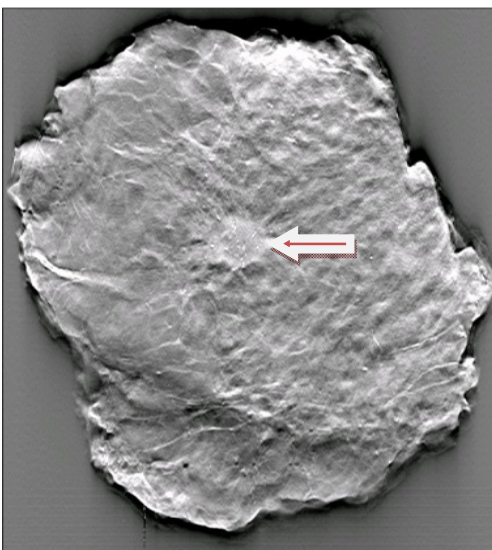


Fig. 2. Reconstructed BT slice of a breast specimen containing a malignant tumor.

In the third study[4], simulated ellipsoid-shaped tumors with irregular margins were projected and added

to each mammograms as well as each BT projection image prior to reconstruction, Fig. 3. The tumors were simulated so that the setup of shape, size and contrast of the objects could be controlled. A series of human four-alternative-forced-choice (4AFC) detection experiments were conducted to determine the fundamental lesion detection limits for BT compared to standard mammography.

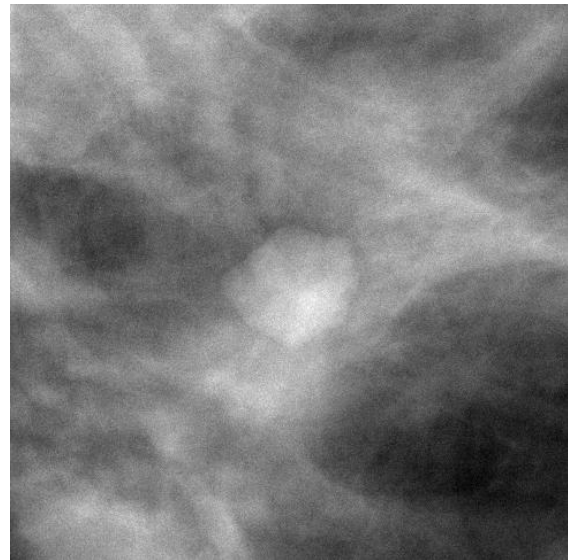


Fig. 3a. The image shows a simulated tumor inserted into a 2D mammogram.

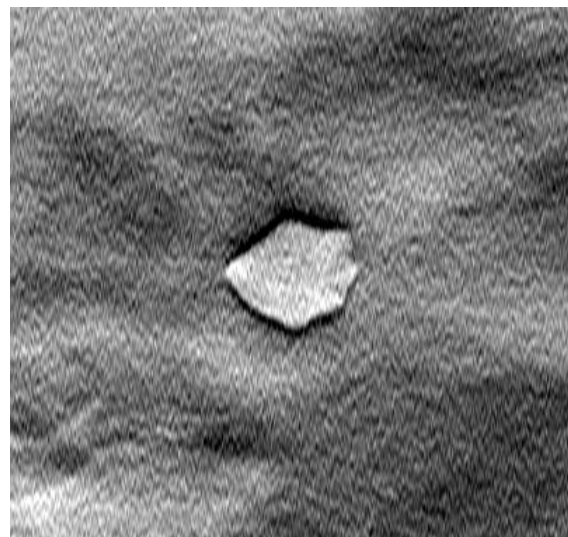


Fig. 3b. A reconstructed BT slice of the same tumor as in Fig. 3a. Notice the artifacts around the borders of the lesion that only appears in the scan direction.

Finally, clinical evaluations of BT with a limited number of cancer patients were performed, Fig. 4. Thirty BT examinations of verified malignant tumors were compared with ultrasonography and 2D mammography. Grading of visibility (not visible (0),

questionable visible (1), visible (2), clearly visible (3)) and classification (normal (1), benign lesion (2), low probability (<2%) of carcinoma (3), suspicious for carcinoma (4), clear carcinoma (5)) according to Breast Imaging Reporting and Data System (BIRADS) was performed for all imaging modalities.



Fig. 4a. A 2D mammogram of a fatty breast that appears to be normal.



Fig. 4b. A reconstructed BT slice of the same view of the breast as in Fig. 4a. Now a spiculated tumor becomes visible with rather high contrast. Histology shows a grade 1, 1.0 cm ductal carcinoma.

3. Results

A novel contrast-detail phantom for testing image quality in BT has been constructed. Optimization of

image acquisition parameters in BT has been performed using 31 breast specimens. The results of the study using simulated tumors indicate that tumors with four times lower contrast can be detected by using BT instead of standard mammography. Finally, our clinical findings (30 patients, 33 breast cancers) indicate an increase in tumor visibility and higher BIRADS classification of malignancies in BT images, Table 1 and 2.

Table 1. Visibility of 33 malignant lesions in 1-view mammography and 1-view BT.

DM	BT	n
Not visible	Visible/ Clearly visible	5
Questionably visible	Visible/ Clearly visible	17
Visible	Not visible	1
Equally visible		6
Not visible	Not visible	4

Table 2. BIRADS classification of 33 malignancies in 1-view DM and the same view BT

DM	BT	n
1, 2	3, 4, 5	9
3	4, 5	8
4	5	2
4	1	1
Equal		13

4. Conclusions

Preliminary results have indicated a potential for an increase in cancer detection sensitivity by using BT compared to mammography.

5. References

1. Svahn T., et al.. Inplane artifacts in breast tomosynthesis quantified with a novel contrast-detail phantom, Proc. SPIE 6510-173, 2007.
2. Mertelmeier T, Orman J, Haerer W, and Dudam MK. Optimizing filtered backprojection reconstruction for a breast tomosynthesis device, Proc. SPIE 6142, 131-142, 2006.
3. Timberg P, et al.. Optimization of image quality in breast tomosynthesis using lumpectomy and mastectomy specimens, Proc. SPIE 6510-110, 2007.
4. Ruschin M, et al.. Improved in-plane visibility of tumors using breast tomosynthesis, Proc. SPIE 6510-54, 2007.

THERMOSTIMULATED EXOELECTRON EMISSION OF CARBON DOPED Al_2O_3 : POTENTIAL APPLICATION FOR MICRODOSIMETRY

Yuri DEKHTYAR*, Alexei KATASHEV*, Sergei POPOV**, Nina ROZANOVA*

*Riga Technical University, Latvia

**Latvian Oncology Centre, Latvia

Abstract

Carbon - doped aluminum oxide is known as a material for dosimeters, operating on the base of optically stimulated luminescence. The present work explores thermally stimulated exoelectron emission of the γ - irradiated material. Because of extremely thin depth of electron escape (about 100 - 1000 Å), thermally stimulated electron exoemission may be used for small- volume dosimetry.

Keywords: dosimetry, thermostimulated exoelectron emission, aluminum oxide.

1. Introduction

Number of ionizing radiation dosimetry applications, such as verification of high gradient radiation fields in radiotherapy, requires dosimeters of relatively small effective size. Diamond solid-state chambers and film dosimeters, generally, provide required resolution. However, such types of dosimeters have certain breakdowns. Diamond detectors are expensive and require external power for operation. Films are single use devices, besides there are some problems for film use in vivo to measure dose within natural human cavities because of low resistance to humidity.

For the purpose of inter-cavity dosimetry, luminescence – based dosimeters may be used. However, these dosimeters usually have size of several millimeters to provide adequate TL signal, originated from the total volume of the dosimeter, therefore high spatial resolution is unreachable. To override this breakdown, one could use electron emission signal from the irradiated surface of the dosimeter. In such a case the depth from which electrons escape from the surface is about 100 – 1000 Å [1]. Therefore, electron emission signal provides information about very thin surface layer. This layer could serve as a dosimeter with effective size of electron escape depth in the direction towards the surface. Such a dosimeter may be applied to high gradient fields.

The present work comprises an attempt to validate the above idea with an example of carbon doped aluminum oxide (Al_2O_3 :C) that is widely in use as photostimulated luminescence dosimeter [2].

2. Materials and methods

Tablets of Al_2O_3 :C, sized 2 mm of thickness and 5 mm in diameter, were used. The tablets were annealed in vacuum at 450°C during 5 minutes.

After that the tablets were irradiated by 6-MeV photon beam using the medical linear accelerator Clinac 2100CD. Tablets were placed in a water equivalent PMMA phantom 10x10 cm with thickness 2 cm. The phantom was placed over 2.4 cm PMMA plate and covered by 0.5 cm water-equivalent bolus. The setup is shown at Fig.1. Irradiation was made at distance 100 cm between radiation source and phantom surface using photon beam field size 10x10 cm. Doses to tablets were evaluated using Varian treatment planning software, adjusted for the Clinac.

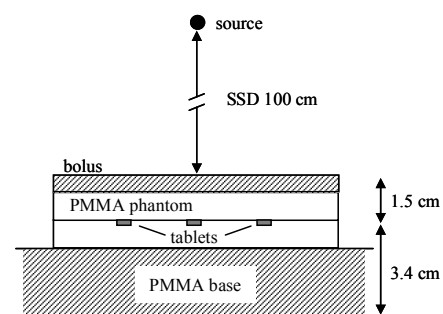


Fig. 1. Arrangement for irradiation of tablets

Photo-, thermo- and photothermostimulated electron emission signals from the surface of the tablets were measured in vacuum 10^{-5} Pa by means of home - made vacuum spectrometer [3]. Photoelectron emission (PE) current was induced by light from deuterium light source. A wavelength was selected by diffraction grating monochromator in the range 280 - 200 nm

(4.4 - 6.2 eV). To reach thermostimulated electron at heating rate 10°C/min. During heating, electron emission current was measured. For photothermostimulated emission (PTSE) detection, specimens were simultaneously heated and illuminated by light of constant wavelength.

Each specimen was measured several times by the same procedure: after initial annealing before irradiation; first time after irradiation and second time to ensure there was no residual thermally stimulated electron emission signal after annealing.

3. Results and discussion

Fig. 2 shows typical PE normalized spectra of non-irradiated, irradiated and annealed tablets. Comparison of spectra does not show any peculiarities for irradiated tablets. This means that the local states, possibly absorbed radiation induced electron, are not displayed by the spectra. There is a shift of the curves, indicating alteration of photoelectron work function of the specimens because of both annealing and radiation. However the observed shift cannot be considered as the significant one for the dosimetry purpose.

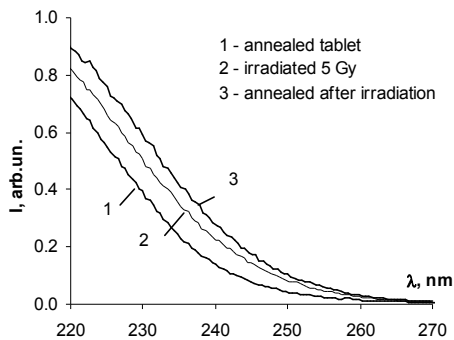


Fig. 2. Photoelectron emission spectra of Al₂O₃:C

TSE spectra of irradiated specimen (Fig. 3) demonstrate a clear peak at 320 °C. Peak does not exist at the spectra of both non-irradiated and annealed specimens. Therefore the appearance of peak is caused just by radiation.

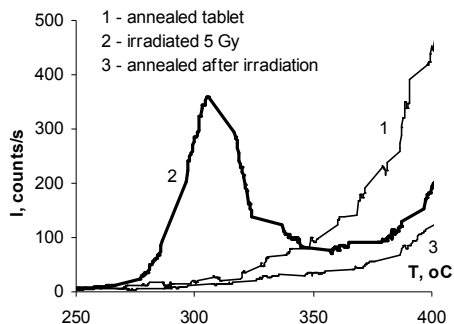


Fig. 3. Thermally stimulated electron emission spectra of Al₂O₃:C

Comparison of PTES spectra (Fig.4) with TSE ones demonstrates, that additional photostimulation does not induce any peaks

emission (TSE), specimens were annealed up to 450°C. Taking the above into account TSE signal is the most appropriate for dosimetry purposes.

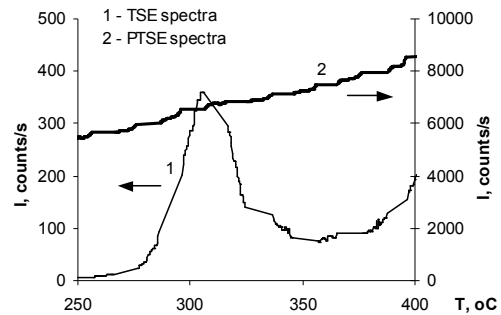


Fig. 4. PTSE of 5Gy irradiated Al₂O₃:C at wavelength 240 nm, compared with TE spectra of the same specimen.

Different tablets demonstrated different sensitivity of TSE to irradiation (Fig.5). Thus, to obtain dose dependence of TSE signal, each tablet has to be processed separately,

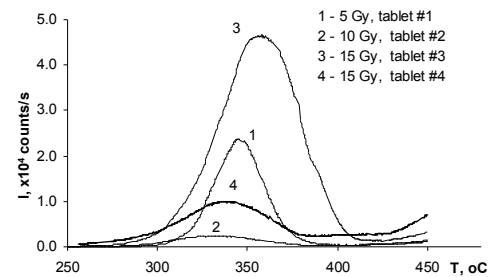


Fig. 5. Thermally stimulated electron emission spectra of different tablets of Al₂O₃:C.

4. Conclusions

Gamma irradiation of Al₂O₃:C tablets induce a clear TSE signal, that demonstrates possibility for dosimetry of the high gradient radiation fields. However, different tablets have different sensitivity of TSE signal to radiation dose. Thus, individual calibration of tablets will be required.

5. References

1. Introduction to radiation of physical chemistry of alkali halids. 1989, Riga, Zinatne, 244 p. (In Russian).
2. Akselrod M. S, Akselrod A. E. New Al₂O₃:C, Mg crystals for radiophotoluminescent dosimetry and optical imaging, Radiation Protection Dosimetry Advance Access, published online on April 10, 2006 Radiation Protection Dosimetry, doi:10.1093/rpd/nci663
3. Akmeņe R.J., Balodis A.J., Dekhtyar Yu. *et al.* Exoelectron emission spectrometer complete set of surface local investigation. Poverhnostj: fizika, khimija, mehanika 1993., N 8., 125.-128.

MICRO-RAMAN AND INFRARED SPECTRA OF BLOOD

Maksims POLAKOV^{*}, Nina MIRONOVA-ULMANE^{*}, M. GRUBE^{**} and E.REINHOLDS^{***}^{*}Institute of solid State Physics, University of Latvia, Riga, Latvia^{**} Institute of Microbiology and Biotechnology, University of Latvia, Riga, Latvia^{***} Nuclear Medicine Dep. P.Stradins Clinical University Hospital, Riga, Latvia**Abstract**

In the present work we report results of measurements of Raman scattering of hemoglobin and FT-IR spectroscopy for detection of radiation influence on serum of patients examined by radio-isotopes diagnosis (Tc99m). After radiation we observed of some little changes of the Raman scattering bands, which connected with out of plane porphyrine bending vibrations. It was shown that FT-IR spectra of blood indicate the radiation effects on serum.

Keywords: Raman scattering, FT-IR spectroscopy hemoglobin, blood

1. Introduction

Resonance Raman spectroscopy has long provided useful information electronic state of iron in haemoglobin (Hb) [1-6]. Resonance Raman scattering from Hb occurs only at its surrounding ligands group because only this part of the molecule absorbs in the visible and near ultraviolet region. Thus it is possible to investigate exclusively vibrations of the four heme groups (Fig.1) of Hb without interference by scattering of the surrounding globin or other parts of the RBC. The resonance Raman spectra of Hb provide information about the oxidation and spin state of the heme irons [1]

The ions of iron in the heme commonly occurs in one of two different electronic states in the haemoglobin ferric Fe^{3+} (methemoglobin) with electronic configuration $\text{Ar}(3d^5)$ and ferrous Fe^{2+} $\text{Ar}(3d^6)$ (haemoglobin). In the low-spin ferric state the porphyrin is more planar because the Fe ion translocates into the porphyrin plane. However, the movement of the Fe ion into the porphyrin plane can distort the macrocycle, further reducing this planarity and increasing nontotally symmetric components.

Each of these ions of iron can exist in two different spin states, which reflect the distribution of electrons within the d orbital - high-spin and low-spin configuration. Methemoglobin or (ferric form of hemoglobin) is the form of hemoglobin, which is oxidized to the 3+ ferric state. This form of hemoglobin is not able to bind oxygen This compound is unable to deliver oxygen to tissues; therefore, it is advantageous to convert this 3+ form of hemoglobin into the 2+ ferrous state so that tissues can get the oxygen that they need.

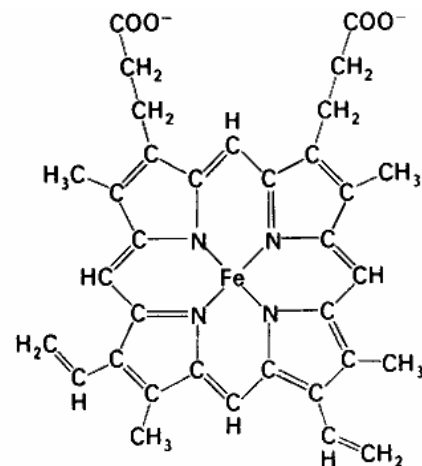


Fig.1. Structure of heme

The Raman bands are well known for several resonance excitation lines (488.0, 514.5, and 568.2 nm) [1-5].

The Raman spectrum strongly depends on the wavelength of the excitation [1-5]

The Raman scattering technique shows potential as diagnostic probe for a myriad of erythrocyte disorders including thalassemia, sickle cell anemia, altitude sickness, and met-Hb disorders. Moreover, the *in vivo* nature of the measurements implies that drug studies could be performed on diseased or impaired erythrocytes [3].

In the present study the Raman spectra of the erythrocytes were recorded on "Nanofinder-S" using the 441.6 nm excitation line The Raman excitation line used in 441.6 nm cause resonance enhancement with absorption band 415 nm.

2. Materials And Methods

Raman experiments were conducted at room temperature using 3D scanning confocal microscope (Fig.1) with spectrometer *Nanofinder-S* (SOLAR TII, Ltd.) and the He-Cd laser (441.6 nm, 70 mW cw power) as excitation source (Fig.2)



Fig. 2. "Nanofinder S" 3D Scanning Confocal microscope with Spectrometer

The laser power at the sample was regulating by the neutral filter (OD=0.5) to prevent sample heating. The measurements were performed through Nikon Plan Fluor 40x (NA=0.75) objective, mounted on inverted Nikon ECLIPSE TE2000-S optical microscope. The elastic component of laser light was eliminated by the edge filter.

The Raman spectra were recorded by a TE cooled back-thinned CCD camera (ProScan HS-101H) attached to the monochromator-spectrograph Model MS5004i (SOLAR TII, Ltd., focal length 520 mm, 600 grooves/mm grating, a resolution 0.16 nm). Frequency shifts in the Raman spectra were calibrated using CaWO₄ as a reference.

Venous blood was donated by consenting patients before and after radio-isotopes diagnosis and collected under air in glass tubes containing a small amount of heparin used as an anticoagulant.

FT-IR absorption spectra of serum samples were recorded on the HTS-XT micro plate reader (BRUKER). 10 μ l of sample were dropped on a 96 place silicon plate, dried at 50 °C and spectra registered in 500-4000 cm^{-1} region, absorption mode.

The spectra were baseline corrected (rubber band) and vector normalized. Data were processed by OPUS 6.0 integration mode "K"- vertical to the oblique line for a semi-quantitative evaluation of the radiation caused changes in cell.

3. Experimental results and discussion

3.1 Raman scattering spectra

The power of the Raman excitation laser 441.6 nm at the sample was regulating by the neutral filter

(OD=0.5) to prevent sample heating and damage of erythrocyte [7].

Observation and imaging of the erythrocyte was made by an external CCD camera connected with additional screen. (Fig. 3).

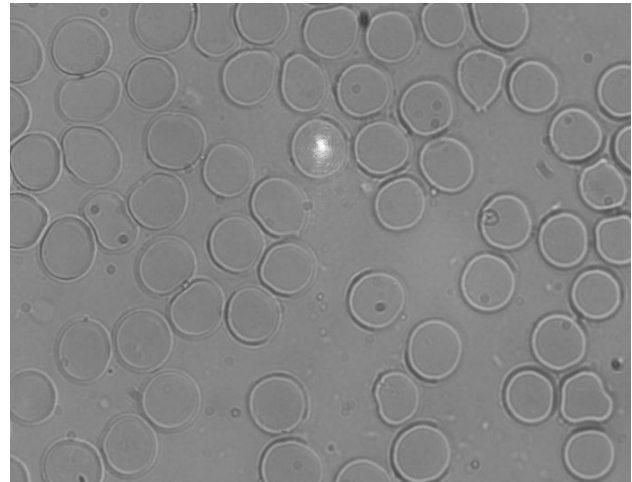


Fig. 3. Bright-field image of RBC taken by the CCD camera. With point of the laser Raman excitation beam.

Raman spectra of hemoglobin in erythrocyte using 441.6 nm excitation are shown in Fig. 4.

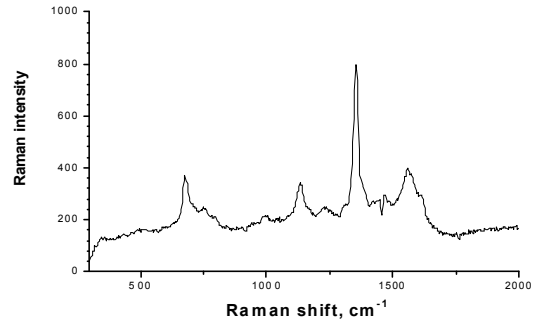


Fig. 4. Micro-Raman spectra of hemoglobin in erythrocyte recorded before radio-isotopes diagnosis

The Raman scattering spectra obtained for the 441.6 nm excitation wavelength applied here are in good agreement [1-5]. The strongest enhancement is usually observed when the excitation wavelength lies on (resonance) or near (pre-resonance) an electronic transition.

Table 1. Symmetry, local coordinates and location for Hb

Nr.	Sym.	Local coordinates	cm ⁻¹
1	A ₁	δ(deform)sym	676
2	B _{1g}	v(pyr breathing)	743
3	E _u	δ(pyr deform)asym	795
4	E _u	v(CbC1)asym	996
5	A _{2g}	v(pyr half-ring)asym	1136
6	B _{2g}	v(pyr half-ring)asym	1230
7	A _{1g}	δ(CmH)	1280
8	A _{2g}	δ(CmH)	-
9	E _u	v(pyr half-ring)sym	1300
10	A _{1g}	v(pyr half-ring)asym	1360
11	A _{2g}	v(pyr quarter-ring)	1450
12	B _{2g}	v(CaCm)sym	1550
13	B _{1g}	v(CbCb)	1558
14	E _u	v(CbCb)	1664
15	A _{2g}	n(CaCm)asym	1800

Raman spectra of hemoglobin in erythrocytes for patient after examined by radio-isotopes diagnosis (Tc99m) using 441.6 nm excitation are shown in Fig. 5

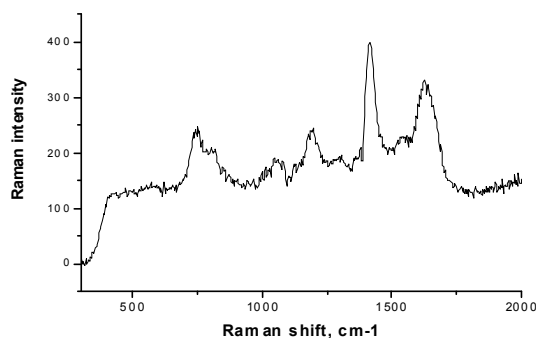


Fig. 5. Micro-Raman spectra of hemoglobin in erythrocyte recorded after radio-isotopes diagnosis

The Raman scattering spectra of patient after radio-isotopes diagnosis have changes detected in the high-frequency region.

The high-frequency region of the resonance Raman spectrum of hemoproteins contains a number of modes that are sensitive to the π-electron density of the heme. The most intense of them and little acted upon by other factors is the mode of symmetric stretching vibrations ν₄. For ferri-forms of hemoglobin (or methemoglobin) and also for liganded ferro-forms (a 6-coordinated heme), the frequency of the mode ν₄ is in the range 1370.-1380 cm.¹, whereas for desoxygenated (reduced) hemoglobin (a 5-coordinated heme), it is 1353.1358 cm.¹ [2]. The large difference in the frequency of the mode ν₄ for the liganded and deliganded forms of hemoglobin and their practically equal intensity make it possible to use it for detecting the liganding state of hemoproteins [2-3].

After radiation we observed of some little changes of the bands which connected with out of plane

porphyrine bending vibrations. Also we observed additional band near 1360 cm⁻¹ shoulder 1370 cm⁻¹. Radiation of blood lead to the transition from hemoglobin (Fe²⁺) to methemoglobin (Fe³⁺) with a delocalization of iron from porphyrine plane.

3.2. FT-IR spectroscopy

This was our first attempt to study the influence of radiation on cells by means of FT-IR spectroscopy. The absorption spectra of initial/control sample and after irradiation are shown in Fig.6.

The spectra are similar to usual bio-sample but it must be pointed out that absorption in “carbohydrate” region – 900-1200 cm⁻¹ is negligible. Comparison of serum spectra with published erythrocyte FT-IR spectra [8-9] are very similar and the main absorption regions are from stretching vibrations of C=O and bending vibrations of N-H and NH₂ in proteins and amino acids (1653 cm⁻¹); stretching vibrations of C=H, and asymmetric stretching vibrations CH₂ and CH₂ of fatty acids and cholesterol (2930 cm⁻¹); and stretching vibrations of P-O, P=O and C-O, of phospholipids and cholesterol (1119 cm⁻¹).

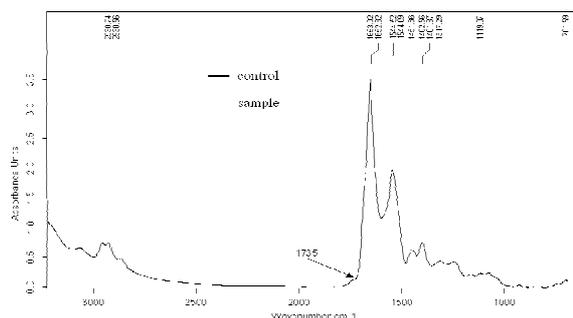


Fig.6. FT-IR absorption spectra of serum: 1- initial/control. 2- irradiated.

Evaluation of spectral profiles of the initial/control and treated sample spectra clearly shows changes in proteins: 1) the ratio of Amid I (1653 cm⁻¹) and Amid II (1544 cm⁻¹) is significantly higher in a control sample and 2) minimum between Amid II (1544 cm⁻¹) and Amid I is much less pronounced (higher) that can indicate the change of protein configuration – dominant of α or β sheet confirmations. Holman et al., (2000) in studies of human cell responses to chemicals showed that the protein Amide I peak centroid shifts down indicates a change in the overall protein conformational state within the cell.

A semi-quantitative integral-based method was used for demonstration of differences between the control and irradiated samples.

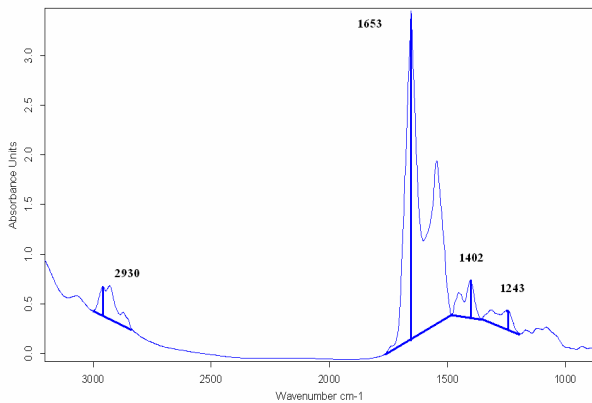


Fig.7. Integration absorption spectra of serum

Integration was used in four regions: 1) 1191-1359 cm^{-1} with maximum at 1243 cm^{-1} (phospholipids, and nucleic acids); 2) 1359-1481 cm^{-1} with maximum at 1402 cm^{-1} (stretching of COO⁻); 3) 1481-1780 cm^{-1} with maximum at 1653 cm^{-1} (Amid I); and 4) 2769-3005 cm^{-1} with maximum at 2930 cm^{-1} (fatty acids).

The integral meanings of those bands are shown in Table 2.

Table 2. Integrals of the principal absorption bands in the FT-IR spectra of serum

Absorption bands	Initial/control sample	After radiation
1243 cm^{-1}	0.005	0.005
Amid I - 1653 cm^{-1}	0.107	0.055
1402 cm^{-1}	0.012	0.016
Fatty acids -2930 cm^{-1}	0.011	0.014

Evaluation of spectra after baseline correction and normalization showed that the absorption in phosphate and nucleic acid region 1191-1359 with maximum at 1243 cm^{-1} is equal in both serum samples and thus can be used as internal standards for evaluation of quantitative changes caused by irradiation. The ratio of integrals: Amid I/1243; 1402/1243 and 2930/1243 showed well pronounced differences in both samples not only in proteins and amino acids but fatty acids as well. (Fig. 7) It can be seen that irradiation causes the decrease of protein content in cells but the fatty acid content increases that can be an indication of the cell response to the stress.

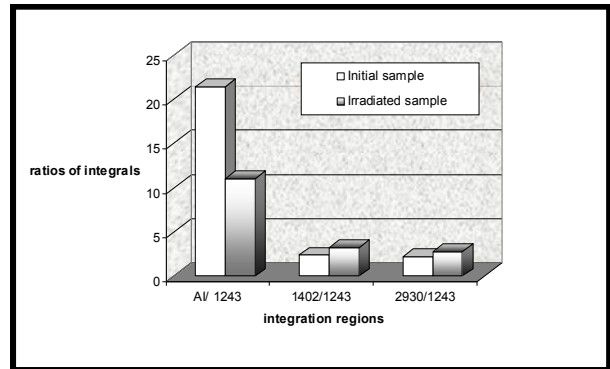


Fig.7. Semi-quantitative analysis of initial/control and irradiated serum samples

4. Conclusions

After radiation we observed of some little changes of the Raman scattering bands, which connected with out of plane porphyrine bending vibrations. Also we observed additional band near 1360 cm^{-1} shoulder 1370 cm^{-1} and increase intensity of band 1664 cm^{-1} . Radiation of blood lead to the transition from oxyhemoglobin (Fe²⁺) to methemoglobin (Fe³⁺) with a delocalization of iron from porphyrine plane.

It was shown that FT-IR spectra indicate the radiation effects on serum. Taking into account that FT-IR spectroscopy is a quick and highly informative method that needs small amounts of sample (in our case even few micro liters) and when using micro plate reader even no sample pretreatment is necessary it is very promising for studies of irradiation effects on blood cells.

This study could be continued applying priorities of infrared micro spectroscopy that hopefully can speed up the evaluation of influence of irradiation and other environmental effects on single erythrocyte cells.

Acknowledgements

This work was supported by the Latvian Government grants (No. 05.1718), Latvian National Research Program in Materials Science

5. References

1. K.Ramser, K. Logg Goksör J. Enger, M. Käll, D. Hanstorp Resonance Raman spectroscopy of optically trapped functional erythrocytes Journal of Biomedical Optics 9(3), 593–600 (May/June 2004)
2. B. R. Wood, B. Tait, and D. McNaughton, Micro-Raman Characterization of High- and Low-Spin Heme Moieties within Single Living Erythrocytes *Biochim. Biophys. Acta* 1539, 58–70 2001.
3. B. R. Wood, S. J. Langford, B. M. Cooke, F. K. Glenister, J. Lim and D. McNaughton, Raman

4. imaging of hemozoin within the food vacuole of *Plasmodium falciparum* trophozoites FEBS Letters 554 (2003) 247-252
5. B. R. Wood and D. McNaughton, "Micro-Raman characterization of high- and low-spin heme moieties within single living erythrocytes, *Biopolymers* **67**, 259-262, 2002
6. B. R. Wood and D. McNaughton, "Raman excitation wavelengths investigations of single red blood cells *in vivo*," *J. Raman Spectrosc.* 517-523 ~2002
7. C. W. Ong, Z. X. Shen, U. A. Ang, U. A. Kara, and S. H. Tang, "Resonance Raman microspectroscopy of normal erythrocytes and *Plasmodium berghei*-infected erythrocytes," *Appl. Spectrosc.* 53, 1097-1101 ~1999.
8. G. J. Puppels, J. H. F. Olminkhof, G. M. J. Segers-Nolten, C. Otto, F. F. M. DeMul, and J. Greve, "Laser irradiation and Raman spectroscopy of single living cells and chromosomes: sample degradation occurs with 514.5 nm but not with 660 nm laser light," *Exp. Cell Res.* 195, 361-367 1991.
9. C. Petibois, G. Deleris (2004) Oxidative stress effects on erythrocytes determined by FT-IR spectrometry, *Analyst*, 129, 912-916.
10. H-Y.N. Holman, R. Goth-Goldstein, E.A. Blakely, K. Bjomstad, M. C. Martin and W.R. McKinney (2000) Individual human cell responses to low doses of chemicals studied by synchrotron infrared spectromicroscopy, In: *Biomedical Spectroscopy: Vibrational spectroscopy and other novel techniques*; A. Mahadevan-Janen, G.J.Puppels, eds., *Proceedings of SPIE*, 57-63.

ESTIMATION OF INTERNAL AND EXTERNAL EXPOSITION IN RETROSPECTIVE DOSIMETRY OF CHERNOBYL CLEAN-UP WORKERS

Nina MIRONOVA-ULMANE*, Maksims POLAKOVS*, Andrejs PAVLENKO*, Daina PIEKSTINA*
Tija ZVAGULE**, Elvira CHURBAKOVA**, Natalija KURJANE**, Natalija GABRUSHEVA**,
Maja EGLITE***, Tiit KÄRNER****

*Institute of Solid State Physics, University of Latvia, Riga, Latvia

** Centre of Occupational and Radiological Medicine of P.Stradins Clinical University Hospital, Latvia

***Institute of Occupational and Environmental Health of Medical Academy of Latvia

****Institute of Physics, University of Tartu, Riia street 142, EE-2400 Tartu, Estonia

Abstract

Individual dose reconstruction by Electron Paramagnetic Resonance (EPR) has been performed for group of Latvian inhabitants participated in Chernobyl reactor accident clean-up activities. The total EPR dose including exposure from internal/external beta and gamma radiations was significantly higher, when officially documented dose.

Keywords: Retrospective dosimetry, Teeth enamel, internal/external exposure

1. Introduction

The explosion at the Chernobyl Nuclear Power Plant occurred more than 20 years ago resulted in unpredicted release of radiation caused adverse health effects both on clean-up workers and general public. The first group represents around 600,000 people participated in recovery operations after accident having high level of radiation exposure. There are huge number of publication devoted to monitoring of health impact to European population [1,2] analysis of radionuclide distribution and its transfer in the environment [2,3] estimation of absorbed doses to personal taking part in mitigating of accident [4-6].

At the moment it is very well investigated topic demonstrating decreasing of public and scientific interest all over the world. However, for Republic of Belarus, Russian Federation and Ukraine and parts of some European countries is still subject of great consequence because of the impact on environment and on human resources caused by this accident. For instance, there are around 5000 Latvian inhabitants or 0.35% of all population took part in clean-up activities from 1986 till 1991. Nowadays they present a group of chronically sick people that requires further observation, examination and scientific investigation as well as proper treatment and rehabilitation. The individual doses obtained from their military passports were in order 1-500 mGy that according to [7] represent highly uncertain radiological issue lacking description of dosimetry method, location of work and activities performed. In the best case the officially documented doses reflected only external exposure from photon radiation and sometimes were approximated for group of workers performing the same type of activities.

The individual dose reconstruction by EPR method has been performed for group of Chernobyl accident clean-up workers indicating underestimation of official doses by factor 2-5 [7-9]. The main factor of discrepancy is continuous irradiation of internally incorporated nuclides mainly ^{90}Sr distributed through the calcified tissues. ^{90}Sr has long physical (29.1 years) and biological (aprox. 5 years individually dependent) half life and continues to irradiate human organism in many years after intake. Therefore contribution to the total EPR dose from this factor is could increase with time.

This paper is focused on estimation of internal and external exposure in retrospective dosimetry.

2. Materials and methods

Latvian inhabitants taking part in mitigating activities after the Chernobyl accident is an unique cohort for scientific studies because they had radiation exposure during an exact period of time and then had been moved to not-contaminated region. The 1320 workers worked close to the reactor and turbine hall, 1130 worked at the installations next to the reactor site, 2213 worked at general environment. These workers were mainly at the age 18-45 at the time of work in Chernobyl (Table 1). People employed between 1986 and 1987 worked 1 to 3 months in average, while those employed later worked for 4 to 6 months in average. The workers employed in 1988 to 1989 were mainly occupied with building of town near the Chernobyl reactor and did not involved in the works on the site of reactor itself, therefore their doses are lower than doses of earlier clean-up workers.

Table 1. Distribution of Chernobyl NPP accident clean-up workers by age and time of work in Chernobyl

Age Year	<18	18-20	21-25	26-30	31-35	36-40	41-45	>45
1986	5	122	712	635	540	387	191	46
1987	2	30	257	347	382	238	74	40
1988	0	2	6	57	227	163	60	9
1989	0	2	4	8	45	47	11	4
1990	0	0	0	0	3	2	2	0
>1990	0	0	0	0	0	0	3	1
Total	7	156	979	1047	1196	837	341	100

Around 70% of the cohort has officially documented exposure records ranging from 0.01 to 0.5 Gy. As was indicated in records 43% received zero dose and 26% absorb dose equal to the normal background radiation in unaffected areas. In reality the dose was not monitored individually but was taken averaging dose rate values from photon radiation.

Electron Spin Resonance

ESR retrospective dosimetry is based on measurements of amount of radiation induced radicals in hydroxyapatite (HAP) $\text{Ca}_{10}(\text{PO}_4)_2(\text{OH})$, which present in mineralized tissues like tooth enamel, dentine and bone. Tooth enamel is more suitable for ESR measurements taking into account high HAP content, slow metabolism and high sensitivity to ionising radiation.

The majority of radiation-induced radicals in tooth enamel are originated in carbonate impurities in HAP, i.e. CO_2^- , CO_3^- , CO^- , CO_3^{3-} , but also radicals derived from phosphate, PO_4^{2-} , and oxygen, O^- and O^{3-} were identified.

The lifetime of the most stable radicals contributing to the asymmetric EPR signal was estimated as 10^7 years. However, thermally unstable radicals are also contributing to the EPR signal. Following irradiation, the CO_3^- signal amplitude gradually increases reaching a stable state after about 4 weeks [10].

Caries, fluorination and metabolism of enamel have superlative contribution to the ESR signal intensity [10]. For instance, they intensively contribute to background ESR signals in teeth enamel ($H = 0.9-1.0$ mT, $g = 2.005$). The origin of these signals is not exactly established, but it essentially limits a threshold of ESR dosimetry with tooth enamel. The signals are specific for every sample and usually attributed to the organic component of enamel [11]. However, another author indicated CO^- radical located on HAP surface as possible source of the background ESR signal [12]. In spite of some difference in details the structure and parameters of background signals are very close. Investigation of synthetic apatite with different concentration of carbonate allows connecting the background signals with presence of the other impurity carbonate phases in HAP. This postulate was also confirmed by X-ray diffraction. Impurity carbonate phases synthesis is connected with pH in solution,

which leads to the individual variation of the radiation sensitivity of enamel.

For the given studies surgically extracted teeth mostly molars and pre-molars affected by caries have been selected for measurements. The crown was mechanically separated from the root. The dentine was removed with a hard alloy dental drill keeping enamel as the most suitable for ESR measurements. The enamel was crushed into coarse chips using an agate mortar and pestle. The teeth mostly molars and pre-molars affected by caries have been removed by dentists during routine dental examinations. The samples were kept in alcohol-ethyl mixture for several days for degreasing and dried for several weeks in exsiccator with annealed selicogel. Following such processing, the mechanically induced radicals decayed and the amplitude of the background signal was reduced.

ESR experiments on teeth enamel have been made at room temperature by an X-band cavity PE-1306 spectrometer. The measurements were compared to the standard samples MgO crystals doped with Mn^{2+} or Cr^{3+} . The spectra were recorded at microwave power 6.2 mW, applying magnetic field modulation of 100 kHz and amplitude 1 mT. One spectrum is obtained averaging 30 scans with receiver time constant 25 ms. For dose calculation the peak-to-peak amplitude of EPR signal located close to $g = 2,005$ has been used.

Two types of radioactive sources were used for sample irradiation: a ^{137}Cs gamma ray source with energy 0.6662 MeV, and a ^{90}Sr - ^{90}Y beta particles source with maximum energies 0.546 MeV and 2.28 MeV respectively. Five measurements, one initial and four after cumulative irradiation, were used to achieve linear fit in steps of 500 mGy. The dose was reconstructed by additive dose method [13-14].

The measurements of ^{90}Sr contents in tooth tissues were made using the standard radiometric method by low-level beta spectrometer at Latvian Nuclear Research Center. The powdered teeth enamel samples were placed close to the detector and measured two times with and without Al filter minimizing self absorption of beta particles. The readings of the device were compared with the measurements of the ^{90}Sr / ^{90}Y standard source with maximum energies 0.546 MeV and 2.28 MeV respectively. Applying the Al filter the low energy particles from ^{90}Sr has been absorbed and only from ^{90}Y detected. The overall uncertainty of enamel activity measurements was in the range 10-15%.

3. Results

The teeth enamel doses measured by EPR were in the range 60-450 mGy, which are much higher than officially documented doses (Fig.1). The EPR doses represent complete individual exposure included external and internal exposure during clean-up activities, exposure from medical examinations, background irradiation and etc. The interpretation of the obtained results is rather complicated and ambiguous. High data scattering may be caused by

differences of professional occupation and high heterogeneity of radiation contamination within the group of individuals. It was found that results of dose rate measurements after accident are varied by factor up to 20 (if dose documented) in different points of the same location [15].

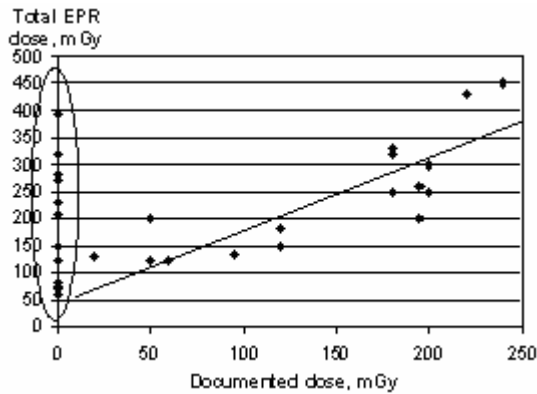


Fig.1 Relationship of EPR reconstructed dose and officially documented

The internal component of total EPR dose has been verified by activity concentration measurements on teeth enamel. The radioactivity of the teeth was measured in the low-background equipment, placing above the sample the Al filter that fully absorbs beta-particles from ⁹⁰Sr, but partly - from ⁹⁰Y. Hence we avoid the error caused by the self-absorption of ⁹⁰Sr low energy beta particles in the investigated sample. The radioactive standard of ⁹⁰Sr-⁹⁰Y was measured in the same way. The results demonstrated correlation between external and internal exposure for one part of liquidators. The other part having no records on external exposure had significant dose from internally incorporated nuclides.

Activity of ⁹⁰Sr measured on tooth enamel in 1997 for Chernobyl clean-up workers ranges from 0 Bq/g to 350 Bq/g (Table 2)

The dose rate in Gy/day is estimated by empirical formula [16]

$$P(t) = C_0 \cdot 1.38 \cdot 10^{-5} \cdot E_{\beta} \cdot k \quad (1)$$

where C_0 - specific activity of the teeth enamel (Bq/g); E_{β} - average energy of β - emitted ⁹⁰Sr/⁹⁰Y, 1.09 MeV; k - part of β -radiation energy absorbed directly in the teeth enamel, 0.9.

Using the formula (1) the absorbed dose rate to the teeth estimated for Chernobyl's clean-up workers ranging from 0.27 mGy/day to 4.7 mGy/day.

In the previous studies [6] the content of microelements and macro element calcium in the Chernobyl clean-up worker teeth in comparison with practically healthy man teeth, obtained from dentist has been measured. It was found presence of strontium (40-250 μ g/g), thorium (0-200 μ g/g) in clean up workers teeth. In teeth

of healthy individuals these elements have not been detected.

Table 2 Officially Documented Dose for Clean-up Workers and Specific Activity of ⁹⁰Sr Measured on Teeth Enamel

Number of Clean-up workers	Documented dose, mGy	⁹⁰ Sr, Bq/g
1	0.24	40
2	0.18	90
3	0	80
4	0	70
5	0.22	30
6	0	140
7	0.13	60
8	0	10
9	0.0427	110
10	0.195	60
11	0.02	80
12	0.15	0
13	0	60
14	0.13	20
15	0.09368	70
16	0.1582	110
17	0	10
18	0.06	90
19	0.2058	30
20	0.177	20
21	0	10
22	0	150
23	0.2011	20
24	0.211	0
25	0.089	0
26	0.211	350

The presented data are in line with results published by [15] where the same dose values from internal irradiation have been reported. Doses estimated from incorporated ⁹⁰Sr are highly varied from 0 to 240 mGy. It is connected with variety of factors on the workplace, kind of work, protective measures, time spend for clean-up activities and etc.

Table 3. Content of microelements - Ba, Sr, Zn,Co, (mkg/g) in the human tooth and macroelment Ca (%)

No of workers	Ba	Sr	Zn	Co x 0.001	Ca (%)
# 8	20	250	176	660	25.3
#15	20	160	197	210	26.7
#16	20	230	145	140	28.3
#17	20	220	166	210	22.4
#22	20	240	247	180	27.3
#23	30	220	199	880	30.1
#24	20	40	9360	450	25.4
#25	50	40	1690	460	33.4
#26	30	40	212	160	30.8
#27	30	170	183	1420	23.9
control	20	40	280	230	34.0
enamel ^a	-	70 -100	173 -250	6 - 1100	25 -28
dentine	4.2 - 12.5	80 -110	200 -366	4 - 1300	36 -37

Calcium content in clean-up workers teeth varied from 25% to 33% compare to 36% in healthy individual (Table.3)

4. Summary and Conclusions

Individual dose reconstruction by Electron Paramagnetic Resonance (EPR) has been performed for group of Latvian inhabitants participated at Chernobyl reactor accident clean-up activities. The total EPR dose including exposure from internal/external beta and gamma radiations was significantly higher, when officially documented dose where only external gamma exposure was registered. The internal component of total EPR dose has been verified by activity concentration measurements on teeth enamel. The radioactivity of the teeth was measured in the low-background equipment, placing above the sample the Al filter that fully absorbs beta- particles from ⁹⁰Sr, but partly - from ⁹⁰Y. Hence we avoid the error caused by the self-absorption of ⁹⁰Sr low energy beta particles in the investigated sample. The radioactive standard of ⁹⁰Sr-⁹⁰Y was measured in the same way. The results demonstrated correlation between external and internal exposure for one part of liquidators. The other part having no records on external exposure had significant dose from internally incorporated nuclides.

ACKNOWLEDGMENT

This work has been supported by research grant N 05-1718 by Latvian Council of Sciences and Latvian National Research Program in Materials Science.

6. References

1. World Health Organization. International Programme on the Health Effects of the Chernobyl Accident. Health consequences of the Chernobyl

- accident: results of the IPHECA pilot projects and related national programmes: Scientific report. ISBN: 5-88429-0 (1996)
2. International Atomic Energy Agency. Testing of Environmental Transfer Models Using Chernobyl Fallout from the Iput River, Catchment Area, Bryansk Region, Russian Federation. ISBN 92-0-104003-2. (2003)
3. International Atomic Energy Agency. Present and Future Environmental Impact of the Chernobyl Accident. IAEA TECDOC Series No. 1240. (2001)
4. United Nations Scientific Committee on the Effects of Atomic Radiation UNSCEAR 2000 Report to the General Assembly. Sources and Effects of Ionizing Radiation. Annex J: Exposures and effects of the Chernobyl accident. p.453-551
5. Degteva M. O., Vorobiova M. I., Tolstykh E. I., Shagina N. B., Shishkina E. A., Anspaugh L. R., Napier B. A., Bougrov N. G. and Tokareva E. E. Development of an Improved Dose Reconstruction System for the Techa River Population Affected by the Operation of the Mayak Production Association. Radiation Research 166, 255–270 (2006)
6. Mokrov, Y., Glagolenko, Y., Napier B. Reconstruction of radionuclide contamination of the Techa river cause by liquid waste discharge from radiochemical production at the Mayak Production Association. Health Physics 79:15-236; 2000
7. Mironova-Ulmane N, Pavlenko A, Eglite M., Curbakova E., Zvagule T. and Kurjane N. (2005) Chernobyl clean-up workers: 17 years of follow-up in Latvia. Recent Advances in Multidisciplinary Applied Physics, pp.9-19, Elsevier 2005 (ISBN 0 08 0444 696-5)
8. Chumak V, Bakhanova E, Musijachenko N et al. (2000) Dosimetric monitoring at time of Chernobyl clean-up. A retrospective view, IRPA-10 Proc. Vol. 1, International congress of the IRPA on harmonization of radiation, human life and the ecosystem, Tokyo, Japan, 2000, p.8
9. Mironova-Ulmane N, Pavlenko A, Zvagule T T., Kärner, T., Bruvere, R. and Volarte, A. et al. (2001) Retrospective dosimetry for Latvian workers at Chernobyl. Radiat. Prot. Dosim. 96:237-240
10. International Atomic Energy Agency. Use of Electron Paramagnetic Resonance Dosimetry With Tooth Enamel for Retrospective Dose Assessment. IAEA-TECDOC-1331. (2002)
11. Ivannikov, A.I., Skvortsov, V.G., Stepanenko, V.F., Tsyb, A.F., Khamidova, L.G. and Tikunov, D.D. Tooth enamel ESR dosimetry: sources of errors and their correction. Appl. Radiat. Isot. 52(5) 1291-1296 (2000)
12. Wieser, A. Comparison of sample preparation and signal evaluation methods for EPR analysis of tooth enamel. Appl. Radiat. Isot. 52(5) 1059-1064 (2000)
13. Mironova, N., Eglite, M., Churbakova, E., Zvagule, T., Riekstina, D. Electron spin resonance and instrumental neutron activation analyses of

- Chernobyl nuclear power plant accident clean-up worker teeth. Proc. Latvian Acad. of Science. **52** 194-196 (1998)
14. Zvagule T., Mironova-Ulmane N., Pavlenko A., Karner T, Bruvere R., Garbuseva N., and Volrate A.. Retrospective Dosimetry and Clinical Follow-up program for Chernobyl Accident Clean-up workers in Latvia. Proc. of the IRPA Regional Congress on Radiation Protection in Central Europe, Dubrovnik, Croatia, May 20-25 2001. CD-ROM 6o-03 (1-6) (ISBN 953-96133-3-7)
 15. Fesenko S.V., Alexakhin R. M., Geraski, S. A., Sanzharova N. I., Spirin Ye.V., Spiridonov S. I., Gontarenkoa, I.A. and Strand P. (2005) Comparative radiation impact on biota and man in the area affected by the accident at the Chernobyl nuclear power plant. J. Envir. Radiat. 80:1–25
 16. Ilin N, Borisova V, Vetluh V (1991) The remote biological effects of the combined action radionuclides. Energoatomizdat, Moskow (in Russian)

THE RADIATION ENVIRONMENT IN BRYANSK VILLAGES, 20 YEARS AFTER CHERNOBYL

Christian BERNHARDSSON^a, Maria CHRISTIANSSON^a, Irina ZVONOVA^b, Tanya JESKO^b,
Slava GOLIKOV^b, Christopher RÄÄF^a, Charlotte THORNBERG^a, Sören MATTSSON^a

^aDepartment of Medical Radiation Physics, Lund University, Malmö University Hospital, SE-205 02, Malmö, Sweden;

^bResearch Institute of Radiation Hygiene, ul. Mira, 8, RU-197101, St.Petersburg, Russia

Abstract

Since 1990 the radiation exposure of the population in some rural villages in the western Bryansk area, Russia has been measured regularly. The external contribution to the radiation effective dose to individuals has been estimated through measurements using individual TL-dosimeters. The contribution to the effective dose from internal ¹³⁷Cs contamination was estimated through whole body measurements. In 2006, twenty years after Chernobyl, the average yearly effective dose contribution from exposure to ¹³⁷Cs of the inhabitants in the villages studied (¹³⁷Cs soil contamination in 1986 was 0.9-2.7 MBq/m²) is in the order of 0.5 mSv. This is similar to the contribution from cosmic radiation and radiation from naturally occurring radionuclides (mainly ⁴⁰K) in the human body.

The initial fast reduction of the external irradiation in the beginning of the measurement series has now leveled off. There are still large variations in the ¹³⁷Cs content of the individuals and thus in the contribution to the effective dose from internal contamination. This may be explained by the highly inhomogeneous contamination level and different attitudes to dietary advices.

Keywords: Cesium-137, Chernobyl, Bryansk, effective dose, population

1. Introduction

In 1990 a joint Nordic-Russian program was initiated in order to carry out estimates of the effective dose to selected groups of inhabitants in a number of rural settlements in the western part of the Bryansk region in Russia. The region was one of the most contaminated areas (0.9 – 2.7 MBq/m² of ¹³⁷Cs) outside the 30 km zone following the Chernobyl disaster in 1986.

The aim of the present paper is to summarise the current radiation exposure of individuals living in these rural settlements and compare it with the results from previous years.

2. Methods

Expeditions have been carried out in September-October each year from 1990 to 1998 [1,2], and in 2000 [3] and have included individual dose assessments from external and internal irradiation to various individuals in a number of settlements. These settlements are all located within a 40 km radius from the regional center Novozibkov, in the Bryansk region close to the Ukrainian border around 200 km from Chernobyl.

A new expedition was carried out in September 2006 to follow up the long-term trend using methods resembling the previous expeditions.

Effective dose from external irradiation. TL dosimeters were handed out to the investigated inhabitants in September and carried by the participants during 1.5 to 3 months. The TL-chips consisted of square hot pressed/extruded LiF:Mg,Ti [Harshaw TLD-100] with dimensions 3.2 x 3.2 x 0.9 mm³. The chips were stored in a lead container and inserted, the night before distribution, in holders of PMMA with two chips in each. The same holders were used as in the earlier studies 1991 – 2000. In each of the villages Demenka, Starye Boboviche, Starye Vyshkov and Yalovka, 16 – 24 dosimeters were distributed to young and adult persons (6 – 79 yrs.) of both sexes.

At the end of the measurement period, the dosimeters were collected by a local contact person and sent to Sweden via St. Petersburg to be read-out using a TL-reader (Toledo Pitman Ltd). Three calibrations, free-in air in a ⁶⁰Co-beam at normal incidence, were performed, one just before the expedition and another two after the read-out.

The effective dose, E , was estimated by the following expression (Eq.1):

$$E = D_{\text{surface}} \cdot (D_{\text{surface}}/K_{\text{air}}) \cdot (E/K_{\text{air}}) \quad (1)$$

where D_{surface} is the absorbed dose to the body surface, i.e. the absorbed dose to the TL-dosimeters. The air kerma factor $K_{\text{air}}/D_{\text{surface}} = 1.11 \text{ Gy/Gy}$ for adults (> 15 yrs.) [4]. Monte Carlo simulations have indicated that

the E/K_{air} ratio is 0.83 Sv/Gy [5]. For children (< 15 yrs.) the effective dose was calculated by multiplying the body surface dose with 0.95 Sv/Gy [6]. The product of these terms (i.e. E/D_{surface}) has been experimentally verified by Thornberg *et al.* [2].

The background dose to the dosimeters is composed of several components. The most significant one is the absorbed dose accumulated during storage in Russia. The dose increment to the dosimeters when stored inside the lead container was estimated with background dosimeters stationary in the container and the dosimeter reading converted to effective dose according to Eq. 1. To determine the total background dose from transportation and during the time the dosimeters were stored outside the lead container, ambient survey measurements were performed with a SRV2000 [RADOS, Finland] and a GR-100 [Exploranium, Canada] ambient survey instrument.

To be able to subtract the dose contribution associated with the normal, “pre-Chernobyl” background (cosmic and natural terrestrial radiation) a dose rate of 45 μSv per month was used [7]. The net contribution from the Chernobyl fall-out was then multiplied by 0.94 to account for the shielding effect from snow during winter [2].

Effective dose from internal irradiation. Body burden of caesium. In each village the inhabitants were offered to get their total body burden of ^{137}Cs measured. The *in vivo* measurements were conducted in school buildings with thick walls of bricks (> 50 cm) or, as in Demenka, in a similar public building. The buildings allowed measurements with two portable (63 mm (\varnothing) \times 63 mm) NaI(Tl) detectors coupled to a multi channel analyzer (DigiDart, EG&G Ortec, USA). The subjects were sitting with the detectors in their knees pointing towards the abdomen (Palmer geometry) and individual calibration factors were used [8]. The background count rate was measured and a correction for the shielding by the measured person was carried out.

In total there were 317 participants of both sexes and ages ranging from 2 to 80 years during the last survey. For calculation of the effective dose from internal contamination of ^{137}Cs , the investigated subjects were divided in groups depending on age and weight according to ICRP 67 [9]. The annual effective dose, E , was then calculated according to Eq. 2 below [10].

$$E = r(m) \cdot A/m \quad \text{Eq. 2}$$

where $r(m)$ is the dose rate coefficient ($\text{mSv} \cdot \text{kg} \cdot \text{kBq}^{-1} \cdot \text{y}^{-1}$) for ^{137}Cs in a human subject with body mass m and A is the activity concentration of ^{137}Cs in the body.

Urine samples. The 12 individuals that had the highest levels of ^{137}Cs from the *in vivo* measurement were asked to give a single urine sample. The samples were collected in glass jars and transferred to 45 ml test tubes. The analysis of the urine was carried out at the Malmö University Hospital, within a few weeks after collection using a (66.2 mm (\varnothing) \times 73.4 mm) HPGe detector with a relative efficiency of 55%.

3. Results

External- and internal contributions to the effective dose. After the dosimeters were used they were stored in schools or other public buildings with thick walls and hence the dose rate was relatively low, about 0.10 $\mu\text{Sv}/\text{h}$. The other component of the background dose that was accumulated during air transport D_f was estimated to be 4 μSv from measurements *in situ*. The measured absorbed dose to the background dosimeters E_b varied between 172 and 177 μSv . This represents on average half of the total effective dose ($E_{\text{mean}} = 300 \mu\text{Sv}$) to the collected dosimeters (including the background radiation).

In Table 1, the dose rates in the villages as measured with TL-dosimeters are presented. The mean individual effective dose in the four villages ranged from 5 – 57 μSv per month, with a coefficient of variation (C_v) of 62 %. On average, the effective dose is decreasing, but there are deviations in all villages from year to year.

Table 1. Mean external dose rate to inhabitants of the studied villages during the autumn 2006, from Chernobyl contributions alone. Included are also results from previous years, from villages located in the same area.

Year	Village ($\mu\text{Sv month}^{-1}$)					
	St. Kusnetz		St. Bobovich		St. Yalovka	St. Demenka
1990	-	-	195	138	-	-
1991	171	165	-	-	216	-
1992	162	152	105	-	219	-
1993	127	132	98	105	-	-
1994	119	101	68	120	130	-
1995	117	109	-	-	100	-
1996	84	95	54	107	111	-
1997	67	83	-	-	138	-
1998	51	89	28	62	68	-
2006	-	-	31	48	-	57

As the Chernobyl contribution decreases, the calculated dose becomes associated with greater uncertainties. The pre-Chernobyl component from cosmic and terrestrial radiation (45 $\mu\text{Sv}/\text{month}$) has been adopted from the earlier studies and may be subject to variations between the villages.

The monthly effective doses are, on average, twice as high for the adults as for the children. The C_v for the adult and the children are 0.71 and 0.45 respectively.

There are large variations within the villages. In St. Bobovichs the C_v was 110 % and the highest individual dose was a factor of 4.5 higher than the mean for the village. However, the spread in individual doses is on average higher within a village than between villages, which is consistent with earlier findings.

The mean external contribution to the effective dose in 2006, from Chernobyl fall-out alone, was determined to 0.4 mSv/year. This is very close to the value reported in 2000 which would mean a reduction of only 3.6 % in 6 years. Even if the migration down into the soil and the other human activities that redistribute the radiocaesium have stagnated, the reduction due to physical decay, which alone amounts to 2% per year, should result in a more pronounced decrease in the dose rate. As mentioned previously, the observed stagnation in the dose rate may be influenced by an increased uncertainty due to prolonged storage times after the measurements.

The decrease of the external dose can be described by a sum of two exponential decay functions, with two different decay constants at different periods. The effective dose from external irradiation of Chernobyl caesium was decreasing with a rate of 20 % per year during the first three years of the study. After that period there is a slower decrease of 12 % per year between 1994 and 1998. An exponential regression was matched to these years and extrapolated to 2006. The regression with a reduction rate of 12 % per year is just in-between the levels measured in 2000 and 2006. This illustrates the difficulties in determining doses close to the background radiation level. Another expedition in 2008 would clarify this discrepancy.

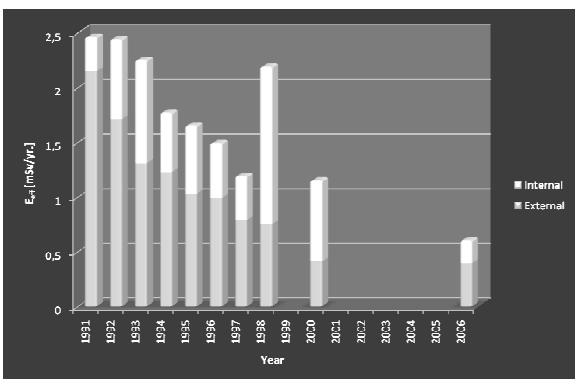


Fig. 1. Effective dose from internal- and external sources as measured during the expeditions between 1991 and 2006. N.B. the doses are calculated as a population average for inhabitants in the villages mentioned in Table 1.

Body burden of ^{137}Cs – Internal dose contribution.

In total 317 individuals in four villages were subject to whole body counting. Urine samples were collected from 12 of the highest internally contaminated individuals. The distribution of body content of ^{137}Cs in

individuals from the four villages is presented in Figure 2.

The total body burden of caesium is highly dependent on food habits and on the amount of forest products available during the different years. As the measurements were performed during the autumn the observed ^{137}Cs body contents will most likely be somewhat higher than during the rest of the year when there is little forest products available. Hence the yearly effective dose may be overestimated.

The internal levels of caesium are similar between the villages and increases with age i.e. the amount of food consumed. In the adult female group however, there are large variations between the villages. As earlier discussed [10] there was no correlation between the whole-body contents of caesium (during 1991 – 1994) and the soil contamination. As can be seen from Figure 2, the inhabitants of the most contaminated village, Yalovka, have on average lower ^{137}Cs body burdens than the inhabitants of Demenka and St Vyshkov. The adults in Demenka have almost twice the body burden of caesium as the adults in Yalovka, but half the contamination level (in 1986). It can partly be explained by the selection of the measured people: In Yalovka most part of adults were teachers and members of the local administration, who more carefully observe the recommendations on restriction of forest products consumption than the people measured in Demenka, where most measured persons were agriculture workers, who were more dependent on forest products.

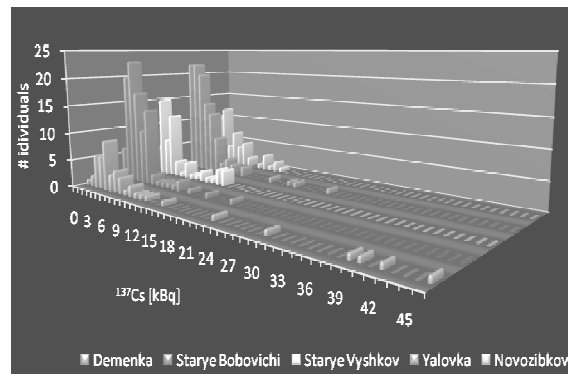


Fig. 2. Histogram illustrating the distribution of the ^{137}Cs body burden. All age groups are included. Most of the measured individuals were school children except in Demenka and Novozibkov.

A high individual variation in the contamination levels within the villages is observed. There is also a significant difference between the ^{137}Cs body burden in the town of Novozibkov and the four rural villages (Figure 2). In these villages, the inhabitants are more self-sufficient and produce much of their own food. In Novozibkov on the other hand, most of the consumed food comes from grocery stores (that import their food from outside the region. Some of the individuals in the villages exhibit values up to 50 kBq, which greatly

exceed the average for the villages of 4 kBq. In Novozibkov on the other hand, no levels above 12 kBq of ^{137}Cs were observed.

The effective dose from internal irradiation is more complexly related to the contamination level in the village than the effective dose from external irradiation as it depends more on social factors than the latter. Also, the internal dose component is highly dependent on the amount of forest products available (especially mushrooms) and the relative amount of adults participating in the *in vivo* measurements. However, the dose from internal contamination is, on average, 76 % of that received from external irradiation (including the two extreme years 1998 and 2000). A few years after the accident the contribution from external exposure of ^{137}Cs to the effective dose was dominating. As this component has decreased, the effective dose from internal irradiation becomes more decisive for the total effective dose, especially during the years with rich mushroom harvests. Another observation is that the average internal dose levels in 1991 and 2006 are almost the same and after 1991 it increases considerably. The reason for this may be that until 1991 the inhabitants followed the recommended countermeasures but as the economical situation became worse they had to rely more on their own production of food and collection of forest products again [10].

The mean body burden of ^{137}Cs from the *in vivo* measurements agrees well with that estimated from the single urine sample when using tabulated voiding data and the creatinine normalization method [11].

4. Conclusions

Twenty years after Chernobyl, the yearly effective dose contribution from exposure to ^{137}Cs of the inhabitants in the rural villages studied is in the order of 0.5 mSv. This is similar to the contribution from cosmic radiation and radiation from naturally occurring radionuclides in the human body. The initial fast reduction of the decrease in external irradiation has leveled off. There are still large variations in the ^{137}Cs content of the individuals. This may be explained by the highly inhomogeneous contamination level and different attitudes to dietary recommendations.

5. References

1. Wallström E., Thornberg C., Erkin V., Wöhni T., Gulikov V., Zvonova I., Jesko T., Alpsten M., Balonov M. and Mattsson S. Estimation of Radiation Doses to Population Groups in the Bryansk Area Following the Chernobyl Accident. In: Environmental impact of radioactive releases, IAEA-SM 339/96 IAEA, Vienna, 1995. p. 413-420
2. Thornberg C., Vesanen R., Wallström E., Zvonova I., Jesko T., Albinsson J., Börjesson J. and Mattsson S. Long-term External Radiation Exposure of Inhabitants in the Western Bryansk Region of Russia as a Consequence of the Chernobyl Accident. Radiation Environmental Biophysics, 2001. 40:287-294
3. Thornberg C., Vesanen R., Wallström E., Zvonova I., Jesko T., Balonov M. and Mattsson S. External and Internal Irradiation of a Rural Bryansk (Russia) Population from 1990 to 2000, Following High Deposition of Radioactive Caesium from the Chernobyl Accident. Radiation Environmental Biophysics, 2005. 44:97-106
4. Jacob P., Paretzke H., Rosenbaum H. and Zankl M. Organ Doses From Radionuclides on the Ground. Part I. Simple Time Dependences. Health Physics, 1988. 54:617-633
5. Jacob P., Paretzke H., Rosenbaum H. and Zankl M. Effective Dose Equivalents for Photon Exposure from Plane Sources on the Ground. Radiation Protection Dosimetry, 1986. 14:299-310
6. Golikov V., Balonov M., Erkin V. and Jacob P. Model validation for External Doses due to Environmental Contaminations by the Chernobyl Accident. Health Physics, 1999. 77:654-661
7. Fogh C., Andersson K., Barkovsky A., Mishine A., Ponamarjov A., Ramzaev V. and Roed J. Decontamination in a Russian Settlement. Health Physics, 1999. 76:421-430
8. Zvonova I., Bruk G., Kaidanovsky G., Jesko T. and Balonov M. Mass Internal Exposure Monitoring of the Population in Russia After the Chernobyl Accident. Radiation Protection Dosimetry, 2000. 89:173-178
9. ICRP, International Commission on Radiological Protection, Age-Dependent Doses to Members of the Public from Intake of Radionuclides: Part 2 Ingestion Dose Coefficients, Publication 67, 1993. Part 2
10. Zvonova I., Jesko T., Balonov M. and Danilova I. ^{134}Cs and ^{137}Cs Whole-Body Measurements and Internal Dosimetry of the Population Living in Areas Contaminated by Radioactivity After the Chernobyl Accident. Radiation Protection Dosimetry, 1995. 62:213-221
11. Rääf C., Thornberg C., Mattsson S. Urinary Excretion Measurements for the Assessment of Body Burden of Radiocaesium in Man: Differences Between Potassium and Creatinine Normalisation. Applied Radiation and Isotopes, 1999. 51:505-514

MODELLING OF MASS CUMMULATION PROCESSES OF Cs-137 AND Sr-90 IN NUCLEAR FUEL

Gediminas A. ADLYS, Gediminas G. ADLYS

Kaunas University of Technology. Studentų g.50, LT-51368 Kaunas, Lithuania

Abstract

High radiotoxic ^{90}Sr and ^{137}Cs isotopes are most important radioactive pollutants in the environment created by radioactive fallout and by nuclear fuel cycle. This study is concentrated on the quantitative and qualitative investigation of the cumulative behaviour of all strontium and caesium isotopes during the burn up and cooling time of nuclear fuel of the RBMK-1500 type reactor, which operates at Ignalina Nuclear Power Plant. Nuclear fuel of operating nuclear reactor is a potential source of accumulated activity, which can enter the surrounding environment. Investigation was performed on base of modelling results, which are important for the risk assessment of environmental contamination and for the interpretation of the results of direct field measurements.

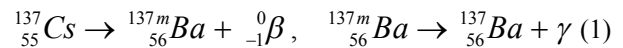
Keywords: APOLLO1, burn-up, fission products, nuclear fuel, PEPIN, SR-90, Cs-137, RBMK reactor.

1. Introduction

Strontium ^{90}Sr and caesium ^{137}Cs are the most dangerous radioisotopes to the environment in terms of their long-term effects. ^{90}Sr has a half-life of 28,79 years and ^{137}Cs - 30,07 years. Because of their intermediate half-lives of about 30 years both radionuclides are highly radioactive and can be incorporated into environment for the long time. Nuclide with a short half-live may cause higher initial dose, but it disappears very soon. Strontium, ^{90}Sr is chemically similar to calcium, and caesium, ^{137}Cs – to potassium. In such a case they have the property of being mistaken for calcium and potassium by living organism: This means that they could be included into the food chain. People may ingest ^{90}Sr and ^{137}Cs with food and water, or may inhale it as the dust particles. ^{90}Sr tends to be deposited in bone and blood-forming tissue (bone marrow). Caesium ^{137}Cs is distributed nearly uniformly in the soft tissues of body. Slightly higher concentration of ^{137}Cs is found in muscle and lower – in bone and fat. ^{137}Cs remains in the body for a relatively short time, as compared to some other radionuclides. It is eliminated through the urine. Exposure to cesium-137 may also be external.

Strontium ^{90}Sr decays to yttrium ^{90}Y , which, in turn, decays to stable zirconium ^{90}Zr . ^{90}Sr emits moderate energy beta particles, and ^{90}Y is a strong (energetic) beta emitter ($E_\beta = 2280$ keV) with a short half-life ($T_{1/2} = 64$ h).

Caesium ^{137}Cs undergoes radioactive decay with the emission of beta particles and relatively strong gamma radiation. ^{137}Cs decays to barium $^{137\text{m}}\text{Ba}$, - a short-lived decay product, which in turn decays to a stable barium ^{137}Ba (Eq.1). The major dose attributed to ^{137}Cs is a dose from $^{137\text{m}}\text{Ba}$.



Strontium ^{90}Sr emits a beta particle with, no gamma radiation, as it decays to yttrium ^{90}Y

The most common test for exposure to ^{90}Sr is a bioassay, usually done by urin analysis. It is possible to measure the amount of radionuclides in urine, or in fecal samples, even at very low levels. A technique called "whole-body counting" allows to detect gamma radiation emitted by ^{137}Cs in the body.

Strontium ^{90}Sr and caesium ^{137}Cs can enter the environment from a variety of sources. The largest source was the fallout from atmospheric nuclear weapons tests in the 1950s and 1960s, which dispersed and deposited radionuclides world-wide. However the main amount of the ^{90}Sr and ^{137}Cs produced during the weapon tests has been decayed in our days.

Strontium ^{90}Sr and caesium ^{137}Cs are also found in spent nuclear fuel from nuclear reactors. They are considered to be the more hazardous constituents of nuclear wastes. The accident at the Chernobyl nuclear power plant also introduced a large amount of ^{90}Sr and ^{137}Cs into the environment.

The measurements of samples with "hot" particles, collected in South Lithuania showed that the nuclear fuel in the IV unit of Chernobyl NPP reached the temperature high enough for the evaporation of nuclides with very high evaporation temperature [1]. This phenomenon allows to treat the radioactive releases during Chernobyl accident in the same way as the radioactive fallout. High temperature radionuclide evaporation is not characteristic for the usual releases of operating nuclear power plant.

Caesium is one of only three metals (caesium, gallium, and mercury) that is a liquid at room or near room temperature. Because of the chemical nature of caesium,

it moves easily through the environment. This makes the clean-up measures for cesium-¹³⁷Cs very difficult. Strontium can form many chemical compounds, including halides, oxides, and sulfides, and moves easily through the environment.

Presence of ⁹⁰Sr and ¹³⁷Cs is directly due to the nuclear fission of uranium and plutonium (in nuclear weapon or in nuclear fuel of the reactor). Despite of the all efforts escape of radioactive metals from the nuclear fuel rods is possible due to the fuel cladding disintegration. Strontium ⁹⁰Sr in this case is not quite as likely as caesium ¹³⁷Cs, because it is much less volatile. At higher temperature caesium behaves similarly to the fission gases and is probably released together with them [2].

The fuel cladding disintegration is rated to 0,1% for all fuel rods of RBMK reactor. For the prognosis of possible radioactive releases it is necessary to study a build-up of all different precursors and their behaviour as they contribute to the amount of ⁹⁰Sr and ¹³⁷Cs in nuclear fuel.

Qualitative assessment of accumulated activities of all these isotopes during the operation of RBMK reactor and during the cooling period is of great importance for the evaluation of radioactive environmental contamination in any accidental case.

Qualitative and quantitative investigation of activity accumulation processes for Cs and Sr are presented in this work.

2. Modelling

Modelling of cumulated activities of caesium and strontium isotopes in nuclear fuel of RBMK 1500 type reactor was performed using French codes APOLLO1 [3] and PEPIN [4]. Computer code APOLLO1 is based on solving of Boltzman equation using the collision probability technique. Modelling data was used for the calculation of time dependent variations of nuclide concentration in decay chain by code PEPIN:

$$\frac{dN_i}{dt} = -(\lambda_i + \sigma_i \phi)N_i + Y_i F + \gamma_{i-1} N_{i-1}, \quad (1)$$

where N_i is the number of nuclei of the i -th fission product at the time t ; λ_i is decay constant; σ_i is the effective microscopic neutron capture cross-section; ϕ is neutron flux density; Y_i is the fission yield of nuclide i ; F is the fission rate; $\gamma_{i-1} = k_{i-1} \lambda_{i-1}$ is build up coefficient of nuclide i by the fission of nuclide $i-1$ with k_{i-1} as a branching ratio.

Calculations were used for the assessment of nuclide masses during burn-up of nuclear fuel in reactor and during its cooling period according the method described in [5]. Activity concentrations of radionuclides were estimated using NUCLIDE.NET data base [6].

Build-up of Sr and Cs isotopes in nuclear fuel and their behaviour was modelled for RBMK-1500 type reactor. It was assumed that the initial UO₂ nuclear fuel was

enriched with 2,4% of ²³⁵U and contained 0,41% of erbium as burnable neutron absorber.

Binary fission, which is most probable, creates two nuclei with different masses. Mass distribution of fission products is characterized by an asymmetric curve, which represents two maxima and valley in between separating groups of “light” and “heavy” fission products **Fig.1** [5].

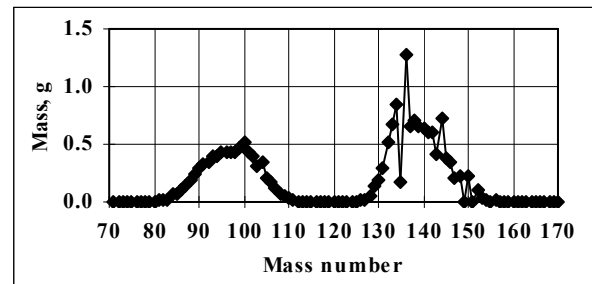


Fig.1. Mass distribution curve of fission products for the nuclear fuel burn up of 18 MWd/kg in RBMK-1500 reactor

Mass numbers of strontium isotopes range from 86 to 99 and from 133 to 147 for caesium isotopes as it could be found from CEA nuclide library [7]. Strontium has a position near the maximum of “light” fission products as well as caesium belongs to the top part of the maximum of “heavy” fission products in mass distribution curve. Due to the behaviour of isotopes belonging to different maxima, their quantitative variations are different during burn up of nuclear fuel.

It is assumed that beta decay does not change mass number of fission products and the shape of mass distribution curve is the same during cooling time of nuclear fuel. Nevertheless mass distribution of fission yields depends on spectrum of neutrons [8] and on creation of new actinides: increasing neutron energy results in the changes of the valley part of nuclides in mass distribution curve and the curve becomes more symmetric [9]. An increase of heavier nuclides fraction in nuclear fuel during its burn up is reflected by the shift of the maximum for “light” fission products towards the more heavy elements in the mass distribution curve, while the position of maximum for “heavy” fission products stays more or less stable.

It is necessary to point out, that isotope content of chemical elements produced in nuclear fuel during operation of nuclear reactor usually is different as compared to the isotope content of elements distributed in nature. Existing discrepancy is due to the fact, that all radioactive fission products have neutron excess and are concentrated on the same side from beta stability line. They are approaching to the stability line along their isobar chains from the side of heavier isotopes by means of β^- decay.

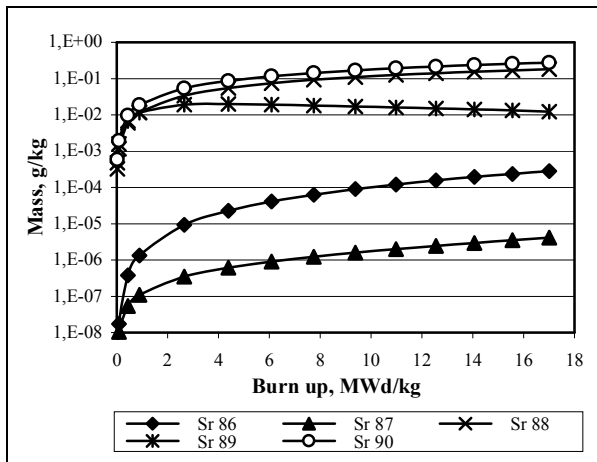
Strontium has 16 different isotopes. Naturally occurring strontium is found as four stable isotopes ⁸⁴Sr, ⁸⁶Sr, ⁸⁷Sr and ⁸⁸Sr. Twelve other isotopes are radioactive. ⁹⁰Sr is the most important radioactive isotope in the environment, although ⁸⁹Sr can be found around

reactors. Caesium has many isotopes, but it has only one naturally occurring stable isotope ^{133}Cs .

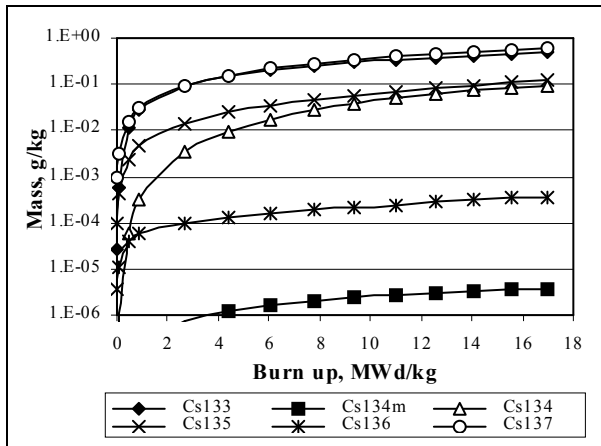
3. Results and discussions

When neutrons interact with nuclear fuel, concentration of ^{235}U isotopes decreases. Due to the capture of neutrons by actinide (starting with ^{238}U) and further successive β^- decay, new fissile actinides ^{239}Pu and ^{241}Pu and fissionable actinide ^{240}Pu are produced.

Mass accumulation behaviour of fission products depends on half-life. Short-lived ^{93}Sr , ^{94}Sr , ^{95}Sr , ^{96}Sr , ^{97}Sr , ^{98}Sr and ^{99}Sr isotopes and ^{141}Cs , ^{142}Cs , ^{143}Cs , ^{144}Cs , ^{145}Cs , ^{146}Cs and ^{147}Cs isotopes reach their mass saturation values very quickly. After that the masses of these isotopes start to decrease because of the neutron capture processes. The mass concentrations of intermediate, long-lived and stable nuclides are increasing steadily with the burn up of nuclear fuel as it is indicated in Fig.2A for strontium isotopes and in Fig.2B for caesium isotopes. Stable isotope ^{88}Sr makes 38 % of the total mass of all produced strontium isotopes and stable ^{133}Cs makes 41 % of the total mass of all produced caesium isotopes for the nuclear fuel burn-up of 18 MWd/kg in RBMK 1500 type reactor.



A



B

Fig.2. Accumulation of strontium (A) and caesium (B) isotopes for different burn up of nuclear fuel

Total mass accumulation process for all isotopes of fission products is following the increasing tendency depending on behaviour of each isotope. Accumulation process is faster for Cs isotopes as compared to Sr isotopes (Fig.3).

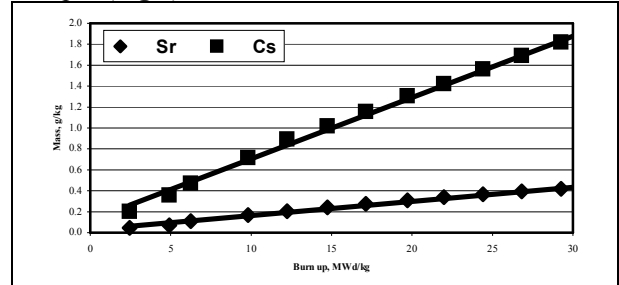
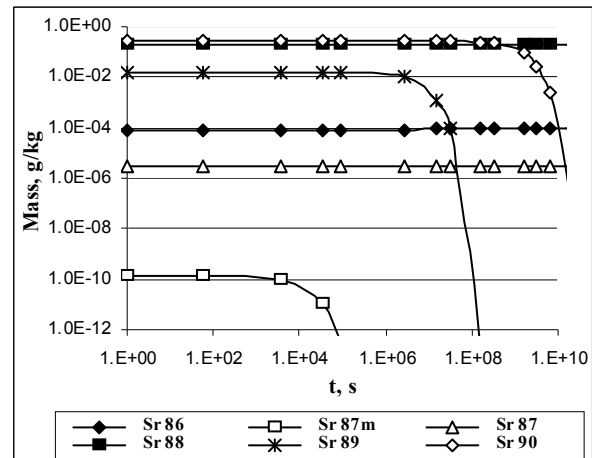
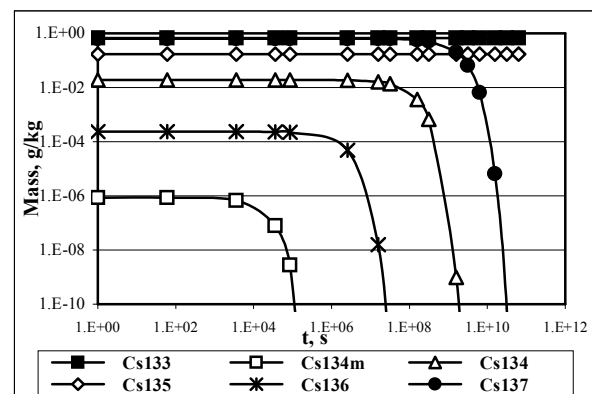


Fig.3. Accumulation of all strontium and caesium isotopes for different burn up of nuclear fuel

Very actual information about the possible environmental contamination could be gathered modelling radionuclide behaviour during cooling period, when reactor is shut down or spent nuclear fuel is removed from the reactor. Quantitative variations of mass concentrations of strontium and caesium in spent nuclear fuel after 18 MWd/kg burn-up during cooling time period are presented in Fig.4A and Fig.4B respectively.



A



B

Fig.4. Quantitative changes of radioactive ^{89}Sr and ^{90}Sr and stable ^{86}Sr , ^{87}Sr , ^{88}Sr (A) and radioactive ^{134}Cs , ^{135}Cs , ^{136}Cs , ^{137}Cs and stable ^{133}Cs , (B) during cooling period of spent nuclear fuel

Short-lived radionuclides being strong irradiation sources are most important at the moment when nuclear reactor is shut down or when spent nuclear fuel is removed from the reactor, while releasing a large amount of decay heat. ^{96}Sr , ^{97}Sr , ^{98}Sr and ^{99}Sr isotopes decay during the first minute after reactor was stopped or the fuel was removed. ^{95}Sr disappears after one hour; ^{94}Sr and ^{93}Sr –after one day. Analysis of decay chains shows that ^{95}Zr with half-life of 64,02 d, having ^{95}Sr as a precursor, would be a source of the environmental contamination.

Only one minute is long enough for decaying of ^{145}Cs , ^{146}Cs and ^{147}Cs isotopes as well as only one hour - for decaying of $^{137\text{m}}\text{Cs}$, ^{141}Cs , ^{142}Cs , ^{143}Cs and ^{144}Cs . Nevertheless, if these radionuclides could escape from fuel rods to the environment during this time they would be precursors for radioactive nuclides, such as ^{141}La (3,92 h), ^{141}Ce (32,5 d), ^{142}La (1,52 h), ^{143}Ce (1,38 d), ^{143}Pr (13,57 d), ^{144}Ce (284,9 d). $^{136\text{m}}\text{Cs}$, $^{138\text{m}}\text{Cs}$, ^{139}Cs and ^{140}Cs disappear after one day. The last one is the precursor for ^{140}Ba (12,75 d) and ^{140}La (1,68 d). ^{138}Cs decays within few days.

Nuclides with the half-life ranging from the few years to few tens of years (^{90}Sr , ^{134}Cs and ^{137}Cs) are important for the interim storage as it is in the case of dry storage of spent nuclear fuel in CONSTOR and CASTOR casks at Ignalina NPP. Nuclides having half-life longer than 10^{10} years are assumed to be stable. Together with ^{90}Sr , ^{134}Cs and ^{137}Cs they are the object of long-term storage. Due to the fission of parent nuclides the mass of stable ^{133}Cs isotope increases approximately by 1% during the first month after the extraction of spent nuclear fuel from the reactor and stays stable after this time. The behaviour of radioactive ^{135}Cs is very similar to that of stable ^{133}Cs isotope although the half life of it is $2,3 \times 10^6$ years.

The relative activities of most important strontium isotopes are approximately the same: ^{89}Sr (10%), ^{91}Sr (13%), ^{92}Sr (14%), ^{93}Sr (16%), ^{94}Sr (15%), ^{95}Sr (13%), ^{96}Sr (10%) at the starting moment of cooling period of spent nuclear fuel. Caesium isotopes: ^{138}Cs (23%), ^{139}Cs (21%), ^{140}Cs (18%), ^{141}Cs (14%) and ^{142}Cs (8%) contribute significant to the total activity of all Cs isotopes at the same time. Time dependent total activity variations are presented in Fig.5.

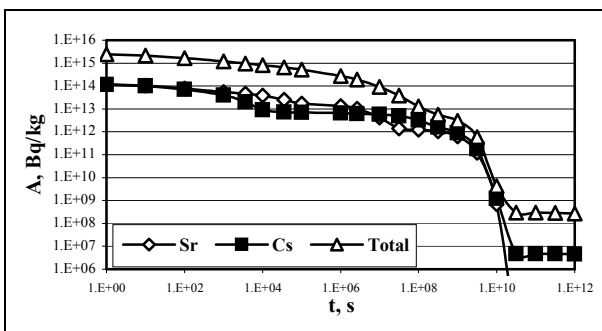


Fig.5. Activity variations of Sr and Cs isotopes and total of all fission products

Only ^{89}Sr and ^{90}Sr are presented in spent nuclear fuel after one year. Their activity is only 2,2% as compared to the total activity of all fission products. The activity of 4 remaining caesium isotopes, with the most important representatives of ^{134}Cs and ^{137}Cs is higher - approximately 9% of total activity. ^{90}Sr (20%), ^{134}Cs (2%) and ^{137}Cs (26%) are found in spent nuclear fuel after 10 years cooling period. Changes in numbers of strontium and caesium isotopes during the cooling time shown in Fig 6.

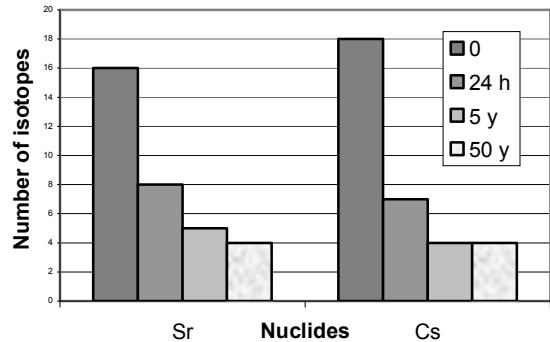


Fig. 5. Number of Sr and Cs isotopes in different cooling times

4. Conclusions

Inventory of the cumulated activities of caesium and strontium isotopes in nuclear fuel of RBMK 1500 type reactor was performed on the base of modelling results obtained using computer codes APOLLO1 and PEPIN.

Modelling results show that strontium isotopes with the mass numbers from the interval 87 – 99 and caesium isotopes with the mass numbers from the interval 133 - 147 could be produced during operation of the reactor. Quantitative variations of Sr and Cs isotopes are different during burn up of nuclear fuel as they belong to the different maximum regions in nuclide mass distribution curve and are dependent on neutron spectrum and on actinide content in nuclear fuel. Cumulative masses and activities of these isotopes depend on the initial fission product, half-life of isotopes and time period of investigation (operating facility, cooling period).

Short-lived isotopes ($^{93-97}\text{Sr}$ and $^{141-147}\text{Cs}$) reach their mass saturation values very quickly during operation of the reactor and than the masses of these isotopes start to decrease because of the neutron capture processes. The mass concentrations of intermediate and long-lived (^{90}Sr , ^{134}Cs , ^{135}Cs , ^{137}Cs) and stable (^{88}Sr , ^{133}Cs) nuclides are increasing steadily with the burn up of nuclear fuel. Stable isotope ^{88}Sr is represented by 38 % of the total mass of all produced strontium isotopes and stable ^{133}Cs by 41 % of the total mass of all produced caesium isotopes for the nuclear fuel burn-up of 18 MWd/kg in RBMK 1500 type reactor.

Due to the existing possibility for radionuclides to escape from the fuel storage facility, time dependent behaviour of Sr and Cs isotopes after the shut down of

reactor or remove of spent nuclear fuel from the reactor was investigated. Investigation showed that the contribution of the relative activities of the main Sr isotopes to the total activity is approximately the same but varies from 23 % for ^{138}Cs to 8% for ^{142}Cs at the starting moment of the cooling period. Only ^{89}Sr and ^{90}Sr are presented in spent nuclear fuel after one year. Their relative activity is 2,2% as compared to the 9% activity of caesium isotopes related to the total activity of all fission products. ^{90}Sr (20%), ^{134}Cs (2%) and ^{137}Cs (26%) are found in spent nuclear fuel after 10 years cooling period.

Assessment of the relative activities of Sr and Cs during the cooling period of spent nuclear fuel is of great importance as the nuclides with the half-life ranging from the few years to few tens of years (^{90}Sr , ^{134}Cs and ^{137}Cs) are an object of long-term dry storage of spent nuclear fuel in CONSTOR and CASTOR casks at Ignalina NPP.

Modelling results can and will be used for the further interpretation of the results of direct field measurements in the environment of operating RBMK 1500 type reactor and spent nuclear fuel storage facility. They can be useful for estimation of strontium and caesium isotopic content occurring during Chernobyl radioactive fallout.

References

1. V. Lujan, N. Špirkauskaitė, R. Jasiulionis, G. Adlys. „Hot“ particles in the area of Lithuania (in Russian). Optimizacija dozimetrisheskih problem. Vilnius. 1988. 66-69.
2. S. Portier, S. Bremier, C.T. Walker. Secondary ion mass spectrometry of irradiated nuclear fuel and cladding. International Journal of Mass Spectrometry 263 (2007) 113-126.
3. Le C.H., Mathonniere G. (1995): APOLLO1, Notice d'utilisation, Rapport DMT/SERMA/LENR, CEA
4. Duchemin B., Nimal B., Raepsaet C. (1995). Code PEPIN, Rapport DMT/SERMA/LENR, CEA
5. Adlys G., Adlienė D. (2002): Qualitative and quantitative characteristics in spent nuclear fuel from RBMK-type reactor. Lithuanian Journal of Physics 42(5), 371-377
6. Magill J. (2002): Nuclides.net. An integrated Environment for Computations on Radionuclides and their Radiation. Springer Verlag.
7. Constans A., Krebs J. (1991). La Bibliothéque CEA pour Apollo1 et Apollo2. Rapport DMT/SERMA/LERN.
8. Adlys G., Adlienė D. (2004): Neutron sources in spent nuclear fuel of RBMK-1500 type reactor. Lithuanian Journal of Physics 44(1), 59-65
9. Wagemans C. (1991): The Nuclear fission process. CRC Press.
10. <http://www.epa.gov/radiation/radionuclides>

MAMOLIT – DATABASE FOR PATIENT’S DOSIMETRY IN MAMMOGRAPHY SCREENING EXAMINATIONS IN LITHUANIA

Inga CIBULSKAITĖ^{a,b}, Marius LAURIKAITIS^{a,c}, Diana ADLIENĖ^a, Jurgita LAURIKAITIENĖ^{a,c}, Miglė ŠNIUREVIČIŪTĖ^{a,b}, Aušra URBONIENĖ^d, Birutė GRICIENĖ^d

^aKaunas University of Technology

^bKaunas Medical University Hospital

^cOnkology Hospital of Kaunas Medical University

^dRadiation Protection Centre

Abstract

MAMOLIT –database for the patient doses obtained during mammography examinations mostly during screening is presented in this work. MAMOLIT-database includes the main parameters of the X-ray examination procedure performed for each patient and calculated average glandular doses. The use of this database makes it possible to compare the results of the individual dosimetry measurements, to establish and compare dose reference levels in different hospitals and to establish national dose reference for mammography screening examinations.

Keywords: mammography, entrance surface dose, average glandular dose, screening

1. Introduction

One of the most important things in X-ray radiography is a dose to patient. As there are no dose limits, the way to regulate the exposure to patient could be a certain dose reference level for the particular X-ray procedure. The reference dose levels for some standard X-ray procedures are already established in Lithuania [1]. However the dose reference level for the mammography examinations is adopted from the European regulations. The dose obtained during mammography screening procedure is especially important as it is performed not only for the patients with the indication as diagnostic case, but also for possible healthy patients as it is in the case of screening. Breast cancer still remains the most often cancer comparing with other. The practice of other countries and also Lithuania, showed that preventive breast cancer mammography screening programs helps in detection of the breast cancer in the early stage and to prevent women against fatal outcome of this disease. National mammography screening program has been started in September 2005. It is addressed to the women in the age of 50-69 years, the number of whose according to the database of health care institutions is ~ 413200 in Lithuania. It is planned to apply breast screening procedure to 60% of all mentioned women during 5 years. 14 mammography screening centres were involved in this project (4 centres in Vilnius, 4 centres in Kaunas, 1 centre in each of hospitals in Klaipėda, Šiauliai, Panevėžys, Alytus, Marijampolė and Utena) in 2005. Only 11 of these centres are continuing this work until now.

Four mammography X-ray examinations (Cranio-Caudal (CC) projection and Medio-Lateral-Oblique (MLO) projection for each breast of the patient) are

planned for the screening procedure. Two independent radiologists-reviewers evaluate mammograms according to the standard BI-RADS evaluation system.

Every X-ray exposure of patient is connected with the risk to initiate the development of cancer cells in the exposed tissue. Typical effective dose received by a patient during one exposure in mammography is 50 μ Sv. This dose equals to the risk of a fatal cancer 1/400 000 [2].

There are a lot of discussions about the benefit of mammography screening versus new cancer cases introduced during exposure, but there is the only way to participate in such a discussion – to have investigation based statistics.

Investigation of patient’s doses during mammography examinations in Lithuania has been started by scientists of Kaunas University of Technology in 2003 and runs now parallel to the National mammography screening program. The aim of this work was and is to establish database for the patient’s doses obtained during mammography examinations (both, screening and diagnostic), to identify the problems and to implement patient’s dose optimization measures on the base of it.

2. Instruments and methods

The dose to the breast tissue of an individual patient depends on the characteristics of the equipment being used for the examination; technological factors, selected for the examination (X-ray tube voltage, X-ray tube output, anode/filter combination, X-ray attenuation, film/screen system, focal spot to the target distance, compression force); size and density of the patient’s

breast. Application of the appropriate dosimetry method is of great importance too.

Investigation of patients doses during mammography examinations was performed in 11 health care institutions in Lithuania: S.Kudirka Hospital (Alytus), Clinic "Bendrosios medicinos praktika" (Kaunas), Dainava Outpatient department (Kaunas), Kaunas Medical University Hospital, Division of the Kaunas Medical University Hospital Oncology Hospital, Šančiai Outpatient Department (Kaunas), Klaipėda Hospital, Marijampolė Hospital, Panevėžys Hospital, Šiauliai Hospital, Utena Health Care Centre. Randomly selected groups consisting of 13-20 patients of different age and with different breast density and size were chosen for each investigation in each institution. Mammography units "ALFA RT" (Instrumentarium), "MAMMOMAT 100" (Siemens) or "MAMMODIAGNOST" with a grid, Mo/Mo or Mo/Rh anode / filter combination; Kodak Min-RD, Cawo Mammo R200 film cassettes and Kodak X-Omat, Konica Minolta, CEA films were used for the screening procedures. Exposure parameters were registered for each patient separately together with the values of the compression force and the compressed breast thickness, age of the patient and other individual data. Entrance surface doses to patients breast were measured using LiF:Mg,Ti TLD dosimeters: pellets with a size of (3.2x3.2x0.9) mm³, calibrated and read out using a Harshaw TLD5500 (Harshaw Bicron Radiation measurement products, Ohio, US) at the Department of Medical Radiation Physics at Malmö University Hospital; and tablets of ø5mm, which were calibrated at the SSL in Latvia and read out using Rados TLD system at Lithuanian Radiation Protection Centre. Depending on the type of the investigation, one to four dosimeters were placed on the breast surface at the reference point (central position, upper quadrant of the breast, 5-6 cm distance from the chest wall).

Average glandular dose (AGD), which is the main dosimetrical parameter in mammography examinations, expresses the dose absorbed in the patient's breast tissue and is described as:

$$AGD = ESAKgcs \quad (1)$$

ESAK is entrance surface air kerma; *g* is entrance air kerma to mean glandular dose conversion factor (corresponds to a breast glandularity of 50%); *c* is correction factor for any difference in breast composition from 50% glandularity; *s* is correction factor for different X-ray spectra.

The value of entrance surface air kerma (*ESAK*) could be obtained dividing the value of measured entrance surface dose (*ESD*) by backscattering factor, *B*, which corresponds to the dosimeter used (European protocol on dosimetry in mammography. EUR 16263EN):

$$ESD = B * ESAK \quad (2)$$

Approximately 200 of patients have been examined and exposure doses to the patient's breast during mammography examinations have been investigated in 2006 with the respect to the dose influencing factors mentioned above.

5. Results and discussions

Database *MAMOLIT* was created for the monitoring of patient doses received during mammography examinations in Lithuania (Fig. 1).



Fig. 1. Front page of the database

The date of mammography examination, health care institution, where the examination has been performed, equipment, which was used, technical and technological parameters of the exposure, individual data of mammography patients are included into database together with the values of measured entrance surface doses, values of the necessary conversion factors and the name of the person, who has performed dose measurements of patient. (Fig. 2).

MAMOLIT - Duomenų įvedimas

Data: _____ Įstaigos pavadinimas: _____

Įrenginio pavadinimas: _____ Al HVL, mm: _____ Anodas/filtrai: _____ Tyrimo pobūdis: _____

Laborantas atlikęs tyrimą: _____ Asmuo atlikęs matavimus: _____

Tiriamosios Nr.: _____ Tiriamosios amžius: _____ Kasetės dydis, cmxcm: _____ Filmo/kasetės kombinacija: _____

RCC (DT) projekcija **RML0 (D) projekcija**

kV	mAs	Storis, cm	Jėga, N	kV	mAs	Storis, cm	Jėga, N
Patamsėjimas	Dozometro Nr.	ESD, mGy		Patamsėjimas	Dozometro Nr.	ESD, mGy	

LCC (KT) projekcija **LMLO (K) projekcija**

kV	mAs	Storis, cm	Jėga, N	kV	mAs	Storis, cm	Jėga, N
Patamsėjimas	Dozometro Nr.	ESD, mGy		Patamsėjimas	Dozometro Nr.	ESD, mGy	

Kompleksinė apšvita

2 projekcijos 3 projekcijos 4 projekcijos

Dozometro Nr.	ESD2, mGy	Dozometro Nr.	ESD3, mGy	Dozometro Nr.	ESD4, mGy

Įvesti Atšaukti



Fig.2. Patient's data sheet

Database *MAMOLIT* calculates average glandular dose (AGD) for each patient and presents dose distributions in one institution or compares doses in different institutions.

It was found, that the patient's dose distributions versus compressed breast thickness differ significantly in different health care institutions (Fig.3 a and b) sometimes being unnecessary high as it is indicated in (Fig. 4).

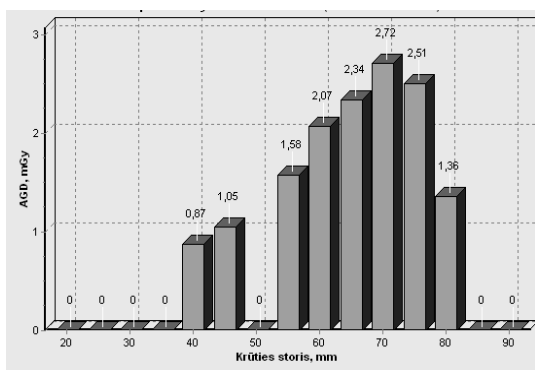


Fig. 3a. Patient's dose distributions versus compressed breast thickness on one of the health institutions

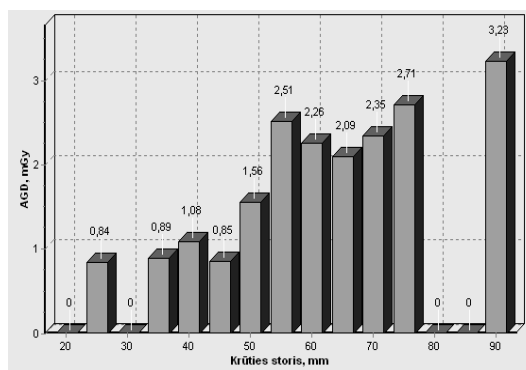


Fig. 3b. Patient's dose distributions versus compressed breast thickness on one of the health institutions

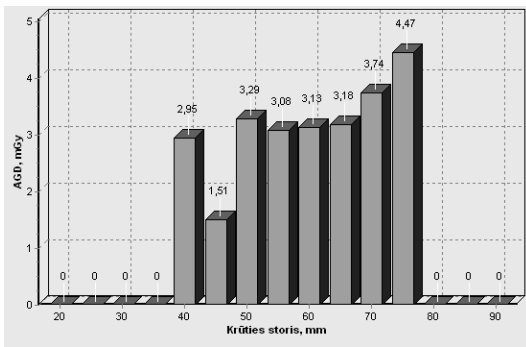


Fig. 4. Patient's dose distributions versus compressed breast thickness on one of the health institutions

The primary idea of patient's dose measurements during mammography examinations was setting of the dose reference levels in Lithuania and in each health care institution separately. Due to this reason the values of average glandular dose for a "standard", 50 mm compressed breast thickness, estimated in different hospitals (Fig.5) were compared and the reference level of 2.4 mGy with the certainty of the third quartile was evaluated. The results are promising, and hopefully it will be possible to reduce the existing 3 mGy reference dose level, which is defined in Lithuanian HN 31:2002 and is adopted from the European protocol on dosimetry in mammography, EUR 16263EN.

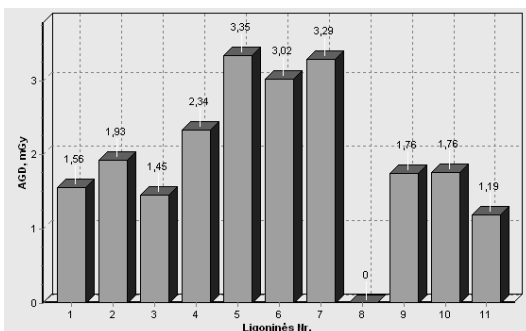


Fig. 5. AGD for a "standard" compressed breast thickness in different institutions

However, the facts of non adequate exposed patients were found in each hospital. Inadequate chosen X-ray tube voltage, compression force, or anode/filter combination are only the few problems, which were recovered during present investigation. Total dose to the skin (ESD) at the reference point in the area of superimposed X-ray fields during the complex mammography examination (4 exposures) is another big problem (Fig.6, Fig. 7).

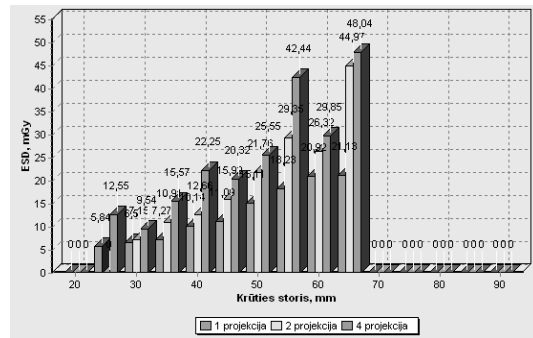


Fig. 6. ESD versus breast thickness in one of the health institutions (1 and 4 exposures)

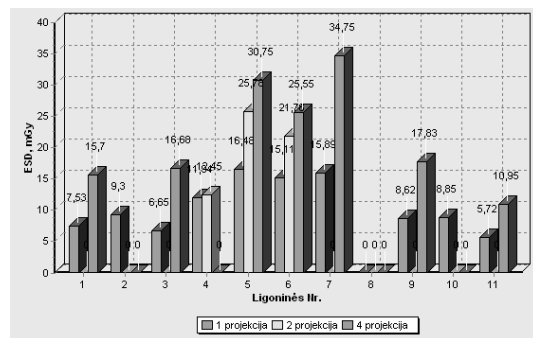


Fig. 7. ESD for "standard" compressed breast thickness in different institutions (1 and 4 exposures)

Since the dose reference level is evaluated for one exposure, attention is not paid for the total point dose during the complex examination, which is more than twice higher as compared to one - exposure dose. Solution of all these problems has to be considered when optimizing patient's doses during mammography examinations and reducing the risk for the new radiation induced cancer.

Acknowledgement

Authors would like to thank all staff at the different health care institutions helping to perform these measurements and the main contributors Viktorija Burinskienė (Kaunas Medical University), Eglė Jonaitienė (Kaunas Medical University Hospital), Skirmantė Mockevičienė, Rita Plaipaitė, Eglė Garnytė, Eglė Skripkaitė (Kaunas University of Technology), Vanda Andrijaitienė (Klaipėda University Hospital), G.Šetikienė (Šiauliai Regional Hospital)

This work was supported by Lithuanian State Science and Studies Foundation

5. References

1. HN 31:2002 "Radiacinės saugos reikalavimai medicininėje rentgeno diagnostikoje". patvirtinta Lietuvos Respublikos sveikatos apsaugos ministro įsakymu 2002 m. gruodžio 20 d. Nr.656.
2. John Sanderson. Radiation protection for assistant practitioners in mammography.
3. European protocol on dosimetry in mammography. EUR 16263EN. ISBN 92-827-7289-6. Luxemburg.

PRACTICAL ASPECTS OF VERIFICATION IN GAMMATHERAPY

Vanda Andrijaitienė^{*}, Lina Vespenderytė^{*}, Mindaugas Zikas^{*}, Diana Adlienė^{}**
^{*}*Klaipeda university hospital*
^{**}*Kaunas University of Technology*

Abstract

Verification systems are being used for the treatment quality improvement in radiation therapy. Old gammatherapy equipment don't allow to apply new technologies, therefore the preparation of patients for the treatment using verification system based on portal verification films is of advantage. Exposed films give enough information about the arrangement of irradiation fields, position of the blocks, central point of the target and patient positioning. Since the arrangement of anatomic bone structure of the patient is clear seen in the gammagraphic image, it is like a landmark for the physicians doing radio therapy planning. The application of film based verification system in gammatherapy is discussed in present paper.

Keywords: radiotherapy, gammatherapy, verification, portal films, immobilization of patients.

1. Introduction

In radiation therapy verification system is used for treatment quality improvement, which provides possibility to observe and estimate patient's treatment, to analyze the results of treatment, to plan the operation of the equipment and staff, to ensure the quality of the involved staff activities. In modern technology of radiation therapy special x-ray control system is used for this purpose. It allows to specify and adjust the position of the irradiation fields before the treatment. Treatment verification encompasses various radiation treatment stages from patient's identification and treatment prescription until radiation treatment: patient's simulation, definition of the irradiation target, individual dose panning, checking of the plan, periodical re-count and adjustment of source rate and patient's treatment (Fig.1).

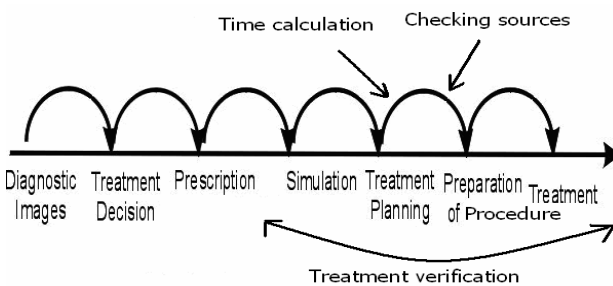


Fig. 1. The treatment chain in gammatherapy [1].

Gammatherapy equipment with ⁶⁰Co sources are still used in Lithuania. This equipment don't have patient's simulation and verification system, therefore

gammagraphy method is used for the patient's treatment verification. This method is widely used in the world [1], to ensure patient safety and treatment quality.

2. Verification method

Verification of patient's radiation treatment is performed by gammagraphy method using portal verification films. Verification cassettes are used for the improvement of image quality. Cassettes are made of one or few fluorescent screens both film sides, thin lead layer and backscatter plates. Gamma photons are converted to light photons during their interaction with cassette material (Fig.2 and Fig.3).

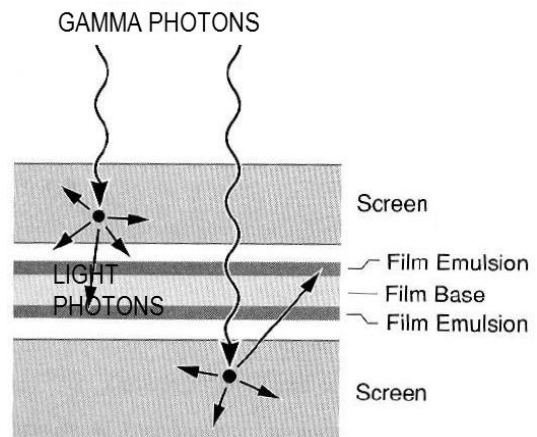


Fig. 2. Film-cassette system [2].

Gamma - verification films, like x-ray films, in general consist of silver halide crystals embedded into

gelatine matrix. One or both film sides are coated by this photographic emulsion. When film is exposed to gamma photon, electrons are ejected from the atom due to the photoelectrical and Compton effect; consequently silver ions occur. Ejected photo- and Compton electrons move towards vacancies and defects located in the grains of the silver bromide. During this process silver ions become silver atom. Latent image is formed from few (at least four) silver atoms and is seen after the film development. Not exposed crystals of silver halide are eliminated from the film after fixation and wash out procedures.

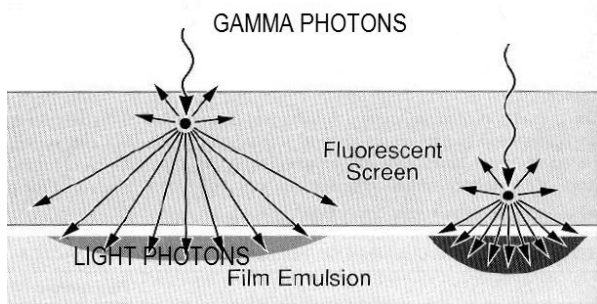


Fig. 3. Processes in film – cassette system during gamma photon interaction [2].

Film – cassette system for the verification purposes improves the image contrast three times approximately, thus anatomic contours of required location in patient are better seen. Due to the low film sensibility, this system can be exposed overall irradiation procedure time.

It is well known, that the individual radiation treatment plan has to be calculated for each patient separately with a purpose to protect healthy tissues surrounding the target and to provide overall dose to the target. Dose planning is performed according the determined incisions of the CT images, which are imported from medical imaging system. The central incision of image is used for radiation treatment planning by two-dimensional (2D) planning system.

Placing the markers on the patient's skin before CT examinations provides physician with the necessary information, when the geometry of the irradiation field is planned. A central marker, which is seen in CT image, allows to accurately define and adjust the irradiation area in the dose plan of the treatment. It is possible to compare the CT images with the images obtained by portal verification film. If the field in the image don't encompass the required irradiation area, it has to be resized and the dose plan has to be recalculated.

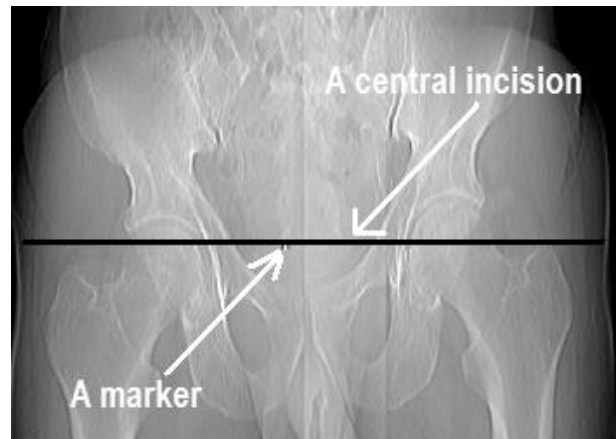


Fig.4. The image got by computed tomography.

Using verification system it is possible to check the arrangement of the irradiation field, the irradiated target area, positioning of the patient, the uniformity of the dose in the irradiated target area during the first treatment procedure of patient. However, planning patient's treatment it is necessary to pay additional attention to the movement of the treatment target due to the patient's breathing, cardiac moving, gas moving, muscle shrinkage, swallowing (Fig.5).

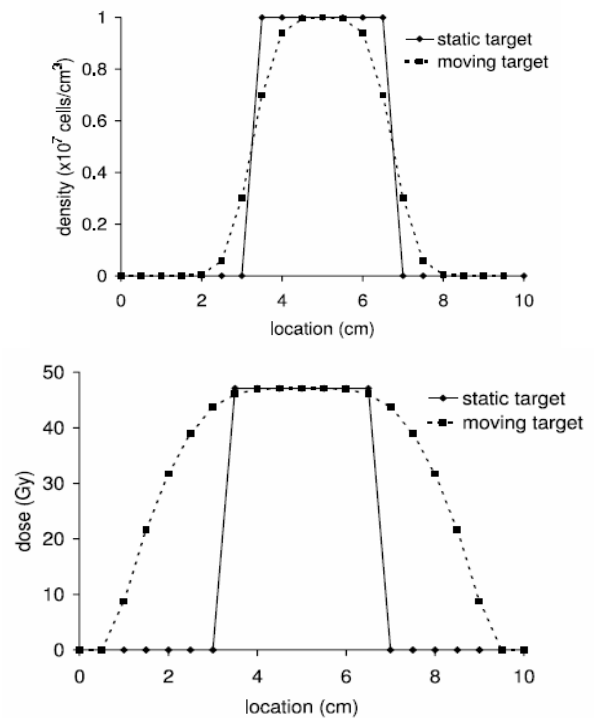


Fig.5. Distribution of density and dose in appropriate location of static and moving target [3].

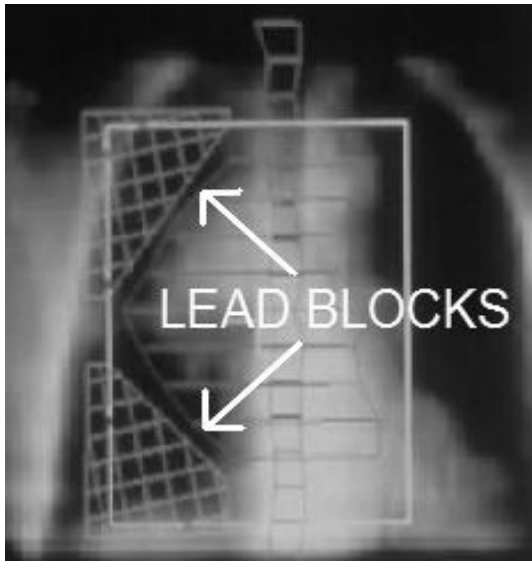


Fig.6. The arrangement of lead blocks seen in gammagraphic image[4].

It is possible also to identify the irregular shaped exposure fields formed by lead blocks in gammagraphic image, according which some necessary corrections could be done (Fig.6).

3. Results and discussion

Verification of the patient's positioning and field geometry was performed for top and lateral irradiation fields. In the case of the top irradiation gamma - films cassette system was positioned under patient, as it is indicated in Fig.7 and was exposed during the whole radiation treatment procedure.

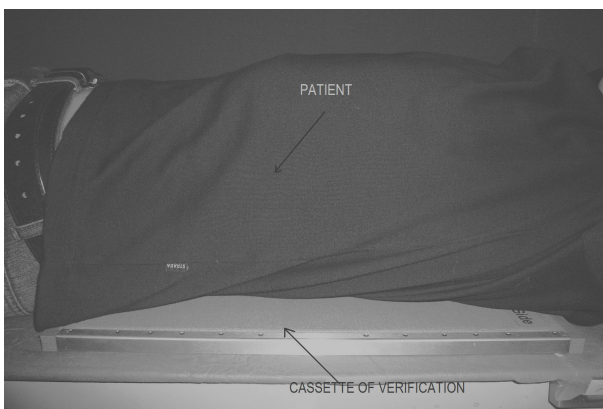


Fig.6. Verification of the irradiation field geometry for the top irradiation.

For the verification of lateral irradiation fields a cassette holder was used, which was positioned close to the patient in the lateral field direction.

Comparison of the CT image of the lungs (Fig.8a) with the gammagraphic image (Fig.8b) show the possibility to estimate, whether irradiation field fits well

with the required irradiation area of the target. In fact, the congruence of the fields contribute significantly to the right positioning of the patient. Anatomic arrangement of bones, which could be clearly seen in the gammagraphic image (Fig.8b) is a landmark in the comparison of the radiation fields.

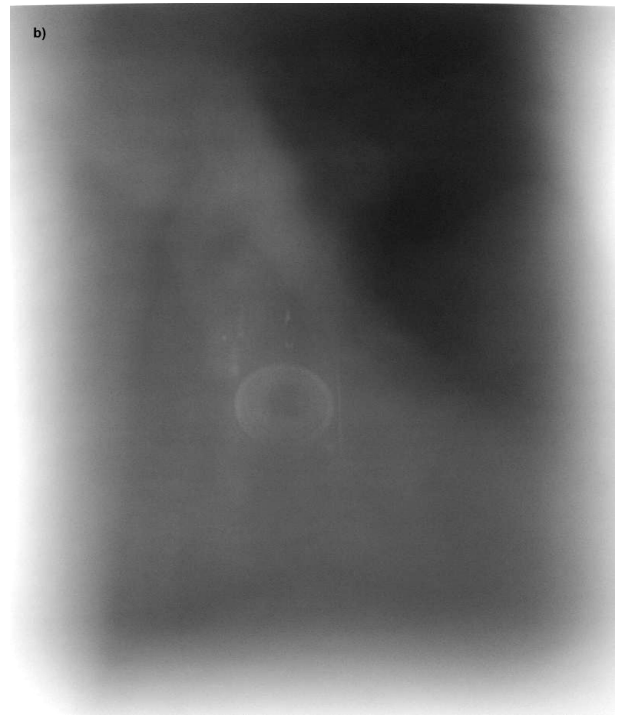
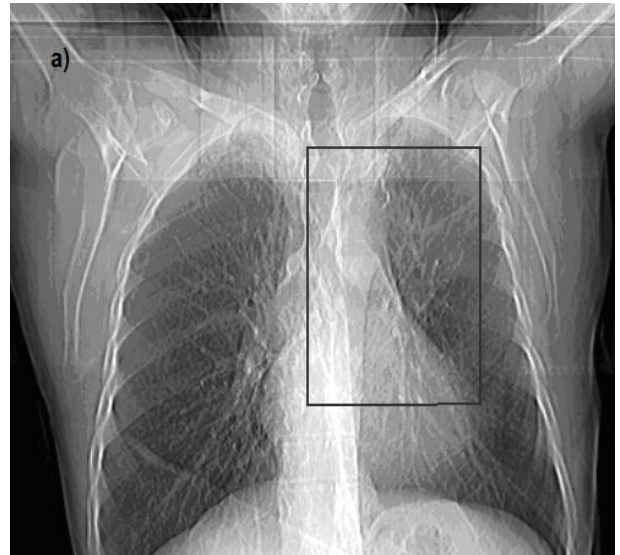


Fig.8. a) CT image of the lungs, b) Gammagraphic image of the lungs.

Comparison of patient's lung - CT image with the marked field for radiation treatment and gammagraphic image obtained during radiation treatment of the patient, has shown that the irradiation field corresponds to the planned treatment area. Consequently, the patient was positioned correctly, the

necessary dose was delivered to the target defined by the physician.

Comparison of the CT (Fig.9a) and gammagraphic images (Fig.9b) for pelvis treatment has shown some discrepancies in between prescribed and irradiated treatment field. It is clearly seen in the gammagraphic image (Fig.9b), that the irradiation field is moved to the left side in the area of pelvis bones. Do to this discongruency of the fields, patient has to be positioned by the appropriate distance to the left.

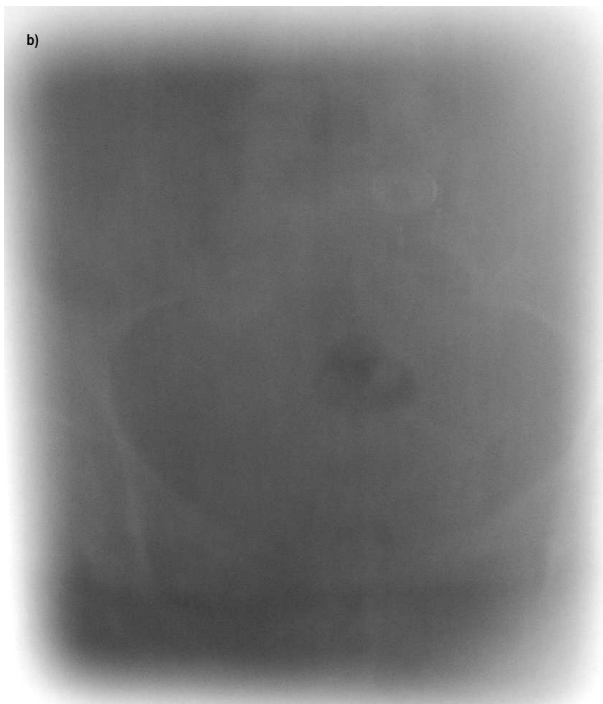
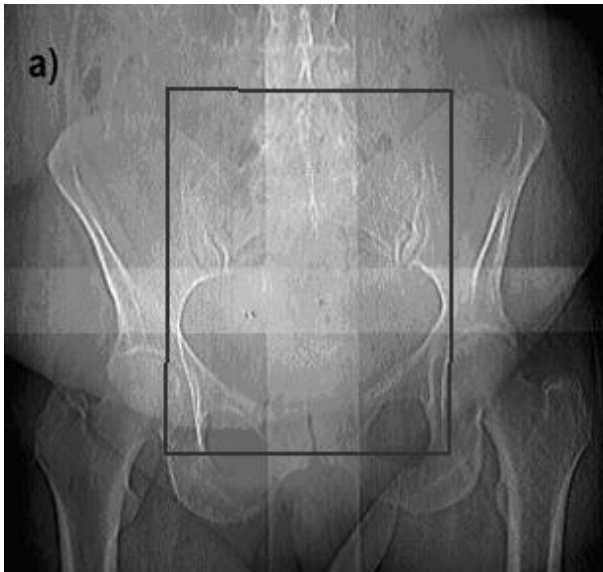


Fig.9. a) CT image of pelvis; b) gammagraphic image of pelvis.

4. Conclusion

The influence of positioning may be reduced by immobilization means. Appropriate immobilization means are used for each localization.

In gammatherapy target moving problem is heavily solved because of old equipment. In new technology, where the fourth parameter is involved (4D system), allowed to estimate target moving during irradiation procedure.

Verification with portal verification films gives enough information about geometric arrangement of irradiation fields in the point of target and patient positioning.

Aknowledgement

Support of the Lithuanian State Science and Studies Foundation is aknowledged

References

1. S. Popov, G. Boka, A. Miller, Yu. Dekhtyar. Implementation of portal dosimetry for patient related quality control in intensity modulated radiotherapy. *Medical Physics in the Baltic States*, (2006).
2. Anthony Brinton Wolbarst. *Physics of radiology*. 2003, Philadelphia, USA
3. A. Nederveen. Image guided position verification for intensity modulated radiotherapy of prostate cancer. 2002, Nederlands.
4. www.iaea.org.
5. W. Schlegel, T. Bortfeld, A.-L. Grosu. *New technologies in radiation oncology*. 2006, Springer, Germany.
6. J. Dobbs, A. Barrett, D. Ash. *Practical radiotherapy planning*. 1999, Great Britain.
7. *Absorbed dose determination in external beam radiotherapy*. International atomic energy agency, Vienna, 2000.
8. E.B. Podgorsak. *Radiation oncology physics: a handbook for teachers and students*. 2005, International Atomic Energy Agency, Vienna.

EVALUATION OF THE INSTANTANEOUS RADIOACTIVITY CONCENTRATION OF TECHNETIUM-99m

Eglė SKRIPKAITĖ*, Jurgita LAURIKAITIENĖ***

* Kaunas University of Technology, Studentų g. 50, LT-51368 Kaunas, Lithuania;

** Oncological Hospital of Kaunas Medical University, Volungių g. 16, LT-45434 Kaunas, Lithuania

Abstract

Technetium-99m (^{99m}Tc) is a radionuclide, which is daily used in hospitals. It is very important to know a real activity concentration of this radionuclide at each moment. However estimation of the activity concentrations of the Technetium-99m is problematic, since instantaneous activity concentration depends on different parameters. Gamma spectrometer IdentifINDER was used for the measurement of instantaneous ^{99m}Tc spectrum and the results of the experimental measurements were used for the calculation of the activity concentrations. Comparison of the results on the estimation of the activity concentration using experimental measurements and calculations, performed using different computing tools are presented.

Keywords: technetium-99m, activity concentration, gamma spectra

1. Introduction

^{99m}Tc is widely used for medical applications, as the radiation from this isotope is a gamma ray with the same energy as the X-rays, used for common medical diagnostic X-ray applications. Its penetration mechanism causes minimal damage of the tissue. Very short half-life (6.01h) of this metastable nuclear isomer, followed by the relatively long half-life ($2.14 \times 10^5 \text{y}$) of the daughter isotope ^{99}Tc , which allows it to be eliminated from the body before it decays, makes ^{99m}Tc very attractive for a relatively low administrated dose applications, for example in immunoscintigraphy. [1]. Immunoscintigraphy incorporates technetium-99m (^{99m}Tc) into a monoclonal antibody, an immune system protein capable of binding to cancer cells. A few hours after injection, medical equipment is used to detect the gamma rays emitted by the ^{99m}Tc . Higher concentrations of this radionuclide indicate the position, where the tumor could be. This technique is particularly useful for detecting hard-to-find cancers, such as those affecting the intestine [2].

Exact determination of the radioisotope parameters, such as concentration, radioactivity, specific radioactivity, etc. is very important in daily work of the hospitals. Sometimes it is very convenient for the parameter calculations to use computing tools, which could be easily found in the Web pages. However one has to answer the question: are they reliable? Due to this reason the main purpose of this investigation was to compare the results of the activity calculations, obtained using different computing tools and the results of calculation performed using experimental data of spectrometric measurements.

2. Experimental details

$^{99}\text{Mo}/^{99m}\text{Tc}$ generators. For medical purposes Technetium-99m is usually extracted from $^{99}\text{Mo}/^{99m}\text{Tc}$ generators (Fig.1).

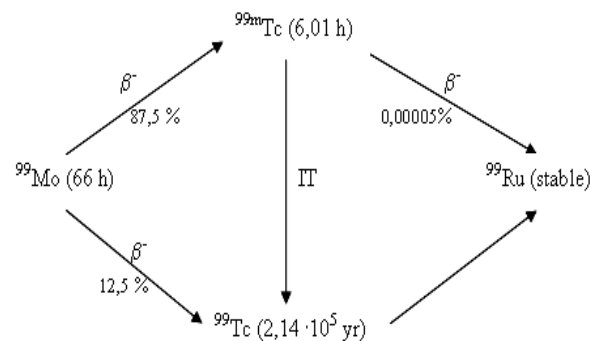


Fig. 1. Radionuclide generator of $^{99}\text{Mo}/^{99m}\text{Tc}$ [5]

The metastable isotope ^{99m}Tc is produced as a fission product from the fission of uranium or plutonium in nuclear reactors. It is well known, that the spent nuclear fuel has to be stored for a several years before reprocessing. Due to this fact, all ^{99}Mo and ^{99m}Tc will decay during the time until fission products will be separated from the major actinides in conventional nuclear reprocessing.

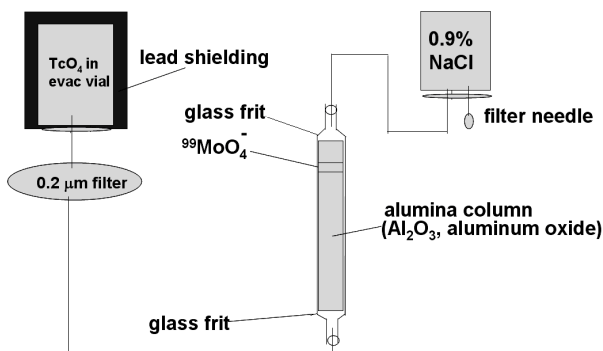


Fig. 2. Radionuclide generator of $^{99}\text{Mo}/^{99\text{m}}\text{Tc}$ [6].

The vast majority of the $^{99\text{m}}\text{Tc}$ used for medical purposes is formed from ^{99}Mo , which is formed by the neutron activation of ^{98}Mo . ^{99}Mo has a half-life of 67h, so it is possible to produce constantly a short-lived $^{99\text{m}}\text{Tc}$ (6,01 h) as a result of its decay [3]. $^{99\text{m}}\text{Tc}$ is produced in so-called radionuclide generator, as it is shown in Fig.2. It is to assume, that the end product of this generation process is the PUREX raffinate, which contains a high concentration of technetium as TcO_4^- . Almost all technetium in TcO_4^- is ^{99}Tc [3].

Gamma spectrometer *IdentiFINDER* represents digital hand held gamma spectrometer (Fig.3) created for in situ operation and having special features of:

- gamma dose and dose rate measurement;
- searching for single radioactive gamma sources or for areas of contamination with gamma radionuclides;
- automatic identification of radio nuclides based on measured gamma ray spectra.

It carries out qualitative and quantitative analysis of gamma radiation using a $\varnothing 1'' \times 2''$ NaI(Tl) crystal. An onboard DSP (Digital Signal Processor) with a sophisticated software and an internal data base enables the *IdentiFINDER* to carry rate measurement A GM tube is integrated into the unit [4].



Fig. 3. Gamma spectrometer *IdentiFINDER*.

Computing tools for radioactivity calculations are used particularly for the calculation of radioisotope activity, concentration, decay constant and other

parameters. Calculation results based on experimental measurements using *IdentiFINDER* were compared with the results obtained from calculations performed using: Calculator1 - Universal Decay Calculator (Wise Uranium project); Calculator2 - Radioactive Decay Calculator (UBC Radiation Safety); Calculator3- GrapPad Quick Calculators. (The working window of Calculator3 is presented in Fig.4 [5]).

Concentration of stock	% remaining isotope: 89.08%
Original dilution: 13	mCi/ml
Original activity: 2200	Ci/mmmole
Stock Concentration = 5.263 micromolar	
Assumes compound was 100% labeled originally (carrier free)	
Dilution of stock	Concentration of stock solution (micromolar): 5.263
	Dilute to this concentration in nM: 6
	Final dilution volume in ml: 1
Stock volume needed = 1.14 microliter	
Specific activity (cpm/fmol)	Specific radioactivity: 2200 Ci/mmmole
	Counter efficiency (%): 16%
Specific Activity = 781.4 cpm/fmol	

Fig. 4. GrapPad Quick Calculators

3. Results and discussion

Calculation of the radioactive decay constant

Radioactive decay is the process in which an unstable atomic nucleus loses energy by emitting radiation in the form of particles or electromagnetic waves. Fission of ^{99}Mo produces metastable $^{99\text{m}}\text{Tc}$. Decay equation and decay scheme is presented in Fig.5:

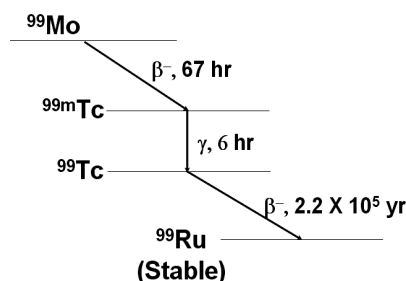
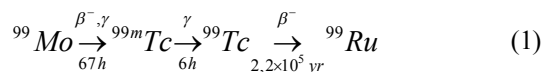


Fig. 5. Decay scheme of ^{99}Mo .

Gamma spectrum of $^{99\text{m}}\text{Tc}$ was registered using the gamma spectrometer *IdentiFINDER* (Fig.6). This radioisotope emits detectable gamma rays with energy of 140 keV [6].

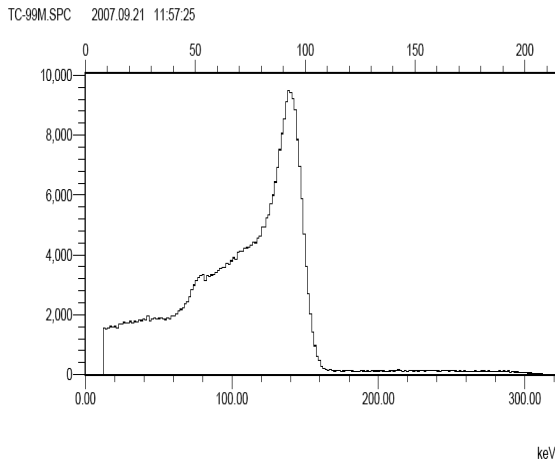


Fig. 6 Spectrum of ^{99m}Tc.

The number of decay events $-dN$ expected to occur in a small interval of time dt is proportional to the number of atoms present. If N is the number of atoms, then the probability of decay ($-dN/N$) is proportional to dt :

$$\left(-\frac{dN}{N}\right) = K_{decay} \cdot dt \quad (2)$$

Particular radionuclides decay at different rates, each having its own decay constant (K_{decay}). The negative sign indicates that N decreases with each decay event.

The solution to this first-order differential equation is the following function:

$$N_t = N_0 \cdot e^{-K_{decay} \cdot t} \quad (3)$$

N_0 are the initial activity and N_t are the activity at the time t [7].

The half-life ($t_{1/2}$) is the time necessary for a half the isotope to decay. Half-life and decay rate constant are related by the equation:

$$t_{1/2} = \frac{\ln(2)}{K_{decay}} = \frac{0,693}{K_{decay}} \quad (4)$$

Knowing the half time of ^{99m}Tc accordingly to the equation (4) the calculated decay constant is 0.1155 per hour.

Radioactive decay of ^{99m}Tc is shown in Fig.7. It could be assumed that the radioactivity of this radioisotope is approximately equal to zero after two days.

It is possible to calculate radioactive decay from a data, if the concentration and specific radioactivity are known using following equation:

$$\text{Fraction remaining} = e^{-K_{decay} \cdot \text{Time}} \quad (5)$$

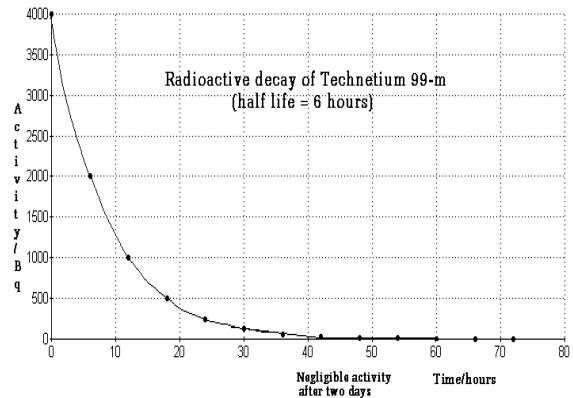


Fig. 7. Radioactive decay of ^{99m}Tc [5].

For example, after 1 day the remaining fraction of ^{99m}Tc equals 6.25 %.

Counter efficiency and specific radioactivity. The fraction of radioactive disintegrations detected by the counter is called efficiency. The efficiency of the counter can be determined by counting a standard sample under conditions identical to those of experiment.

It is relatively easy to detect gamma rays emitted from isotopes such as ¹²⁵I, so efficiencies are usually over 90 %, which depends on the geometry of the counter. The detector does not entirely surround the tube, so a small fraction of gamma rays (photons) miss the detector. The efficiency of the counter is equal:

$$E = \frac{cpm - cpm_{background}}{dpm} \quad (6)$$

Specific radioactivity can be expressed in Bq/gC, dpm/g. However, radioactivity of the commercially available radionuclides is usually indicated as Curies per millimole (Ci/mmol). Since most of the experimental measurements are performed in counts per minute (cpm), it is more useful to change the specific radioactivity units to be in terms of cpm rather than Curie. Often the specific radioactivity is expressed as cpm/fmol (1 fmol = 10⁻¹⁵ mol).

The conversion from Ci/mmol to cpm/fmol, is possible assuming that 1 Ci equals 2.22 x 10¹² disintegrations per minute. The following equation converts element Z Ci/mmol to element Y cpm/fmol when the counter has an efficiency equal to E (Eq.7) [9]:

$$Y \frac{cpm}{fmol} = Z \frac{Ci}{mmol} \cdot 2,22 \times 10^{12} \frac{dpm}{Ci} \times 10^{-12} \frac{mmole}{fmole} \cdot E \frac{cpm}{dpm} = Z \cdot 2,22 \cdot E \quad (7)$$

Then:

$$Y \frac{cpm}{fmol} = Z \frac{Ci}{mmole} \cdot 2,22 \cdot E \quad (8).$$

⁹⁹Mo/^{99m}Tc Radionuclide generator produces sterile, pyrogen-free and isotonic water solution of sodium pertechnetate ^{99m}TcO₄. So calculated specific radioactivity of ^{99m}TcO₄ is equal 2200 Ci/mmol, and recalculated specific radioactivity using equation (8) is equal 784.4 cpm/fmol.

Calculation of the concentration. It is possible to accurately calculate the concentration of radionuclides in a stock solution rather than trust the dilutions. Calculations can be performed (Eq.9), if the number of counts per minute in a small volume of solution is measured. C is cpm counted, V is volume of the solution in ml, and Y is the specific activity of the radionuclides in cpm/fmol in this equation [9]:

$$Concentration = \frac{C \text{ cpm} / Y \text{ cpm} / \text{fmol}}{V \text{ ml}} \times \frac{0,001 \text{ pmol} / \text{fmol}}{0,001 \text{ liter} / \text{ml}} = \frac{C}{Y} \quad (9)$$

Calculated concentration of the radioisotopes is 6.16 mol/ml.

Comparison of the results of calculations based on experimental measurements of spectrum of ^{99m}Tc and the results obtained by using different computing tools is presented in the Table1 and Fig.8. Results in the Table1 indicate some differences in the calculated values of various parameters. These differences could be influenced through application of different algorithms for the calculation, data (experimental or theoretical) used for the evaluation of the activity of radionuclide, and experimental conditions.

Table 1. Comparison of the results of calculations obtained by using different theoretical and experimental data

	Experimental data		Calculator1		Calculator2		Calculator3	
Efficiency, %	16,10	100 %	16,06	99.75 %	16,05	99.69 %	16,10	100 %
Specific radioactivity, cpm/fmol	781,44	100 %	784,37	100.37 %	783,88	100,31 %	781,44	100 %
Concentration, mol/ml, *10 ⁶	6,16	100 %	6,13	99.51 %	6,14	99.67 %	6,16	100 %

Different efficiencies of the counters introduce differences in all calculations as well.

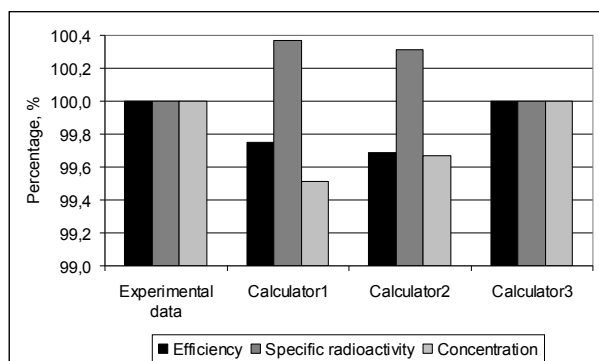


Fig. 8 Diagram of the main parameters of our calculations for the particular radioisotope.

4. Conclusions

1. Calculated efficiency of the gamma spectrometer, and from the experimental data evaluated specific radioactivity and concentration of ^{99m}TcO₄ fit well with the results of calculations when radioactivity Calculator3 was used.

2. The results obtained from the calculations performed by other computing tools (Calculator1 and Calculator2), differ slightly from our results. This difference can be influenced by the efficiency of the counter and has to be assumed, when performing quick radioactivity calculations.

5. References

1. K. Schwochau, Technetium: Chemistry and Radiopharmaceutical Applications, 2000. p. 446
2. Yagi M., Sekine K, Yoshihara. Detection limit of technetium in ⁹⁹Tc(γ,γ') ^{99m}Tc radioactivation analysis in the presence of molybdenum // Journal of Radioanalytical and Nuclear Chemistry (1991) 155 (6) 435.
3. Ilse Zollez, Technetium-99m Pharmaceuticals: Preparation and Quality Control in Nuclear Medicine (2006) p. 345.
4. Digital hand held spectrometer and dose rate meter with nuclide identification IDENTIFINDER. User's manual, Target Systems, 2005.
5. www.martindales.com/CalculatorsD_RAD.htm.
6. F. Russ, F. Knapp, S. Mirzadeh, A. L. Beets. Reactor production and processing of therapeutic radioisotopes for applications in nuclear medicine // Journal of Radioanalytical and Nuclear Chemistry (1996) 205 (1) 93.

7. The Encyclopedia of the Chemical Elements. Applications.
8. $^{99}\text{Mo}/^{99\text{m}}\text{Tc}$ Radionuklidic Generator. Operating Instruction, POLATOM, 2005.
9. Hutton, Brian F., Basic advice for Nuclear Medicine Technologists. Applied radiation and Isotopes (2002) 18, 234.
10. W. Williamson, Radiation safety in Nuclear Medicine, 2003.

LINEAR ACCELERATOR ROOM SHIELDING CALCULATIONS

Eglė Garnytė*, Marius Laurikaitis**

* Kaunas University of Technology, Physics Department, Studentų g. 50, LT-51368 Kaunas, Lithuania;

** Oncological Hospital of Kaunas Medical University Hospital, Volungių g. 16, LT-45434 Kaunas, Lithuania;

Abstract

Algorithm for the calculation of room shielding in the case when the existing Co-60 unit is replaced by a new 15 MV linear accelerator, which full fill all radiation protection requirements is discussed in this paper. It is shown, that there is the necessity for the additional shielding of the primary beam. The maze door has to be heavy shielded due the neutron radiation. Reduction of the the door thickness and weight is possible, if the maze will be reconstructed and prolonged.

Keywords: linear accelerator, radiation, shielding.

1. Introduction

Linear accelerator is a new generation radiotherapy unit that can produce high energies photons and electrons, allows to achieve maximal influence on the tumour and keeps healthy risk organs. The accelerator room must be shielded to reduce radiation dose to the safety limits. Shielding has to secure, that annual radiation dose does not exceed the possible limits. According to the Lithuanian regulations [1], radiotherapy room shielding must be thick enough to reduce annual effective dose from the primary, leakage and scatter radiation to 10 mSv for working staff, and 0.3 mSv for the members of public. The instantaneous dose rate at every place, which can be occupied by person, must not exceed 20 μ Sv/h, .except places which are controlled and radiotherapy rooms,

The linear accelerators, which generate high energy electrons (> 8 MeV) induce the neutron radiation [2]. Neutron production in the radiotherapy accelerators can contribute to the increased doses to patient and to operating personnel from direct neutron exposure and residual radioactivity. A nucleus can absorb energy from a high energy electron or photon and to exceed this minimum energy. Neutrons also can be emitted during the process of photon or electron induced fission. Photo-neutrons are produced mainly from the target, flattener and collimator. The potential sources of neutron contamination are materials on which the electron beam is incident (walls of the wave guide in the linear accelerators or patients). The potential sources of residual radioactivity are any places where neutrons are produced or absorbed.

The aim of this work is to find out the algorithm for the calculation of the room shielding adopting the Co-60 unit room to the new 15 MV linear accelerator. All radiation protection requirements has to be full filled.

2. The calculation model

For estimation of shielding elements we need estimate equipment workload per week, weekly expected dose limits for controlled and uncontrolled areas, use factors, occupancy factors, distances from target to measurement points and etc.

The workload W is stated in terms of the weekly dose at 1 m from the source [Gy/week]. The workload for conventional radiotherapy is determined by [3]:

$$W = \frac{\text{patients}}{\text{hour}} \cdot \frac{\text{hours}}{\text{day}} \cdot \frac{\text{days}}{\text{week}} \cdot \frac{\text{Gy}}{\text{patient}} \quad (1)$$

The value of 50 Gy/week must be added to workload for including daily warm-ups, quality control procedure, calibrations, etc.

The use factor U refers to the fraction of time over the course of a year that the primary barrier is pointing at a particular barrier. The fractional values of $\frac{1}{4}$ for walls, ceilings and floor are recommended to use [3].

The occupancy factor T for a shielding barrier is the time spent by maximal exposed person in the area beyond that barrier. The factor for non-controlled areas depends on the situation [3]. Full occupancy – for offices, laboratories, living quarters, occupied space in nearby building, etc. Quarter occupancy – for corridors, rest rooms, unattended parking lots, etc. One-sixteenth occupancy – for waiting rooms, toilets, outside areas used only for pedestrians and vehicular traffic. For controlled areas, the occupancy is recommended to be one.

Shielding calculations are based on calculation of shielding design goal per week P [Sv/week] [3]:

$$P = B \cdot H_o, \quad (2)$$

where B – barrier transmission factor, H_o – unattenuated dose equivalent at the location to be protected [Sv/week].

Barrier transmission factor is the ratio of the detector response at a location behind a shield on which radiation is incident to the detector response at the same location without the presence of the shield. The barrier transmission factor B is calculated by:

$$B = \frac{P}{H_o}. \quad (3)$$

It is necessary to determine barrier thickness x that is needed to achieve B . The barrier transmission factor B is a function of tenth value layer (TVL) number n that are needed to satisfy the shielding design goal:

$$B = 10^{-n}, \quad (4)$$

or

$$n = \log_{10} \left(\frac{1}{B} \right). \quad (5)$$

Often first barrier TVL_1 is not equal to the next barrier TVL_e ($TVL_1 \neq TVL_e$), so the barrier thickness x is determined as:

$$x = TVL_1 + (n - 1) \cdot TVL_e. \quad (6)$$

Two types of barriers have to be considered (Fig. 1):

- a) primary barrier – the primary radiations is directly incident on this;
- b) secondary barrier – secondary radiations, leakage and scatter impinge on this type.

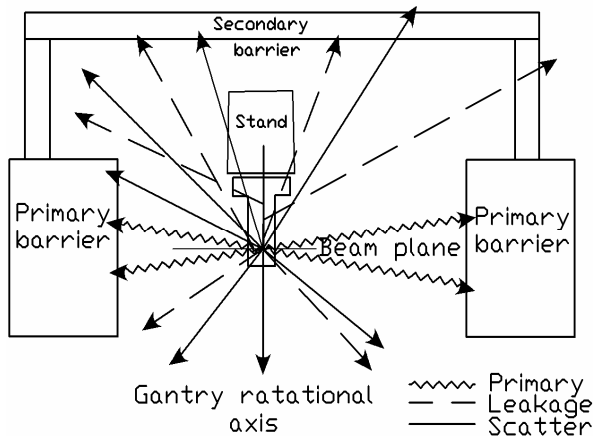


Fig. 1. Two types of barriers in the linear accelerator room.

2.1. Primary barriers calculation

Primary radiation is a radiation used to treat the patient. The maximum field size of $40 \times 40 \text{ cm}^2$ is always assumed for shielding purposes. The required barrier transmission factor B_{pri} for primary radiation is given by [3]:

$$B_{pri} = \frac{P d_{pri}^2}{WUT}, \quad (7)$$

where P – the weekly shielding design dose limit [Sv/week]; d_{pri} – the distance from the target to the point of measurement [m].

The width w [m] of the primary barrier is calculated using maximum diagonal field size at the barrier and adding 30 cm distance on each side of barrier:

$$w = 0.4\sqrt{2}d_{pri} + 0.6. \quad (8)$$

2.2. Secondary barrier calculation

2.2.1. Scatter radiation

Scatter radiation is a radiation generated by the two principal sources – the patient and the primary beam (attenuated by the patient) striking a primary barrier. The required barrier transmission factor B_{sca} for scattered radiation is given by [3]:

$$B_{sca} = \frac{P}{aWT} d_{sec}^2 d_{sca}^2 \frac{400}{F}, \quad (9)$$

where a – is the scatter fraction of particular angle and incoming beam energy; d_{sec} – the distance from the scatterer to the point measurement [m]; d_{sca} – the distance from the target to the scatterer (isocenter distance) [m]; F – the area of the beam in the plane of the scatterer [cm^2].

2.2.2. Leakage radiation

Leakage radiation refers to the X-rays generated in the head of the accelerator during the interactions of the primary electrons and the target, flattening filter, collimator jaws and other surrounding. The required barrier transmission factor B_{leak} for leakage radiation is given by [3]:

$$B_{leak} = \frac{1000 \cdot P d_{leak}^2}{WT}, \quad (10)$$

where d_{leak} – the distance from the target to the point of measurement [m]; the factor 1000 means the leakage radiation at 1 m not exceed 0,1 % of the primary beam at isocenter.

Leakage and scattered radiation are considered for the secondary radiation. If the required thicknesses for scattered and leakage radiation are within 1 HVL, an additional HVL is added.

2.2.3. Neutrons

The neutrons fluence Φ can be calculated for a room of a given size using a method given by McCall [2]:

$$\Phi = \frac{Q}{2\pi} \left(\frac{c}{2R^2} + \frac{5.4c}{S} + \frac{1.26}{S} \right), \quad (11)$$

where Q – the number of fast neutrons; c – a constant for a given accelerator (0.85 – for an all tungsten shielded machine; 1.0 – for an all lead shielded machine); R – the distance between the source and the detector [m]; S – the inside surface area of the room [m²]; 2π – factor for the scattered and thermal neutrons. The average energy can be derived from this fluence and the neutron dose can be calculated from fluence to dose conversion factors given graphically.

2.2.4. Maze doors

When calculating the radiation incident on the door at the end of the maze, several sources of secondary radiation have to be taken into account. These include leakage from the accelerator head, scattered radiation from the patient and scattered radiation from the primary beam hitting the primary barrier, and leakage from the accelerator head penetrating the inner maze wall.

Leakage from the accelerator head H_l is scattered by the wall maze towards the maze door. The equation from this process is given by [4]:

$$H_l = \frac{L_0 D_0 \alpha_0 A_M}{(d_{n1} d_{n2})^2}, \quad (12)$$

where L_0 – the leakage factor, taken at 1 m from target; D_0 – the dose at isocenter [Gy]; α_0 – the reflection coefficient for the leakage from back wall in the direction of the maze; A_M – the area of the back wall seen by the maze [m²]; d_{n1} – the distance from the target to the maze [m]; d_{n2} – the length along the maze [m].

The dose of primary radiation scattered from the primary barrier H_w towards the maze and in turn down the maze is small, but not negligible. The description of this process is given by [4]:

$$H_w = \frac{D_0 \alpha_1 A_1 \alpha_2 A_M}{(d_{s1} d_{s2} d_{s3})^2}, \quad (13)$$

where α_1 – the reflection coefficient of the primary radiation scattered from the primary barrier; α_2 – the reflection coefficient of the secondary radiation scattered at the maze wall; A_1 – the area of the primary barrier struck by the primary beam [m²]; d_{s1} – the distance from target to the primary barrier [m]; d_{s2} – the distance between the centre of the primary barrier and the maze wall [m]; d_{s3} – the distance along the maze [m].

The primary radiation scattered by the patient is H_p . It is directed towards the direction of the maze, where it is scattered by the back wall down the maze. The equation for this process is given by [4]:

$$H_p = \frac{a D_0 (F/400) \alpha_3 A_M}{(d_{p1} d_{p2} d_{p3})^2}, \quad (14)$$

where α_3 – the reflection coefficient for scattered x-rays from the back wall; d_{p1} – the distance from the target to the scatterer [m]; d_{p2} – the distance from the scatterer to the point measurement [m]; d_{p3} – the length along the maze [m].

The leakage radiation from the head of the machine H_{dl} is reduced by inverse square to the maze door and attenuated by the thickness of the maze wall. The equation for this process is given by [4]:

$$H_{dl} = \frac{L_0 D_0 10^{-(x/TVL)}}{(d_n)^2}, \quad (15)$$

where x – the thickness of maze wall; TVL – the tenth value layer of the maze wall; d_{n1} – the distance from the target to maze door.

The total dose at the door is given by the sum of four contributions [4]:

$$H_t = H_w + H_l + H_{dl} + H_p. \quad (16)$$

Neutrons produced in the head of the linear accelerator are first moderated by the X-ray shielding. Neutrons are further moderated by scattering off the concrete walls of the therapy room. Kersey's formula provides method for determining the neutron fluence at the end of a maze. It is based on a two step process which consists of determination of the fluence at the entrance to the maze and the attenuation of the neutrons down the maze. Thus, the equation is expressed as [5]:

$$H_N = H_0 \frac{S_0}{S} \frac{1}{d_{N1}^2 10^{-d_{N2}/5}}, \quad (17)$$

where H_N – the neutron dose equivalent at maze door; H_0 – the neutron dose equivalent at 1 m from the target; d_{N1} – the distance between the target and entrance to the maze; d_{N2} – the length of the maze; S_0/S – the ratio of the inner to outer maze areas.

For the determining of the production of gamma rays during neutron capture in a maze, calculation of the neutron fluence at the entrance maze is needed (Eq.11). Having the value of the neutron fluence, production of gamma rays by neutron capture is determined using the following equation [6]:

$$D = K\Phi_{total} 10^{-d/TVD^2}, \quad (18)$$

where K – constant ($6.9 \cdot 10^{-12} \text{ cm}^2 \text{ Gy}$); Φ_{total} – total neutron fluence at the end of the maze; d – the length of the maze; TVD^2 – the tenth value distance for γ rays along the maze (5.4 m).

3. Results and discussion

Before the reconstruction of the Co-60 unit bunker to the room for the 15 MV linear accelerator, the calculations were performed to ensure, whether the shielding is sufficient. It was considered that the workload of the operating accelerator will be about 850 Gy/week (2 Gy/patient 80 patients/day; 5 days/week). The other parameters, which were used for the room calculation are shown in Table 1. The room plan, and the shielding elements are shown in Figure 2.

Table 1. The parameters for room calculation

Location	Type	Zone	P, mSv/week	U	T	x, cm
A, A1	Unctrl.	Waiting corridor	0.006	0.25	0.25	140
B	Unctrl.	Room	0.006	-	0.50	110
C, C1	Unctrl.	Grassland	0.006	0.25	0.06	140
D	Ctrl.		0.192	-	1.00	150
E, E1	Unctrl.	Roof	0.006	0.25	0.06	140

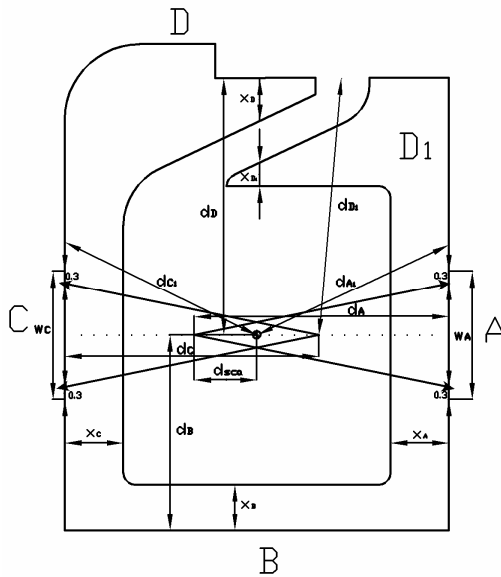


Fig. 2. The room plan and the shielding elements. The distances for primary, scattered and leakage radiation are shown in the picture.

Firstly the primary shielding calculations were performed (Table 2). It was found, that the shielding of all walls, where primary beam is directed is not sufficient. There was a need to add 65-90 cm of concrete. In this case the width of the primary barrier was 377 cm.

Table 2. Thickness required for primary barrier

Location	Type	P, mSv/week	U	T	d _{pri} , m	B _{pri}	n	x _{pri} , cm
A	Unctrl.	0.006	0.25	0.25	5.6	$3.41 \cdot 10^{-6}$	5.47	230.4
C	Unctrl.	0.006	0.25	0.06	5.6	$1.42 \cdot 10^{-5}$	4.85	204.6
E	Unctrl.	0.006	0.25	0.06	4.5	$3.41 \cdot 10^{-6}$	5.04	212.5

Next step was to determine the thickness of the secondary barrier. The required thickness was calculated separately for the scattered (Table 3) and leakage (Table 4) radiation. Total secondary barrier thickness was estimated using TVL rule (Table 5). It was found, that there was a need to add 20 cm of concrete more to the wall B, because the treatment room is located behind this wall and it needs more protection. Other walls satisfy all shielding requirements.

Table 3. Thickness required for scattered radiation

Location (θ)	Type	P, mSv/week	T	d _{sec} , m	$\alpha(\theta)$	B _{sca}	n	x _{sca} , cm
A1 (30°)	Unctrl.	0.006	0.25	5.2	$2.77 \cdot 10^{-3}$	$2.65 \cdot 10^{-4}$	3.58	134.8
B (90°)	Unctrl.	0.006	1.00	4.9	$2.61 \cdot 10^{-4}$	$1.25 \cdot 10^{-3}$	2.90	109.5
C1 (30°)	Unctrl.	0.006	0.06	5.2	$2.77 \cdot 10^{-3}$	$1.10 \cdot 10^{-3}$	2.96	111.5
D (90°)	Ctrl.	0.192	1.00	6.5	$2.61 \cdot 10^{-4}$	$3.66 \cdot 10^{-2}$	1.44	54.1
E1 (90°)	Unctrl.	0.006	0.06	4.2	$2.77 \cdot 10^{-3}$	$7.20 \cdot 10^{-4}$	3.14	118.5

Table 4. Thickness required for leakage radiation

Location	Type	P, mSv/week	T	D _{leak} , m	B _{leak}	n	x _{leak} , cm
A1	Unctrl.	0.006	0.25	5.2	$7.34 \cdot 10^{-4}$	3.13	108.2
B	Unctrl.	0.006	1.00	4.9	$3.26 \cdot 10^{-4}$	3.49	120.2
C1	Unctrl.	0.006	0.06	5.2	$3.06 \cdot 10^{-3}$	2.51	87.3
D	Ctrl.	0.192	1.00	6.5	$9.56 \cdot 10^{-3}$	2.02	70.6
E1	Unctrl.	0.006	0.06	4.2	$2.00 \cdot 10^{-3}$	2.70	93.6

Table 5. Thickness required for secondary barrier

Location	x _{sca} , cm	x _{leak} , cm	x _{sec} , cm	x _{sec} (θ) = $\cos(\theta) \cdot x_{sec}$, cm
A1	134.8	108.2	145.0	125.6
B	109.5	120.2	130.3	130.3
C1	111.5	87.3	121.6	105.3
D	54.1	70.6	80.7	80.7
E1	118.5	93.6	128.6	111.4

The last part of calculation was performed with a purpose to determine the dose equivalent at the door. The distances needed for the calculation of the dose at the maze door are indicated in Fig.3. The results of calculation are shown in Table 6.

Table 6. Dose equivalent at the door

Location	Type	P, mSv/week	H _l	H _w	H _p	H _{dl}	H _t	H _N
Door	Ctrl.	0.192	0.022	0.121	0.039	0.001	0.183	0.638

The dose equivalent H_T from photon radiation is under the limit, but the dose from neutron radiation H_N is 3.3 times higher than the dose limits. Due to this reason, there is a need to use heavy shielded doors for reduction of the dose equivalent. Another possible option to reduce the neutron dose is to rebuild the maze in the room, making it longer.

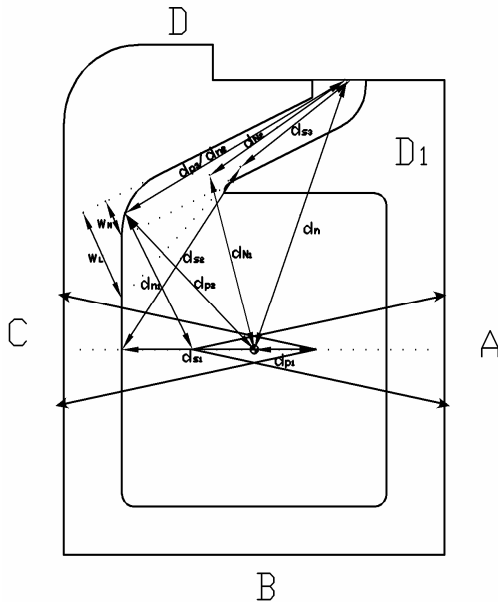


Fig. 3. The distances required for the maze doors calculation.

4. Conclusions

There is a need to rebuild the Co-60 room before the installation of the new linear accelerator. It is necessary to shield primary beam increasing the thickness of the wall C. The maze doors must be heavy shielded due neutron radiation. Possible solution for the reduction of the door thickness and weight is a prolonged construction of the existing maze.

5. References

1. Lithuanian Hygiene Standard HN 95:2005 "Radiation protection and quality control in radiotherapy".
2. NCRP report No. 79. Neutron contamination from medical electron accelerators. Bethesda, MD: NCRP, 1984.
3. NCRP report No. 49. Structural shielding design and evaluation for medical use of x-rays and gamma rays of energies up to 10 MV. Bethesda, MD: NCRP, 1976.
4. McGinley P.H. Shielding techniques for radiation oncology facilities. Second edition, Madison, WI: Medical Physics Publishing, 2002.
5. Kersey R.W. Estimation of neutron and gamma radiation doses in the entrance mazes of SL75-20 linear accelerator treatment rooms. Medicamundi 24, 1979. p. 150-155.
6. McGinley P.H., Miner M.S., Mitchum M.L. A method for calculating the dose due to capture gamma rays in accelerator mazes. Physics in medicine and biology 40, 1995. p. 1467-1473.

AUTHOR INDEX

- Adlienė D. 41,69,74
Adlys G. A. 41,64
Adlys G.G. 64
Andersson I. 45
Andrijaitienė V. 74
Bäck S. Å. J. 24,41
Bagdonas S. 10
Båth M. 45
Bernhardsson Ch. 60
Burneikis A.
Christiansson M. 60
Churbakova E. 55
Cibulskaitė I. 69
Dekhtyar Yu. 28,48
Eglite M. 55
Gabrusheva N. 55
Garnytė E. 83
Gražalienė G. 10, 19
Gricienė B. 69
Grube M. 50
Golikov S. 60
Griškevičius R. 39
Gudaitis R. 35
Gustavsson H. 24
Hemdal B. 45
Jesko T. 60
Karabanovas V.
Kärner T. 55
Karlsson A. 24
Katashev A. 48
Kulvietis V. 19
Kurjane N. 55
Lapienis J. 19
Laurikaitienė J. 41,69,78
Laurikaitis M. 41,69,83
Månsson S. 24
Mattsson S. 5,41,45,60
Miller A. 28, 39
Mironova-Ulmane N. 50,55
Nordström F.24,41
Pavlenko A. 55
Piekstina D. 55
Plaude S. 28
Plukys M. 10
Polakovs M. 50,55
Popov S. 28,39,48
Raila.S. 41
Räaf Ch. 60
Reinholds E. 50
Ruschin M. 45
Rotomskis R. 10,15,19
Rožanova N. 48
Simutytė I. 39
Skripkaitė E. 78
Stenström K. 5
Svahn T 45
Šiupšinskas L. 35
Šniurevičiūtė M. 69
Tamošiūnas M. 10
Tamulevičius S. 35
Timberg P. 45
Tingberg A. 45
Thornberg Ch. 60
Vainoras A. 35
Urbonienė A. 69
Valančiūnaitė J.
Venius J. 15
Vespenderytė L. 74
Wittgren L. 24
Zakarevičius E. 19
Zakrevskaja T. 41
Zikas M. 74
Zvagule T. 55
Zvonova I. 60
Žiliukas J

Information for Authors

Only original works, nowhere else published before, dealing with the conference topics and prepared in compliance with the enclosed requirements will be accepted for the conference.

The paper must be written in English. The written material of the article should be prepared on a paper of A4 size using Microsoft Word for Windows text editor. The length of the paper must be of 4 or 6 pages.

The paper must be written in two columns in **Times New Roman fonts, single spacing and with no indentations**.

Margins on the first page are as follows: left, right and bottom margins – 2 cm, top margin – 6 cm wide. All **margins on the second and subsequent pages** are 2 cm wide.

On the first page title of paper ought to be placed at the distance of 6 cm from the top edge of the page. The title should be written in bold capital letters using Times New Roman 13-point font, single spacing and centered in the whole width of the page. Below the title there should be 2 empty, 10-point lines left.

In lines that follow in order the names of the authors and institutions are written (surname in capitals) using 10-point font with single spacing. Next, there are again 3 empty lines of a 10-point height.

Below, the actual text of the paper begins. The text is written in two columns with the space of 1 cm between them, using Times New Roman 10-point font, single spacing. The text should begin with an abstract (the word 'Abstract' written in 10-point bold italics) of a scope of not more than 10 lines (10-point font also). The abstract section is followed by keywords section written in the same way.

Titles of chapters should be written in 10-point bold type font with single spacing. They should be numbered by successive Arabic figures and centered in lines. **Titles of subsections** are to be written in 10-point bold type font with single-spacing as well, but they should be aligned with the left edge of the column. All titles are to be separated from the text by 1 (10-point) empty line above, and 1 (6-point) empty line below the title.

Contents of chapters and subsections must be aligned with both edges of each column without any additional spacing between lines.

Drawings, diagrams and photographs are to be considered as the same and referred to using abbreviations, for instance 'Fig.' and marked as Fig. along with the successive number. The drawings may be prepared by using of any technique (as black lines on a white background) and photographs must be black-and-white only. Captions of figures are to be written in 9-point font, single spacing. The font size on the figures should ensure them a good legibility. The space between figure and its caption should have the size of 6-point font. Above each figure and below its caption should be 1 empty line spacing (10-point).

Tables ought to be numbered by Arabic figures and referred to by the word, for instance: Table 1. The headings informing about the contents of tables should begin with the word 'Table' followed by the successive number and ought to be written in 9-point font and shifted towards the left margin. The heading should be separated from the table by 1, 6-point empty line.

Figures and tables should be not more than 8 cm wide and ought to be centered in column. In particular cases it is allowed to insert figures or tables that require the full width of page (maximum 17 cm). In such cases they should be centered on the full width of page together with captions or headings.

Mathematical equations ought to be centrally arranged in lines and numbered by successive Arabic figures using parentheses aligned with the right-side edge of the column. Symbols and variables in equations as well as in the text should be written in italics, while vectors and matrices in ordinary bold type. Equations ought to be separated from the text by 1 empty line (10-point).

After the actual text, the article should contain **references and sources** from which the information has been taken. The references must be numbered successively by Arabic figures and referred to in the text by these numbers in square brackets, for instance: [2]. Each successive reference should be written with single spacing and an incision of 0.5 cm in every successive line.

The enclosed **example of paper** provides the general arrangement and the main requirements for preparing the manuscript.

TITLE OF PAPER WRITTEN IN BOLD CAPITAL LETTERS USING 13-POINT FONT, WITH SINGLE SPACING AND CENTERED

2 empty lines using 10-point font with single spacing

First name and SURNAME*, First name and SURNAME**, First name and SURNAME***
 *Institution of the Author; **Institution of the Author; ***Institution of the Author

2 empty lines using 10-point font with single spacing

Abstract

The text should begin with an abstract of a scope of not more than 10 lines (10-point font). The word ‘Abstract’ written in 10-point bold italics.

1 empty line using 10-point font with single spacing

Keywords: This section is written in the same way as the abstract section above.

1. Introduction

The scope of the paper must not exceed 6 pages of A4 size and should have an even number of them. The paper should be created in MS Word for Windows (doc) formats.

1 empty line using 10-point font with single spacing

2. Page arrangement

Margins on the first page are as follows: left, right and bottom – 2 cm, top margin – 6 cm wide. All margins on the second and subsequent pages are 2 cm wide. The text of the paper is written in two columns with a space of 1 cm between them. An empty place should be leaved at the top of the first page.

1 empty line using 10-point font with single spacing

3. Illustrations, tables and equations

3.1. Tables

Tables ought to be numbered by Arabic figures and referred to in the text by the word, for instance: Table 1.

1 empty line using 10-point font with single spacing

Table 1. Recommended font types for tables

Font type	Example
Times New Roman	9-point / 10-point
Arial	8-point / 9-point

1 empty line using 10-point font with single spacing

3.2. Mathematical equations

Mathematical equations ought to be centrally arranged in lines and numbered by successive Arabic figures using parentheses aligned with the right-side edge of the column.

1 empty line using 10-point font with single spacing

$$u(t) = U_m \sin(\omega t + \varphi) \quad (1)$$

1 empty line using 10-point font with single spacing

3.3. Drawings, diagrams and photographs

Drawings, diagrams and photographs are considered as the same and referred to in the text using abbreviations, for example: Fig. 1.

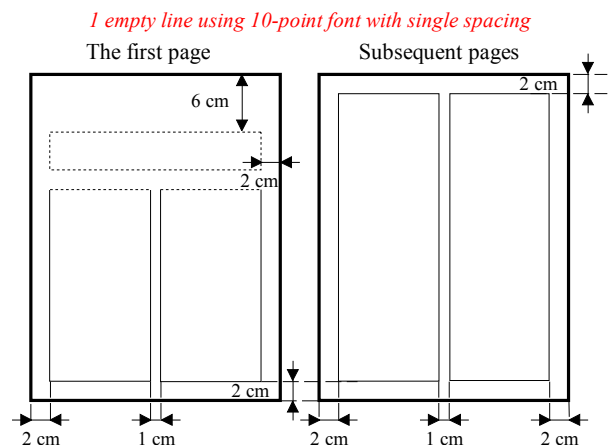


Fig. 1. Arrangement of printing area on an A-4 size page for the first and subsequent pages of manuscript

1 empty line using 10-point font with single spacing

4. Conclusions

The instruction for the preparation of final paper manuscripts for the international conference provides the essential arrangement and technical requirements for papers.

1 empty line using 10-point font with single spacing

References

1. Burinskiene V., Laurikaitis M. and Adliene D.. Entrance Surface Dose Measurements with Thermoluminescence Dosimeters and Transmission Ionization Chamber. Proceedings of the 4th

International Conference “Medical Physics in the Baltic States”, Kaunas, 2006. p. 85-87.

2. Cember H. Introduction to Health Physics. Third edition, McGraw-Hill, 1996. 393 p.